CFD study of thick flatback airfoils using OpenFOAM

Master Thesis

$$(EIv'')''=q-\rho A\ddot{v}$$

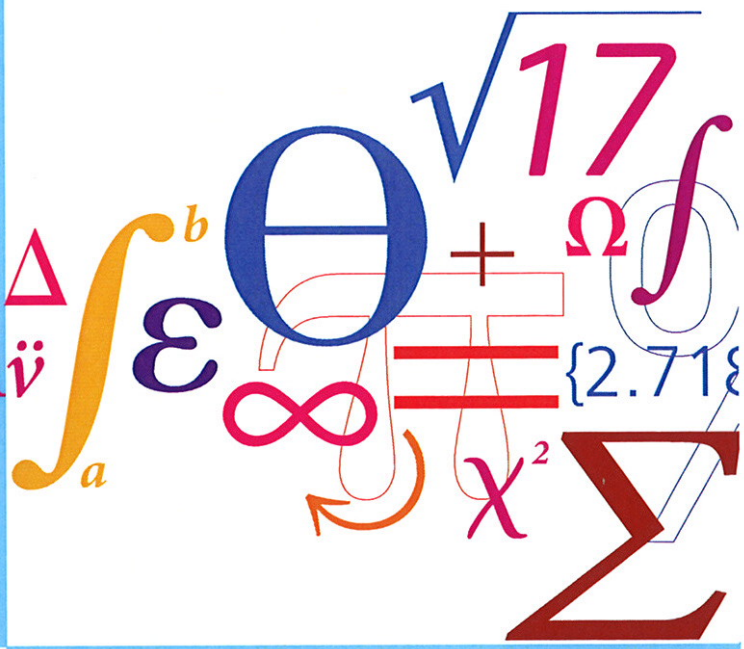

José María Milián Sanz
MEK-FM-EP-2011-03
July 2011

DTU Mechanical Engineering
Department of Mechanical Engineering

Contents

Contents i

List of Figures iii

List of Tables ix

Abstract xi

Preface xiii

1 Thesis introduction 1

2 Theory 3
2.1 The Navier-Stokes Equations . . . 3
2.2 Reynolds number . . . 5
2.3 Reynolds Averaged Navier-Stokes equation, RANS . . . 5
2.4 Turbulence modelling . . . 6
2.5 Transition prediction model . . . 8
2.6 Near wall treatment . . . 11
2.7 Airfoil parameters . . . 13
2.8 Force Coefficients . . . 14
2.9 Numerical schemes . . . 15
2.10 XFOIL . . . 18
2.11 Creating the flatback airfoils . . . 19

3 Meshing 21

4 NACA0012 - Sensitivity Studies 25
4.1 NACA0012 vs NACA0012 blunt . . . 25
4.2 Comparison of both $k-\omega$ SST and Spalart-Allmaras turbulence models . . . 28
4.3 Introducing the transition prediction model . . . 34
4.4 y^+ dependence study . . . 41
4.5 Domain extent . . . 41

4.6 Cell count dependence study 45
4.7 Numerical schemes dependence 47

5 Thick-blunt airfoils validation 49
5.1 Fully Turbulent vs Free Transition 50
5.2 Comparison of different CFD codes for the airfoil FX-77-W-343 53
5.3 Comparison of different CFD codes for the airfoil FX-77-W-400 58
5.4 Comparison of different CFD codes for the airfoil FX-77-W-500 60
5.5 Comparison of the performance of the airfoils FX-77-W studied 62

6 Thick-flatback airfoils validation 65
6.1 Comparison of different CFD codes for the airfoil FB-3500-0050 66
6.2 Comparison of different CFD codes for the airfoil FB-3500-0875 68
6.3 Comparison of different CFD codes for the airfoil FB-3500-1750 70
6.4 Comparison of the performance of the airfoils FB-3500 studied 72
6.5 Study of the flow around flatback airfoils 81

7 Thick-flatback airfoils study 89
7.1 Flatbacking of the airfoils studied 89
7.2 *NEW* flatback airfoils 92
7.3 *NEWsym* flatback airfoils 94
7.4 *NEWthick* flatback airfoils 97
7.5 NACA8648 flatback airfoils 100

8 Comments to the convergence of the solution 107
8.1 Initialization of the field with *potentialFoam* 107
8.2 Sensitivity Study 109

9 Conclusion 111
9.1 Future work 113
9.2 Future work 114

Bibliography 115

Appendices 118

A Meshing a NACA0012 with a sharp trailing edge 119

B Results computed with ANSYS CFX and Ellipsys for the airfoils FX-77-W 125

C Results computed with ANSYS CFX and Ellipsys for the airfoils FB-3500-XXXX 129

D Comparison of the results obtained with OpenFOAM and ANSYS CFX for the airfoils NEW TE X% 133

E Comparison of the results obtained with OpenFOAM and ANSYS CFX for the airfoils *NEWsym* TE X% 137

F Comparison of the results obtained with OpenFOAM and ANSYS CFX for the airfoils *NEWthick* TE X% 141

G Mesh dependence study for the airfoil FX-77-W-400 145

H Mesh dependence study for the airfoil FB-3500-0875 149

I Example of the *fvSolution* file of OpenFOAM 153

List of Figures

2.1 Notation used to obtain the stress tensor. Obtained from reference [17] 4
2.2 Boundary layer on a flat plate. y scale greatly enlarged. Obtained from reference [22]. 9
2.3 Typical velocity profile of a turbulent boundary layer. Obtained from reference [18] 12
2.4 Possibilities of near wall treatment in CFD. Obtained from reference [21]. 13
2.5 Parameters describing the geometry of an airfoil. 14
2.6 Aerodynamic forces on an airfoil. Obtained from reference [23]. . . 15
2.7 Control volume around a node P. Obtained from [19]. 16
2.8 Gradients at the faces for a linear scheme. Obtained from [19]. . . 17
2.9 Gradients at the faces for a quadratic scheme. Obtained from [19]. 17
2.10 Sketch of the parameters used by the function *TGAP* of XFOIL. Created by Alejandro Gómez. 20

3.1 Zoom of the airfoil FB-3500-0875 meshed using an O-mesh. 21
3.2 Zoom of the airfoil FB-3500-0875 meshed using a C-mesh. Example of a mesh not optimal for flatback airfoils. 22
3.3 Zoom at the trailing edge of the Airfoil FB-3500-0875 meshed using a C-mesh. Example of a mesh not optimal for flatback airfoils. . . 22

4.1 Geometry of the NACA0012 airfoil and the NACA0012 airfoil with the blunt trailing edge. 25

4.2 Aerodynamic coefficient curves for the airfoil NACA0012 original and truncated, for Re=3.000.000. Curves obtained with OpenFOAM. 27
4.3 Lift coefficient curves for the airfoil NACA0012 with the blunt trailing edge using the $k-\omega$ SST turbulence model. Re=3.000.000 28
4.4 Drag coefficient curves for the airfoil NACA0012 with the blunt trailing edge using the $k-\omega$ SST turbulence model. Re=3.000.000. 29
4.5 Residuals during the computation performed for the Spalart-Allmaras turbulence model and an angle of attack of 8 degrees. Simulation run for the airfoil NACA0012 with the blunt trailing edge at Re=3.000.000 using OpenFOAM. 30
4.6 Residuals during the computation performed for the $k-\omega$ SST turbulence model and an angle of attack of 8 degrees. Simulation run for the airfoil NACA0012 with the blunt trailing edge at Re=3.000.000 using OpenFOAM. 31
4.7 Force coefficients history for the Spalart-Allmaras turbulence model and an angle of attack of 8 degrees. Simulation run for the airfoil NACA0012 with the blunt trailing edge at Re=3.000.000. . 31
4.8 Force coefficients history for the $k-\omega$ SST turbulence model and an angle of attack of 8 degrees. Simulation run for the airfoil NACA0012 with the blunt trailing edge at Re=3.000.000. 32
4.9 Aerodynamic coefficient curves for the computations using both turbulence models using OpenFOAM. NACA0012 with blunt trailing edge at Re=3.000.000. 33
4.10 Aerodynamic coefficient curves for the computations with OpenFOAM with and without transition model for the boundary layer. NACA0012 at Re=3.000.000. 35
4.11 Curves of the pressure coefficient Cp for the NACA0012 at an angle of attack of 10 degrees and Re=3.000.000. Experimental data taken from [12]. 36
4.12 Friction coefficient curves for the airfoil NACA0012 at an angle of attack of 10 degrees and Re=3.000.000. 37
4.13 C_f curves at both pressure and suction side for the different cases specified for a NACA0012 at an angle of attack of 2 degrees at Re=3.000.000. 38
4.14 C_p curves for the different cases specified for a NACA0012 at an angle of attack of 2 degrees at Re=3.000.000. 39
4.15 Position predicted for the transition point on the airfoil NACA0012 at Re=3.000.000. 40
4.16 y^+ sensitivity study on the NACA0012 airfoil with the trailing edge blunt at Re=3.000.000. 42
4.17 Topology view of the meshes done in order to do the domain extent sensitivity study. 43
4.18 Sensitivity study of the domain extent. Simulations for the airfoil NACA0012 with the blunt trailing edge at Re=3.000.000. 44

4.19 Mesh dependence study for the NACA0012 with the blunt trailing edge for an angle of attack of 2 degrees at Re=3.000.000. 45
4.20 Mesh dependence study for the NACA0012 with the blunt trailing edge for an angle of attack of 8 degrees at Re=3.000.000. 46
4.21 Mesh dependence study for the NACA0012 with the blunt trailing edge for an angle of attack of 14 degrees at Re=3.000.000. 46
4.22 Aerodynamic coefficients obtained for different differencing schemes in the convective terms of the RANS equation. Tested at the airfoil NACA0012 with the blunt trailing edge at Re=3.000.000. 48

5.1 Comparison of the geometry of the airfoil FX-77-W studied. 50
5.2 Aerodynamic coefficients for the airfoil FX-77-W-343 with and without transition model applied at Re=3.000.000. 51
5.3 Aerodynamic coefficients for the airfoil FX-77-W-343 with and without transition model applied at Re=3.000.000. Results obtained with ANSYS CFX 52
5.4 Aerodynamic coefficients for the airfoil FX-77-W-343 at Re=3.000.000. 54
5.5 Contour plot of the velocity field for the airfoil FX-77-W-343 at Re=3.000.000 and an angle of attack of 14 degrees. 55
5.6 Numerical schemes dependence study for the airfoil FX-77-W-343 at the stall region at Re=3.000.000. 57
5.7 Aerodynamic coefficients for the airfoil FX-77-W-400 at Re=4.000.000. 59
5.8 Aerodynamic coefficients for the airfoil FX-77-W-500 at the Reynolds number specified. 61
5.9 Comparison of the results for the lift coefficient of the airfoils FX-77-W at the different Reynolds number specified. OpenFOAM=solid line. Experiments=broken line. 63
5.10 Comparison of the results for the drag coefficient of the airfoils FX-77-W at the different Reynolds number specified. OpenFOAM=solid line. Experiments=broken line. 63

6.1 Comparison of the geometry of the airfoil flatback FB-3500-XXXX studied. 66
6.2 Aerodynamic coefficients for the airfoil FB-3500-0050 at Re=666.000. 67
6.3 Aerodynamic coefficients for the airfoil FB-3500-0875 at Re=666.000. 69
6.4 Aerodynamic coefficients for the airfoil FB-3500-1750 at Re=666.000. 71
6.5 Comparison of the the lift coefficient for the airfoils FB-3500 at Re=666.000. OpenFOAM = solid line, Experiments = broken line. 73
6.6 Comparison of the drag coefficient for the airfoils FB-3500 at Re=666.000. OpenFOAM = solid line, Experiments = broken line. 73
6.7 Comparison of the lift to drag ratio of the airfoils FB-3500 at Re=666.000. OpenFOAM = solid line, Experiments = broken line. 74
6.8 Streamlines for the airfoil FB-3500-0050 at an angle of attack of 14 degrees at Re=666.000. 74

6.9 Streamlines for the airfoil FB-3500-0875 at an angle of attack of 14 degrees at Re=666.000. 75
6.10 Streamlines for the airfoil FB-3500-1750 at an angle of attack of 14 degrees at Re=666.000. 76
6.11 Cp curves for the airfoils FB-3500 simulated with OpenFOAM for an angle of attack of 14 degrees at Re=666.000. 76
6.12 Friction coefficient curves for the airfoils FB-3500 simulated with OpenFOAM for an angle of attack of 14 degrees at Re=666.000. . 77
6.13 Turbulent kinetic energy field for the airfoil FB-3500-0050 at an angle of attack of 14 degrees at Re=666.000. 78
6.14 Turbulent kinetic energy field for the airfoil FB-3500-1750 at an angle of attack of 14 degrees at Re=666.000 78
6.15 Comparison of the location of the transition point for the different airfoils specified at Re=666.000. 80
6.16 Comparison of the magnitude of the velocity at the wake of the airfoil FB-3500-1750 at a distance x from the trailing edge. Re=666.000 and angle of attack 14 degrees. 81
6.17 Vector field of the velocity at the wake of airfoil FB-3500-1750 at Re=666.000 and an angle of attack of 14 degrees. 82
6.18 Comparison of the geometry of the airfoil FB-3500-1750 and the airfoils generated adding chord downstream in the dead water region. 82
6.19 Vector field of the velocity at the wake of airfoil FB-3500-1750 at Re=666.000 and an angle of attack of 14 degrees. 83
6.20 Comparison of the geometry of the airfoil FB-3500-1750 and the airfoils generated adding chord downstream in the dead water region. 84
6.21 Velocity field and streamlines for the airfoil FB-3500-1750 with an addition of 20 % of the chord length into the dead water region shown in figure 6.10. Re=666.000 and angle of attack of 14 degrees. 84
6.22 Velocity field and streamlines for the airfoil FB-3500-1750 with an addition of 35 % of the chord length into the dead water region shown in figure 6.10. Re=666.000 and angle of attack of 14 degrees. 85
6.23 Turbulent kinetic energy field for the airfoil FB-3500-1750 with an addition of 20 % of the chord length into the dead water region shown in figure 6.10. Re=666.000 and angle of attack of 14 degrees. 86
6.24 Turbulent kinetic energy field for the airfoil FB-3500-1750 with an addition of 35 % of the chord length into the dead water region shown in figure6.10. Re=666.000 and angle of attack of 14 degrees. 87

7.1 Different openings done by Risø DTU at the airfoil DU-97-W-300 (shown in red color). Figures obtained from [27]. 90
7.2 Results for the different flatback airfoils created by Risø DTU, shown in figures 7.1. Figures obtained from [27]. 91
7.3 Lift coefficient normalized for the airfoil *NEW* at Re=4.000.000. . 92
7.4 Drag coefficient normalized for the airfoil *NEW* at Re=4.000.000. . 93

7.5 Lift-to-drag ratio normalized for the airfoil *NEW* at Re=4.000.000. 93
7.6 Lift coefficient normalized for the airfoil *NEWsym* at Re=4.000.000. 95
7.7 Drag coefficient normalized for the airfoil *NEWsym* at Re=4.000.000. 95
7.8 Lift-to-drag ratio normalized for the airfoil *NEWsym* at Re=4.000.000. 96
7.9 Lift coefficient normalized for the airfoil *NEWthick* at Re=4.000.000. 98
7.10 Drag coefficient normalized for the airfoil *NEWthick* at Re=4.000.000. 98
7.11 Lift-to-drag ratio normalized for the airfoil *NEWthick* at Re=4.000.000. 99
7.12 Comparison of the geometry of the flatback airfoils NACA8648. . . 100
7.13 Lift coefficient normalized for the airfoil NACA8648 at Re=4.000.000.101
7.14 Drag coefficient normalized for the airfoil NACA8648 at Re=4.000.000.102
7.15 Lift-to-drag ratio normalized for the airfoil NACA8648 at Re=4.000.000.102
7.16 Location of the transition point for laminar to turbulent boundary layer at the airfoil NACA8648 at Re=4.000.000. 103
7.17 Pressure coefficient at the airfoil NACA8648 at Re=4.000.000 and an angle of attack of 10 degrees. 104
7.18 Friction coefficient at the airfoil NACA8648 at Re=4.000.000 and an angle of attack of 10 degrees. 105

8.1 Solution for the flow around a flat plate at time step 15, field initialized with *potentialFoam*. 108
8.2 Solution for the flow around a flat plate at time step 15, field not initialized with *potentialFoam*. 108

A.1 Different C-meshes tried for the airfoil NACA0012. 120
A.2 Lift coefficient curves for the airfoil NACA0012 at Re=3.000.000 with different distribution of cells, cases from table A.1. Curves obtained with ANSYS CFX. 122
A.3 Drag coefficient curves for the airfoil NACA0012 at Re=3.000.000 with different distribution of cells, cases from table A.1. Curves obtained with ANSYS CFX. 122
A.4 Lift coefficient curves for the airfoil NACA0012 at Re=3.000.000 for the mesh from figure A.1d, case 5 from table A.1. 123
A.5 Drag coefficient curves for the airfoil NACA0012 at Re=3.000.000 for the mesh from figure A.1d, case 5 from table A.1. 123

B.1 Comparison of the results obtained with ANSYS CFX and Ellipsys of the lift coefficient for the airfoils FX-77-W at the different Reynolds number specified. 126
B.2 Comparison of the results obtained with ANSYS CFX and Ellipsys for the drag coefficient of the airfoils FX-77-W at the different Reynolds number specified. 126
B.3 Comparison of the results obtained with ANSYS CFX and Ellipsys for the lift-to-drag ratio of the airfoils FX-77-W at the different Reynolds number specified. 127

C.1 Comparison of the the lift coefficient for the airfoils FB-3500 at Re=666.000. ANSYS CFX = solid line, Ellipsys = broken line. . . 130

C.2 Comparison of the drag coefficient for the airfoils FB-3500 at Re=666.000. ANSYS CFX = solid line, Ellipsys = broken line. 130

C.3 Comparison of the lift to drag ratio of the airfoils FB-3500 at Re=666.000. ANSYS CFX = solid line, Ellipsys = broken line. . . 131

D.1 Lift coefficient normalized for the airfoil *NEW* at Re=4.000.000. OpenFOAM=solid line, ANSYS CFX=broken line. 134

D.2 Drag coefficient normalized for the airfoil *NEW* at Re=4.000.000. OpenFOAM=solid line, ANSYS CFX=broken line. 134

D.3 Lift-to-drag ratio normalized for the airfoil *NEW* at Re=4.000.000. OpenFOAM=solid line, ANSYS CFX=broken line. 135

E.1 Lift coefficient normalized for the airfoil *NEWsym* at Re=4.000.000. OpenFOAM=solid line, ANSYS CFX=broken line. 138

E.2 Drag coefficient normalized for the airfoil *NEWsym* at Re=4.000.000. OpenFOAM=solid line, ANSYS CFX=broken line. 138

E.3 Lift-to-drag ratio normalized for the airfoil *NEWsym* at Re=4.000.000. OpenFOAM=solid line, ANSYS CFX=broken line. 139

F.1 Lift coefficient normalized for the airfoil *NEWthick* at Re=4.000.000. OpenFOAM=solid line, ANSYS CFX=broken line. 142

F.2 Drag coefficient normalized for the airfoil *NEWthick* at Re=4.000.000. OpenFOAM=solid line, ANSYS CFX=broken line. 142

F.3 Lift-to-drag ratio normalized for the airfoil *NEWthick* at Re=4.000.000. OpenFOAM=solid line, ANSYS CFX=broken line. 143

G.1 Mesh dependence study for an angle of attack of 0 degrees for the airfoil FX-77-W-400 at Re=4.000.000. 146

G.2 Mesh dependence study for an angle of attack of 8 degrees for the airfoil FX-77-W-400 at Re=4.000.000. 147

H.1 Mesh dependence study for an angle of attack of 0 degrees for the airfoil FB-3500-0875 at Re=666.000. 150

H.2 Mesh dependence study for an angle of attack of 8 degrees for the airfoil FB-3500-0875 at Re=666.000. 151

H.3 Mesh dependence study for an angle of attack of 16 degrees for the airfoil FB-3500-0875 at Re=666.000. 151

List of Tables

2.1 Summary of the properties of the most common numerical schemes. Data obtained from reference [19]. 18

4.1 Characteristics of the airfoils shown in 4.1 relative to the chord. . . 26

5.1 Characteristics of the airfoils shown in 5.1 relative to the chord. . . 49

6.1 Characteristics of the airfoils shown in 6.1 relative to the chord. . . 65
6.2 Comparison of the aerodynamic forces of the different airfoils specified at Re=666.000 and an angle of attack of 14 degrees. 83

7.1 Geometrical characteristics of the airfoils shown in 7.12 relative to the chord. 100

A.1 Results obtained for an angle of attack of 8 degrees the different meshes tried shown in figures A.1. AR=Aspect Ratio 121

Abstract

New airfoil designs are created in order to improve both the structural and aerodynamic properties of a wind turbine blade, one example of these are flatback airfoils. Furthermore, a new CFD programme exists in order to study the behavior of the flow around an airfoil, OpenFOAM. The flow around these new airfoils using OpenFOAM is studied in the present thesis. It is used the turbulence model k-ω SST for fully turbulent boundary layer and free transition at the boundary layer, modeled with the $Re_{\theta t} - \gamma$ transition model.

At the beginning of the present thesis the programme OpenFOAM is validated by doing different sensitivity studies on a thin airfoil (NACA0012) and then it is validated by comparing results obtained ANSYS CFX, Ellipsys and wind tunnel experiments. It is seen good agreement of OpenFOAM's results with these other results just mentioned.

It is seen that, making flatback airfoils which are very thick (with a relative thickness of 48 % and 57 %) by opening the trailing edge thickness the same percentage towards both pressure and suction side, much better aerodynamic characteristics are obtained. For example, while thickening the trailing edge of one airfoil 20 %, the lift coefficient is increasing 180 % and the lift-to-drag ratio 140 % for the range they are supposed to operate. While making flatback airfoils that are 35 % and 36 % thick relative to the chord, this increment in the lift-to-drag ratio is not observed. The behavior of the flow around a flatback airfoil is studied by increasing its chord into the dead water zone created behind the airfoil. The same pressure distribution on the wall of the modified versions is observed as for the former flatback airfoils. The friction coefficient is also very similar.

Thus, the flatback airfoils studied with OpenFOAM are profitable for the inner sections of the blade of a wind turbine, where very thick airfoils are found.

Preface

This report contains the results of the final thesis of the Wind Energy MSc at DTU (Technical University of Denmark, Kongens Lyngby). The thesis has been undertaken from the beginning of January to 1st July 2011 in Suzlon Blade Technology (SBT) in Aarhus (Denmark). It has a weight of 30 ECTS points. It has been supervised by associate Professor Martin O. L. Hansen from DTU-MEK and cosupervised by Ph.d. Mads Reck from Suzlon Blade Technology.

I wish to thank Martin O. L. Hansen and Mads Reck for all their support and advices during this thesis. I want to thank to General Manager of SBT Thomas Bjertrup Nielsen for giving me the opportunity to write my thesis in such a nice team and environment. Specially, I would like to thank to Ph.d. Peter Bjørn Andersen and Ph.d. Alejandro Gómez Gonzalez for all the fruitful discussions during the development of this thesis. I want to thank to professor Niels N. Sørensen for the conversations maintained in order to solve some of the problems during the development of the thesis and for the data given for doing comparisons shown. I also want to thank to Felix Langfeldt for the advices about OpenFOAM and for giving me the key to perform the study done. Finally, I want to thank to Risø for lending me computational resources in the Alfheim cluster.

No puedo entregar este proyecto sin agradecer a mi familia su apoyo durante toda mi carrera. En especial a mis padres y mis hermanas por estar siempre presentes y a mis abuelos por el ejemplo que me han dado. Quiero también agradecer a mis amigos por los buenos momentos compartidos durante la carrera, *Amics Tarragona*, *Industriales Penyafort* y al *Timbia Team* y *HH* ya que sin ellos no hubiera disfrutado como lo he hecho de mi estancia en Dinamarca.

Suzlon Blade Technology
Aarhus, July 1st, 2011

José María Milián Sanz, Pepe

Chapter 1

Thesis introduction

The demand of energy production from renewable energies such as wind turbines has increased a lot during the last 25 years. Thus, the small wind turbines offered in the early days of the wind energy industry with a power capacity of 20-30 kW have been improved to obtain wind turbines giving a capacity of 3-5 MW, or even 7.5 MW ([14]). It is well known that this increase in nominal power given, related with an increase of the size of the turbine, involves an increase of the loads on the wind turbine components.

The wind energy industry is working hard on research for solutions to support these loads while maintaining this high annual energy production achieved. The option which is being investigated by some companies and research centers are the flatback airfoils. The trailing edge of these airfoils is opened towards pressure and/or suction side in order to modify the airfoil properties.

These blunt trailing edge airfoils basically increase both the sectional area and the sectional moment of inertia, thus reducing weight and optimizing structural material placement and blade strength, as it is shown in [1]. Thus, they are a very good option to be situated at the root of the blade (where the thickest sections are found) because it is well known that inboard sections have to be designed to provide more structural performance, while outboard sections are thought to give better aerodynamic characteristics. In [1] they also comment the better manufacturing of these airfoils with thicker trailing edge. Furthermore, thick flatback airfoils are supposed to be less sensitive to surface soiling, as it is stated in [1]. Nevertheless, due to the vortex formation at the trailing edge they generate more drag and low frequency noise with higher intensity as stated in [7]. This is another beneficial reason for these flatback airfoils at the inner part of the blade, where the lower relative velocities are found. Studies have been made to decrease this negative effect, including modifications like addition of a splitter plate (with both serrated and not serrated shape at the end), which can reduce the overall drag by 50 % ([4]) and create less intensity noise with higher frequencies ([7]).

In order to know about the aerodynamic performance of these airfoils wind tunnel experiments or Computational Fluid Dynamics (CFD) have to be done. Sandia Laboratories from California ([2]), shows the results for wind tunnel experiments on thick flatback airfoils, the airfoil FB-3500-0050 and the modifications made to its trailing edge (by opening its trailing edge the same percentage towards both pressure and suction side). CFD has also been used by Sandia Laboratories in order to study these airfoils in [9]. In reference [6] the airfoil DU-97-W-300 is studied using CFD. Another MSc thesis ([5]) has been done in order to study with CFD the performance of the airfoils FB-3500-0050 and DU-97-W-300 and the modifications made to their trailing edges.

Risø DTU modificated the airfoil DU-97-W-300 by increasing differently the trailing edge towards the upper or the lower side and does CFD on them ([27]). These results show the drag increases generally to the same level for all of these modifications they did. On the other hand, the lift coefficient increases while opening the trailing edge more towards the pressure side than the suction side, which is actually a camber increase.

In this thesis it was decided to increase the thickness of the trailing edge of the thick airfoils studied. In the cases studied in this thesis the trailing edge is thickened the same percentage towards both pressure and suction side in order to see how this is affecting the aerodynamic performance.

Along side with the study of flatback airfoils already explained, it has been done a lot of investigation on the performance of the free and open CFD code OpenFOAM. This study is going to be realized with the software OpenFOAM (v1.7.1). Before doing that, results for thick and thick flatback airfoils are going to be compared with results obtained with commercial CFD softwares, ANSYS CFX (v13.0) and Ellipsys. Initially different sensitivity studies for a thin airfoil (NACA0012) are performed in order to validate the results obtained with OpenFOAM. Thus, once the programme OpenFOAM has been validated, the study of flatback airfoils is started.

The current thesis is answering two main questions:

1. Is OpenFOAM a reliable software to be used for steady analysis of 2-D airfoils?

2. By flatbacking thick airfoils, is there an improvement in the aerodynamic performance of these?

Chapter 2

Theory

In this chapter it is going to be explained the basis of the theoretical aspects regarding the computations done. It is summarized in a few subchapters and they are cited some references where it can be found a deeper explanation and development of the theoretical aspects and equations shown.

2.1 The Navier-Stokes Equations

Newton's second law applied to a fluid particle yields to equation 2.1.

$$\rho \frac{DV}{Dt} = f = f_{body} + f_{surface} \tag{2.1}$$

The body forces, f_{body}, are the ones applied to the entire mass of the fluid element studied, i.e. gravitational forces or magnetohydrodynamic forces are not considered in the different studies done. Thus, these body forces considered are $f_{body} = \rho g$. The surface forces, $f_{surface}$, are the forces applied by external stresses τ_{ij} on the side of the fluid element. This τ_{ij} is a stress tensor that is written as it is shown in equation 2.2, the terms appearing are shown in figure 2.1.

$$\tau_{ij} = \begin{pmatrix} \tau_{xx} & \tau_{xy} & \tau_{xz} \\ \tau_{yx} & \tau_{yy} & \tau_{yz} \\ \tau_{zx} & \tau_{zy} & \tau_{zz} \end{pmatrix} \tag{2.2}$$

Then, taking into account the front faces shown in figure 2.1 the surface force in the x direction is shown in equation 2.3. The surface forces for directions y and z are not given because they can be obtained by analogy to equation 2.3.

$$dF_x = \tau_{xx} dydz + \tau_{yx} dxdz + \tau_{zx} dxdy \tag{2.3}$$

Taking into account that in the x-direction equation 2.4 is fulfilled, the net force at the element at this direction is shown in equation 2.5.

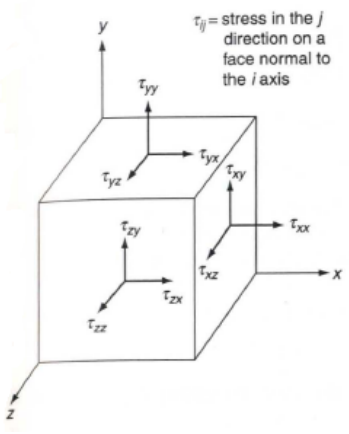

Figure 2.1: Notation used to obtain the stress tensor. Obtained from reference [17]

$$\tau_{xx,front} = \tau_{xx,back} + \frac{\partial \tau_{xx}}{\partial x} dx \tag{2.4}$$

$$dF_{x,net} = \left(\frac{\partial \tau_{xx}}{\partial x} dx\right) dydz + \left(\frac{\partial \tau_{yx}}{\partial y} dy\right) dxdz + \left(\frac{\partial \tau_{zx}}{\partial z} dz\right) dxdy \tag{2.5}$$

Equation 2.5 on a unit volume basis (dividing by dxdydz) becomes equation 2.6, which is equivalent to take the divergence of the vector $(\tau_{xx}, \tau_{xy}, \tau_{xz})$.

$$f_x = \frac{\partial \tau_{xx}}{\partial x} + \frac{\partial \tau_{yx}}{\partial y} + \frac{\partial \tau_{zx}}{\partial z} \tag{2.6}$$

Thus, applying equation 2.6 similarly in directions y and z it yields to equation 2.7. This is the equation to calculate the surface force for all the directions.

$$f_{sur} = \nabla \cdot \tau_{ij} = \frac{\partial \tau_{ij}}{\partial x_j} \tag{2.7}$$

Finally, taking into account equation 2.8, for incompressible flow, they are obtained the Navier-Stokes equations, shown in equation 2.9. These are the Navier-Stokes equations for incompressible flow and constant viscosity, where V corresponds to the velocity vector $V = (u, v, w)$, yielding one momentum equation for each direction.
The equation 2.8 shown is taken from reference [17].

$$\tau_{ij} = -p\delta_{ij} + \mu \left(\frac{\partial u_i}{\partial x_j} + \frac{\partial u_j}{\partial x_i}\right) \tag{2.8}$$

where, $\delta_{ij} = 1$ if $i = j$ and $\delta_{ij} = 0$ if $i \neq j$.

$$\rho \frac{DV}{Dt} = \rho g - \nabla p + \mu \nabla^2 V \tag{2.9}$$

2.2 Reynolds number

The Reynolds number is a dimensionless number giving a ratio of the inertial forces and the viscous forces in a flow. The equation of the Reynolds number is shown on equation 2.10. It is used in fluid dynamics to state if the fluid being studied is laminar or turbulent. For external flow this limit at which the fluid changes from laminar to turbulent is depending in several aspects as the roughness or the curvature of the surface of the body studied. For example, for a flat plate the limit is for $Re = 5x10^5$ as it is stated in reference [28].

$$Re = \frac{Ul}{\nu} \tag{2.10}$$

where, U is the speed of the incoming flow, l is the chord of the airfoil and ν is the kinematic viscosity of the flow. In order to state the Reynolds number for a case studied with a given chord length and a given velocity of the incoming flow, the value of ν has to be fixed according to equation 2.10.

2.3 Reynolds Averaged Navier-Stokes equation, RANS

The flow at which the wind turbines are operating is turbulent. Thus, the velocity studied will be composed by an averaged component ($\overline{u}$) and a fluctuation in (u'), as it is shown in equation 2.11. By similarity, they can be also obtained the velocities for the other two directions, v and w. Also, the pressure in a turbulent flow is shown in equation 2.12.

$$u = \overline{u} + u' \tag{2.11}$$

$$p = \overline{p} + p' \tag{2.12}$$

In the RANS modeling, equations 2.11 and 2.12 are inserted into equation 2.9. Thus, the resulting equation is averaged to yield equation 2.13, which is an equation expressing momentum conservation for the averaged motion.

$$\rho \frac{D\bar{V}}{Dt} + \rho \frac{\partial}{\partial x_j} \left(\overline{u_i' u_j'} \right) = \rho g - \nabla \bar{p} + \mu \nabla^2 \bar{V} \tag{2.13}$$

The equation 2.8 of the shear stress is rearranged as it is shown in equation 2.15 and the turbulent inertia terms are shown as if they were stresses. For a 2D flow, this new term $-\rho\overline{u'v'}$ is called the *turbulent shear*.

$$\tau_{ij} = -p\delta_{ij} + \mu\left(\frac{\partial u_i}{\partial x_j} + \frac{\partial u_j}{\partial x_i}\right) - \rho\overline{u_i'v_j'} \tag{2.14}$$

This new term mentioned can not be neglected in any case modeling turbulent flow and it creates analytical difficulties to the calculation of the flow. J. Boussinesq in 1877 made the assumption of modeling this as a gradient diffusion term, making an analogy to the molecular shear as it is shown in equation 2.15 for a 2D flow.

$$\tau_t = -\rho\overline{u'v'} = \mu_t\frac{\partial\overline{u}}{\partial y} \tag{2.15}$$

where μ_t is the eddy viscosity. This is not a property of the fluid, it varies depending on the geometry and the flow conditions. In order to be able to compute a solution for the momentum equations, a solution for ν_t (shown in equation 2.16) has to be found. Thus, in order to model it there have been developed different turbulence models, these are explained in the section 2.4.

$$\nu_t = \frac{\mu_t}{\rho} \tag{2.16}$$

2.4 Turbulence modelling

In order to model the turbulence in the present study they are used both Spalart-Allmaras turbulence model (1-equation model) and $k-\omega$ SST turbulence model (2-equations model), although more turbulence models are available in OpenFOAM. Beforehand, the $k-\omega$ SST turbulence models is supposed to give better results, mainly at the stall region, because it leads to major improvements in the prediction of adverse pressure gradient flows, as it is written in reference [13].

Spalart-Allmaras turbulence model

In order to get the eddy viscosity using this turbulence model they have to be solved the equations in 2.17 using equation 2.18, as it is shown on [12].

$$\nu_t = \tilde{\nu}f_{v1}, f_{v1} = \frac{\chi^3}{\chi^3 + C_{v1}^3}, \chi = \frac{\tilde{\nu}}{\nu} \tag{2.17}$$

$$\frac{\partial \tilde{\nu}}{\partial t} + u_j \frac{\partial \tilde{\nu}}{\partial x_j} = C_{b1}\left(1 - f_{t2}\right)\tilde{S}\tilde{\nu} + \frac{1}{\sigma}\left\{\frac{\partial}{\partial x_j}\cdot\left((\nu + \tilde{\nu})\frac{\partial}{\partial x_j}\tilde{\nu}\right) + C_{b2}|\frac{\partial \tilde{\nu}}{\partial x_i}\frac{\partial \tilde{\nu}}{\partial x_i}\right\} - \\ - \left[C_{w1} f_w - \frac{C_{b1}}{\kappa^2} f_{t2}\right]\left(\frac{\tilde{\nu}}{d}\right)^2 \tag{2.18}$$

where the functions and constants not specified appearing on equations 2.17 and 2.18 can be found in [12].

While preparing the case to run the computations with this model they have to be introduced the initial conditions on the different boundaries for $\tilde{\nu}$, these are defined based on the reference [12]. The values of ν_t are set as *calculated*, thus no boundary condition has to be given for this variable, but the one at the wall, which is set to a value of 0.
$\tilde{\nu}$ is defined as follows,
- $\tilde{\nu}_{wall} = 0$
- $\tilde{\nu}_{inlet} = 3\nu_\infty : 5\nu_\infty$, based on reference [12]
- $\tilde{\nu}_{outlet} = zeroGradient$

$k - \omega$ SST turbulence model

In order to get the desired eddy viscosity using this model it has to be solved the equation 2.19, from reference [12].

$$\nu_t = \frac{a_1 k}{max(a_1\omega, SF_2)} \tag{2.19}$$

where the turbulent kinetic energy, k, and the specific dissipation rate, ω, are obtained solving the equations 2.20 and 2.21, respectively.

$$\frac{\partial k}{\partial t} + \frac{\partial u_j k}{\partial x_j} = P - \beta^* k\omega + \frac{\partial}{\partial x_j}\left[(\nu + \sigma_k \nu_t)\frac{\partial k}{\partial x_j}\right] \tag{2.20}$$

$$\frac{\partial \omega}{\partial t} + \frac{\partial u_j \omega}{\partial x_j} = \frac{\gamma}{\nu_t} P - \beta\omega^2 + \frac{\partial}{\partial x_j}\left[(\nu + \sigma_\omega \nu_T)\frac{\partial \omega}{\partial x_j}\right] + 2\left(1 - F_1\right)\sigma_{\omega 2}\frac{1}{\omega}\frac{\partial k}{\partial x_j}\frac{\partial \omega}{\partial x_j} \tag{2.21}$$

The boundary conditions imposed to the computations performed using this turbulence model are listed below. These are based on the well known turbulent kinetic energy equation, the eddy viscosity ratio for such external flows and the equations of the boundary conditions for ω_{inlet} from reference [13].
- $k_{inlet} = \frac{3}{2}\left(U_\infty \cdot T_i\right)^2$
- $\nu_{Tinlet} = (1 \to 10)\nu_\infty$
- $\omega_{inlet} = \frac{k_{inlet}}{\nu_{Tinlet}}$
- $\omega_{inlet} = (1 \to 10)\frac{U_\infty}{L}$

where L is the approximate length of the computational domain.
When one develops these equations for ω_{inlet} it is seen that the different two equations given do not fit with each other. For example, a Reynolds number of 3.000.000 and a turbulence intensity of 0.07% would yield to a range of $0.22 < \omega_{inlet} < 2.22$ 1/s. At the same time, for a $U_\infty = 1\ m/s$ and a length of the computational domain of 120 meters, it is obtained a range of $0.008333 < \omega_{inlet} < 0.08333$ 1/s. This is a minor problem though because as it is said in the paper where Menter presented the $k-\omega$ SST turbulence model [13] the results obtained with this turbulence model are independent of ω_{inlet}. Furthermore, it has been tested for different parameters of ω_{inlet} with OpenFOAM and the solution obtained for the force coefficients on the airfoil did not change.
The boundary conditions at the outlet and the wall are given below.
- $k_{outlet} = \omega_{outlet} = zeroGradient$
- $\nu_{twall} = k_{wall} = 0$
- $\omega_{wall} = 10\frac{6\nu}{\beta_1(\Delta y_1)^2}$

In OpenFOAM there is one tool called *omegaWallFunction* that takes care that this last condition is fulfilled. Even though it is called "wall function" it does not apply any wall function, it just applies this boundary condition from reference [13].

The boundary condition of ν_t is set to calculated as it was done for the cases run using the Spalart-Allmaras turbulence models.

2.5 Transition prediction model

Laminar and turbulent boundary layer

The flow found around an airfoil presents a velocity profile due to the velocity is changing from 0 velocity at the wall to the freestream velocity. The boundary layer is the region where the flow changes from 0 velocity to a velocity which is 99% of the free stream velocity. While studying the boundary layer around an airfoil it can be seen that there is a region where this boundary layer is laminar and then, there is one position where they are generated vortexes and the boundary layer from that point is called turbulent. There is one very small zone called transition region, where it is not perfectly defined whether the boundary layer is laminar or turbulent, the point where this region starts is called transition point. In order to show it, it is plot the boundary layer on a flat plate in figure 2.2.

Brief explanation of the transition prediction model used

In order to model the different types of boundary layer present on the airfoils studied it is used the transition model of reference [20]. In this point it is

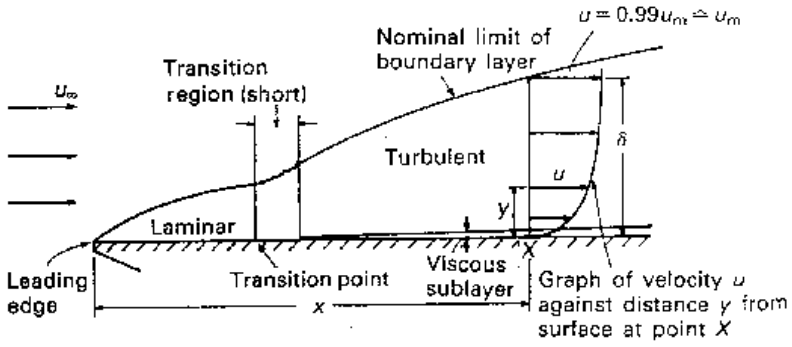

Figure 2.2: Boundary layer on a flat plate. y scale greatly enlarged. Obtained from reference [22].

given a summary of the explanation given in the reference mentioned. The transition prediction model used is a two equations model. The first one, called intermittency equation γ is used to trigger the transition process, it is used to control the production of turbulent kinetic energy in the boundary layer. The second equation is based on the transition Reynolds number $Re_{\theta t}$. Thus, the model relates the local momentum thickness Reynolds number Re_θ (shown in equation 2.23) with the critical value $Re_{\theta c}$ and when Re_θ is larger than this critical value, it switches on the production of turbulent kinetic energy.

$$Re_\nu = \frac{\rho y^2}{\mu}\frac{\partial u}{\partial y} = \frac{\rho y^2}{\mu}\Omega \tag{2.22}$$

$$Re_\theta = \frac{Re_{\nu,max}}{2.193} \tag{2.23}$$

The first equation that the model is using, the intermittency equation γ, is shown in equation 2.24. The values of γ are in the range $0 < \gamma < 1$, where the lowest values are related to the cells where the k production term is turned on. Thus, the transition model used is coupled with the $k-\omega$ SST turbulence model.

$$\frac{\partial(\rho\gamma)}{\partial t} + \frac{\partial(\rho U_j\gamma)}{\partial x_j} = P_{\gamma 1} - E_{\gamma 1} + P_{\gamma 2} - E_{\gamma 2} + \frac{\partial}{\partial x_j}\left[\left(\mu + \frac{\mu_t}{\sigma_f}\right)\frac{\partial\gamma}{\partial x_j}\right] \tag{2.24}$$

where the terms appearing in this equation not given can be found in reference [20].

The boundary conditions to be used for this equation are given in [20]. These are:
- $\gamma_{wall} = zeroGradient$, i.e. zero normal flux.
- $\gamma_{inlet} = 1$.
- $\gamma_{outlet} = zeroGradient$.

The second equation used, the transport equation for the transition momentum thickness Reynolds number $\widetilde{R}e_{\theta t}$ is shown in equation 2.25.

$$\frac{\partial\left(\rho\widetilde{R}e_{\theta t}\right)}{\partial t}+\frac{\partial\left(\rho U_j\widetilde{R}e_{\theta t}\right)}{\partial x_j}=P_{\theta t}+\frac{\partial}{\partial x_j}\left[\sigma_{\theta t}\left(\mu+\mu_t\right)\frac{\partial\widetilde{R}e_{\theta t}}{\partial x_j}\right] \tag{2.25}$$

where the terms appearing in this equation not given can be found in reference [20].

The boundary conditions to be used for this equation are given in [20]. These are:
- $\widetilde{R}e_{\theta t,wall} = zeroGradient$, i.e. zero normal flux.
- $\widetilde{R}e_{\theta t,outlet} = zeroGradient$.
- $\widetilde{R}e_{\theta t,inlet}$ is calculated from an empirical correlation based on the inlet turbulence intensity. This is found in reference [20].

P_γ from equation 2.24 has two terms, both $Re_{\theta c}$ and F_{length}, that are not given in reference [20] due to proprietary reasons, these are the terms that ANSYS CFX uses in its computations. The equations for these two terms just mentioned given by Sørensen in [24] have been used in the computations performed with OpenFOAM.

Best practices for using the transition model

Using the transition model explained requires approximately 18 percent additional CPU time compared to simulations with the $k-\omega$ SST turbulence model without transition model applied as it is stated in the appendix "Best Practice Guidelines for Using the Transition Model" of reference [20]. Thus, it has been studied whether the transition model is actually necessary for the airfoils studied or not.

The recommendations that can be found in the appendix just mentioned and that are applied for the meshes used are:
- $Max(y^+)$. Depending on the angle of attack of the polar curve that is being computed, it is found a different $max(y^+)$ because of the different velocities found in the cell closest to the wall. However, $max(y^+)$ is always between 0,5 and 2 and, as it is seen in the recommendations given, the solution is not affected because of this difference.
- Wall normal expansion ratio between 1.05 and 1.1. An expansion ratio of

1.6 has been used
- $75 - 100$ streamwise grid points from the leading edge to the trailing edge. $120 - 150$ grid points have been used, which does not affect the solution, the range specified is for the minimum number of grid points to use.
- It is desirable to have a relatively low viscosity ratio (between 1 and 10). An eddy viscosity ratio of 10 has been used.
- It is recommended to estimate the turbulence intensity at the inlet based on the turbulence intensity at the leading edge, based on the decay rate. This has not been taken into account, the turbulence intensities at the inlet has been based on the turbulence intensities used at the references shown, (i.e. boundary conditions of the wind tunnel experiments and Ellipsys computations).

2.6 Near wall treatment

The wall is the main source of turbulence in external flows. This is the reason why a lot of effort has to be put to model accurate enough the flow in the zone closed to the walls. Figure 2.3 shows the different layers in how the boundary layer is subdivided when the flow around the body studied is turbulent. The parameters u^+ and y^+ that are shown are presented in equations 2.26 and 2.27 respectively.

$$u^+ = \frac{\overline{u}}{u_*} \tag{2.26}$$

where $\overline{u}$ is the mean velocity of the flow and u_* is the friction velocity defined as $u_* = (\frac{\tau_w}{\rho})^{\frac{1}{2}}$. τ_w is the wall shear stress defined as $\tau_w = \mu \left(\frac{\partial u}{\partial y}\right)_{y=0}$.

$$y^+ = \frac{u_* y}{\nu} \tag{2.27}$$

where y is the distance to the nearest wall.

The behavior of the flow in the boundary layer is different depending on the distance to the wall.

Inner layer

Also called viscous sublayer. It corresponds to part of the boundary layer closest to the wall, where the flow is mostly affected by the viscous shear. In this region $u_+ = y_+$, as it is shown in figure 2.3. The limit is found at $y_+ < 5$. Thus, from equation 2.27 its thickness is $\delta_{sub} = 5\frac{\nu}{u_*}$.

Log layer

Also called the overlap layer. In this region both the effects of the viscous and the turbulent shear are important. It corresponds to a profile that smoothly connects the inner and the outer regions. It exists a logarithmic relation in

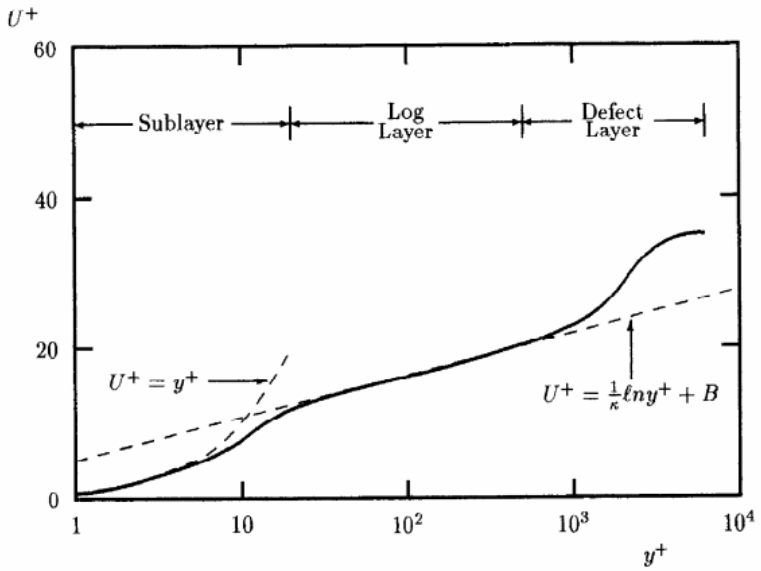

Figure 2.3: Typical velocity profile of a turbulent boundary layer. Obtained from reference [18]

this region between u^+ and y^+ for $35 < y^+ < 350$, this upper limit depends in the Reynolds number though.

Between this layer and the viscous sublayer, it exists a region called buffer layer or blending region, for $5 < y^+ < 30$. In this region the profile is neither linear nor logarithmic, it is a merger between the two.

Outer layer

Also called the defect layer. It corresponds to the part of the boundary layer closest to the freestream, which is mostly affected by the inertia effects and the turbulent shear.

CFD and the near wall treatment

In the RANS models there are two ways of solving the flow near the wall using CFD, these are the Low-Re RANS models and the High-Re RANS models. In the Low-Re RANS models the region very close to the wall ($y^+ \approx 1$) is solved. In the High-Re RANS models the region near the wall (up to $y^+ \approx 30$) is modeled by the use of wall functions. Thus, for meshes with $y^+ > 11.63$, the nodes closer to the wall are considered to be inside the log-law region and the wall functions should be used in order to model the behavior of the flow in this region. This is shown in figure 2.4. Every model has its advantages and inconveniences, doing the Low-Re RANS modeling one is sure that the flow is solved down to the wall and that no modeling is done by the wall functions.

On the other hand, the High-Re RANS models are better because cells can be saved in the meshing due to the higher y^+ needed.

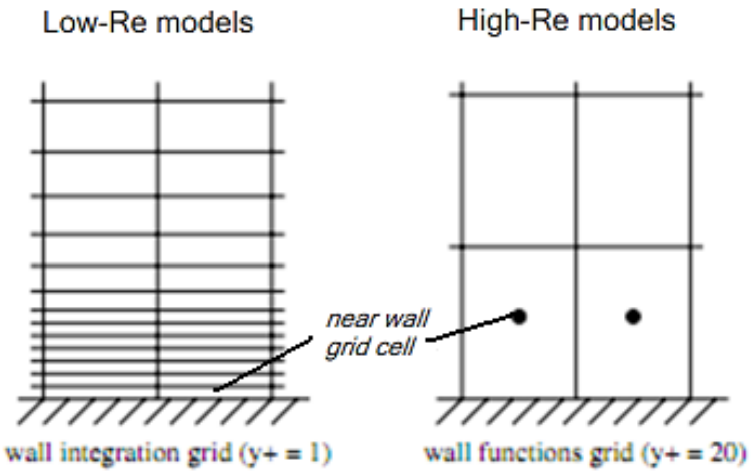

Figure 2.4: Possibilities of near wall treatment in CFD. Obtained from reference [21].

Depending on the software used these wall functions can be turned on, turned off or it can be used a hybrid modeling, where they are turned on automatically if necessary ($y^+ > 11.63$). While running the software with the wall functions turned off, as it has been done in the cases presented, they should be used meshes with $y^+ < 2$. In chapter 4.4 this limit will be studied, where a sensitivity study for y^+ is done in order to know how this choice affects the solution obtained.

2.7 Airfoil parameters

In order to describe the geometry of an airfoil it is always used a geometry file giving the coordinates of the upper and lower surfaces. There are some parameters that describe how an airfoil looks like, these are shown in figure 2.5.

The chord of the airfoil corresponds to the straight line connecting the leading and trailing edges of the airfoil. The thickness is the distance from the upper to the lower surface. Usually thickness is given in relative terms (relative to the chord of the airfoil) and the main interest usually is on the maximum thickness and its location in percentage of chord. The mean line or camber line corresponds to an equidistant line to both upper and lower surfaces. The main interest when looking at it is the shape of this camber

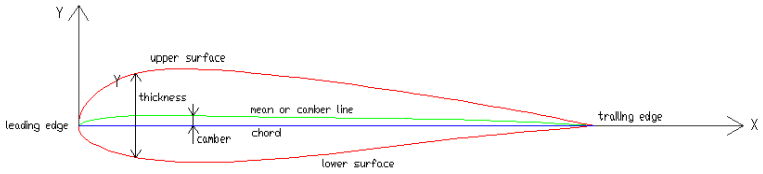

Figure 2.5: Parameters describing the geometry of an airfoil.

line, the maximum camber (relative to the chord) and the location of this maximum camber, also in percentage of chord.

Since flatback airfoils are studied in this thesis the percentage of trailing edge relative to the chord of the airfoil is also an important parameter to consider when describing the airfoils studied.

In the different chapters of this report, where different airfoils are studied, their parameters are given.

During this thesis they are studied two NACA four-digit airfoils (NACA0012 and NACA8648). The different digits of this nomenclature, based on [33] correspond to:
1- Maximum camber in percentage of the chord.
2- Position of the maximum camber in tenths of the chord.
3, 4- Maximum thickness of the airfoil in percentage of the chord.

Thus, for example the airfoil NACA8648 corresponds to one airfoil with a maximum thickness of 48 % (relative to the chord) and a maximum camber of 8 % situated at 60 % of the chord of the airfoil. NACA four-digit airfoils have been generated with XFOIL, which is explained briefly in section 2.10. This programme uses the equations given in [33] in order to generate them.

2.8 Force Coefficients

The aerodynamic force is the force done by the air to a body moving with a relative speed in it. This is composed of both a pressure and a viscous component. In the case of airfoils the viscous component of this aerodynamic force is smaller than the pressure component. However, for low angles of attack this viscous component may not be negligible compared to the pressure component.

This aerodynamic force is decomposed in the lift force, which is the component perpendicular to the movement of the airfoil, and the drag force which is the component parallel to the movement airfoil and opposite to it. They are shown in figure 2.6.

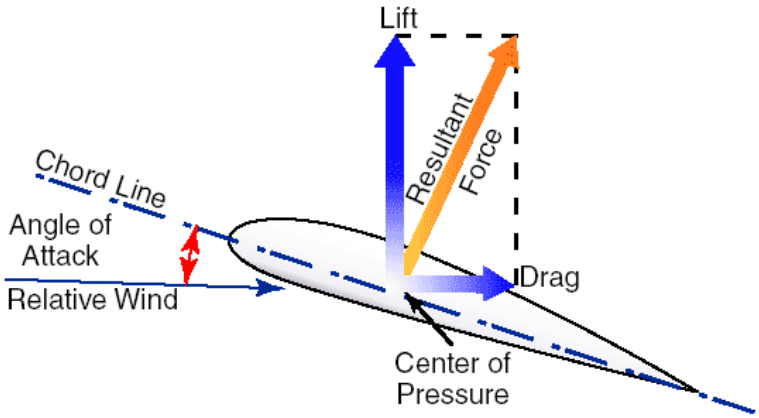

Figure 2.6: Aerodynamic forces on an airfoil. Obtained from reference [23].

These aerodynamic forces are made non-dimensional by using the dynamic pressure shown in equation 2.28.

$$q = \frac{1}{2}\rho v^2 \tag{2.28}$$

Thus, the lift and drag coefficients studied during this report are calculated using equations 2.29 and 2.30, respectively.

$$C_L = \frac{L}{qA} = \frac{L}{\frac{1}{2}\rho v^2 A} \tag{2.29}$$

$$C_D = \frac{D}{qA} = \frac{D}{\frac{1}{2}\rho v^2 A} \tag{2.30}$$

2.9 Numerical schemes

There are different numerical schemes one can choose to perform the CFD calculations. The equation 2.13 presents both convection and diffusion terms. Such a equation for a steady one-dimensional convection and diffusion of a property ϕ is shown on 2.31, it is taken into account that the flow fulfills the continuity equation, thus $\frac{d(\rho u)}{dx} = 0$. The explanation given refer to a 1D case in steady state in order to simplify the equations written. However, it will be sufficient enough to comment the main characteristics of the different numerical schemes.

$$\frac{d}{dx}(\rho u \phi) = \frac{d}{dx}\left(\Gamma \frac{d\phi}{dx}\right) \tag{2.31}$$

In figure 2.7 it is shown the nomenclature that it is going to be used in the explanation below, i.e. P refers to the node representing the element

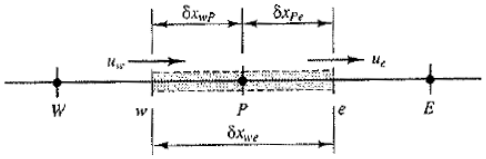

Figure 2.7: Control volume around a node P. Obtained from [19].

studied, W and E refer to the west and east nodes, respectively. On the other hand, w and e refer to the west and east faces of this node P studied. The points used in order to calculate the desired derivative at a point x_0 are called stencil points (r). The number of points situated at the left of the point x_0 is known as a and the number of points at the right of this point is b. Thus, $r = a+b+1$, since the point x_0 is also used to calculate the desired derivative. While refining one grid with a cell width of Δx, it can be seen that the error tends to Δx^{r-1} as $\Delta x \to 0$, as it is explained in [16]. Thus, it is said that the accuracy is a $(r-1)$th order.

They are defined two new variables in order to get discretised equations for the ones shown above. These are shown in 2.32.

$$F = \rho u \quad , \quad D = \frac{\Gamma}{\delta x} \tag{2.32}$$

These ones referred to the cell faces explained above are shown in equation 2.33 and 2.34.

$$F_w = (\rho u)_w \quad , \quad F_e = (\rho u)_e \tag{2.33}$$

$$D_w = \frac{\Gamma_w}{\delta x_{WP}} \quad , \quad D_e = \frac{\Gamma_e}{\delta x_{PE}} \tag{2.34}$$

These variables defined will be introduced in the integrated forms of both the transport and continuity equations shown in 2.35 and 2.36, respectively.

$$(\rho u A \phi)_e - (\rho u A \phi)_w = \left(\Gamma A \frac{\delta \phi}{\delta x}\right)_e - \left(\Gamma A \frac{\delta \phi}{\delta x}\right)_w \tag{2.35}$$

$$(\rho u A)_e - (\rho u A)_w = 0 \tag{2.36}$$

Thus, considering that $A_w = A_e = A$ they are obtained the integrated forms of both the convection-diffusion equation and the continuity equation in terms of the coefficients 2.33 and 2.34. These are shown in equation 2.37 and 2.38

$$F_e \phi_e - F_w \phi_w = D_e(\phi_E - \phi_P) - D_W(\phi_P - \phi_W) \tag{2.37}$$

$$F_e - F_w = 0 \tag{2.38}$$

Properties of the numerical schemes

Conservativeness

One numerical scheme is conservative if conservation of a flux ϕ for the entire solution domain is ensured, i.e. the flux of ϕ leaving a control volume has to be the same as the flux entering the adjacent one. In order to show this, they are shown figures 2.8 and 2.9, representing a central difference scheme (CDS) and a scheme using a quadratic interpolation formula, respectively. In both cases a one-dimensional steady state diffusion problem without source terms is considered.

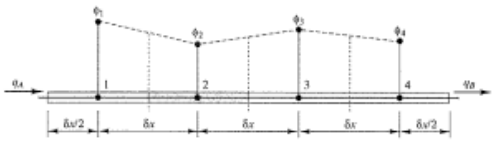

Figure 2.8: Gradients at the faces for a linear scheme. Obtained from [19].

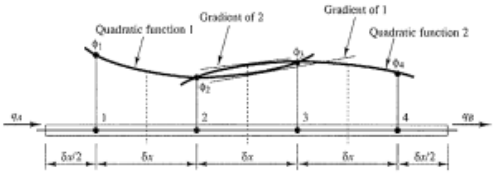

Figure 2.9: Gradients at the faces for a quadratic scheme. Obtained from [19].

The flux leaving cell 2 in figure 2.8 is $\Gamma_{e2}(\phi_3 - \phi_2)/\delta x$ and the flux entering to cell 3 is $\Gamma_{w3}(\phi_3 - \phi_2)/\delta x$, where Γ is the diffusion coefficient and $\Gamma_{ei} = \Gamma_{w(i+1)}$. A balance of the flux between nodes 1 and 4 is done in order to check the conservativeness of this scheme. It can be easily seen that the gradients at the faces between two cells are equal all over the domain. Thus, while doing the mentioned balance it will be obtained $q_B = q_A$. Thus, it is shown that CDS is conservative. On the other hand, this other scheme considered using a quadratic interpolation formula is not conservative since the gradients at the faces between two cells are not equal, i.e. the gradient at the faces is slightly different, which makes the scheme shown in figure 2.9 not conservative.

Boundedness

In order to solve the CFD cases run, a set of discretised equations has to be solved at each nodal point. One scheme is bounded when, without sources, the internal nodal value of ϕ is bounded by its boundary values (i.e. in a steady state conduction problem with boundary temperatures of 100° C and 200° C, all the values found in the domain will be between these values). Unbounded numerical schemes may find overshoots and undershoots affecting the stability and the accuracy of the solution. The mathematical explanation for when this property is fulfilled is explained in reference [19].

Transportiveness

The numerical schemes that take into account the direction of the flow fulfill this transportiveness property. Thus it is said that if a numerical scheme takes into account the relationship between the Peclet number (ratio between convection and diffusion) and the directionality of influencing, this fulfills the transportiveness property.

In reference [19] they are explained very detailed the properties for the most common numerical schemes. It is given a summary in table 2.1.

	Order	Conservative	Bounded	Transportiveness
CDS	2nd	YES	not for Pe>2	NO
Upwind	1st	YES	YES	YES
Linear Upwind	2nd	YES	YES	YES
QUICK	3rd	YES	YES	YES

Table 2.1: Summary of the properties of the most common numerical schemes. Data obtained from reference [19].

2.10 XFOIL

XFOIL is a program used for the analysis of subsonic isolated airfoils (i.e. 2D airfoils). It is not using CFD (Computational Fluid Dynamics), but the panel method. This is solving the boundary layer equations. The general XFOIL methodology is explained in [34]. It is also used in order to design or redesign isolated airfoils. During the development of this thesis it has been used for the following aspects:

1. Viscous analysis of some of the airfoils studied with free transition at the boundary layer in order to obtain lift and drag curves just beyond

CL_{max}, pressure coefficient curves, transition location points.

2. Design of NACA four-digit airfoils using the definition explained in [33].
3. Redesign of airfoils in order to obtain the desired flatback airfoils of them, opening the trailing edge towards both pressure and suction side. This is detailed in section 2.11
4. Normalize a given airfoil to unit chord.
5. Get the airfoil parameters explained in 2.7.

This program can also be used in order to solve the flow around an airfoil with a blunt trailing edge, as it is specified in the manual of the programme [35], where it is mentioned a study found in [36].

2.11 Creating the flatback airfoils

A flatback airfoil is an airfoil that maintaining the same chord length, the trailing edge is opened towards both pressure and suction side or to one of those.

The openings in the trailing edge have been done the same percentage relative to chord to both pressure and suction sides of the airfoil. Thus, it was decided to do computations on airfoils opened the same distance to both sides to see how this is affecting to the aerodynamic performance of the airfoil. The reason of this decision is explained later in chapter 7.

The mentioned flatback airfoils have been created using the tool *TGAP* of XFOIL. This one, for a given trailing edge thickness in relative terms (t/c) and a bending distance (x_b), shown in figure 2.10, creates a flatback airfoil with a trailing edge opened equally to both pressure and suction sides. The tool *TGAP* of XFOIL is working based on equation 2.39, which gives the displacement vector applied on every point of the airfoil. Because of the openings done to the trailing edge of the airfoils studied, the thickness and camber is modified slightly (between 1 and 4 %), these changes are specified for all the flatback airfoils studied. Figure 2.10 shows the parameters used in equation 2.39.

$$\overrightarrow{\delta r} = \frac{\delta t}{2} \cdot \overrightarrow{r_t} \cdot \gamma \tag{2.39}$$

where,
$\gamma =< x > \beta =< x > e^{-\tau}$
$\tau = (c- < x >) \left(\frac{1}{x_b} - 1\right)$
$< x >= \frac{x}{c}$
$\delta t = \tilde{t} - t$, which is the difference between the old and the new trailing edge thickness, in absolute terms.

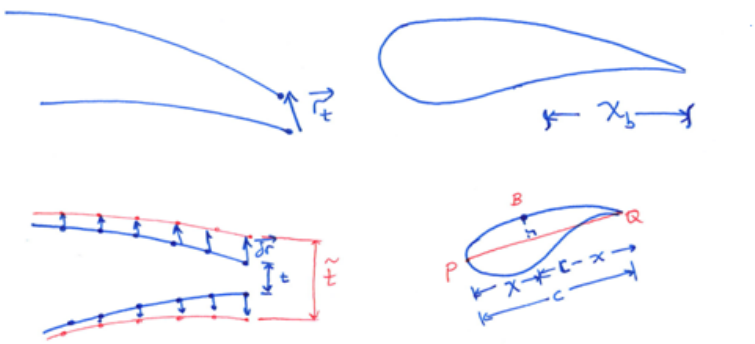

Figure 2.10: Sketch of the parameters used by the function *TGAP* of XFOIL. Created by Alejandro Gómez.

Chapter 3

Meshing

In order to mesh the domain studied, the software ANSYS ICEM HEXA is being used. It is done an O-mesh mesh since it is considered the best topology for airfoils with blunt trailing edges in order to save as many cells as possible and to avoid high aspect ratios. In figure 3.1 it is shown a zoom of the O-mesh used and in figure 3.2 a mesh for the same airfoil using a C-mesh. It can be seen in figure 3.2 that the wake of a C-mesh for the same airfoil requires more cells than the same mesh done with an O-mesh topology.

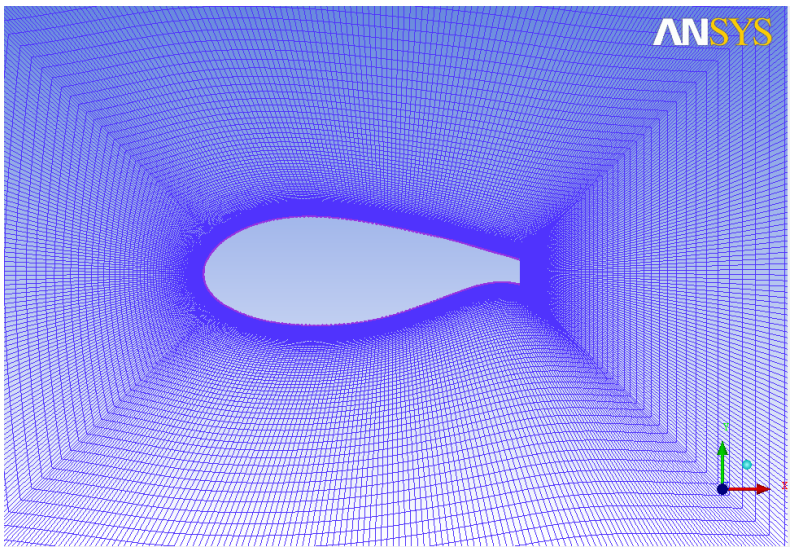

Figure 3.1: Zoom of the airfoil FB-3500-0875 meshed using an O-mesh.

In figure 3.3 it is shown the distribution of the cells in the trailing edge while meshing a flatback airfoil using a C-mesh. The mesh shown would need even more cells in the wake since the ratio between the first cell of the edge normal to the airfoil and the first cell in the wake is high, i.e. higher than 1.2. Thus, in order to not waste cells, the O-mesh is going to be used for both the

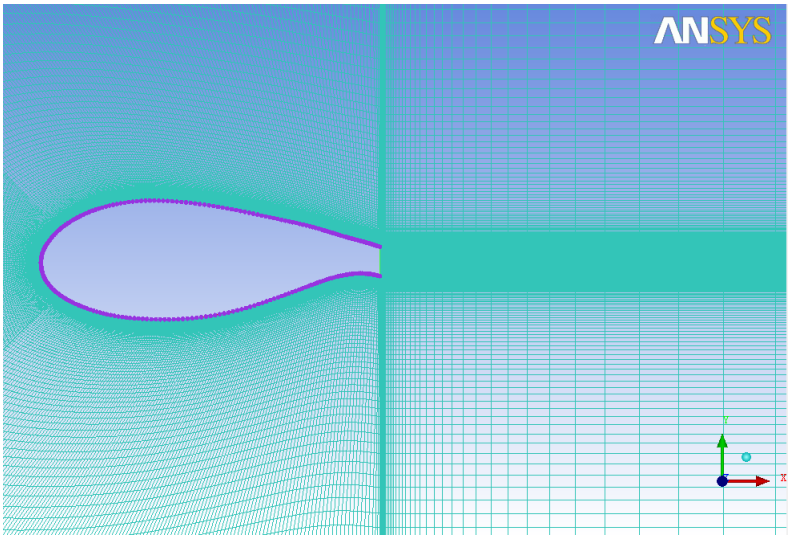

Figure 3.2: Zoom of the airfoil FB-3500-0875 meshed using a C-mesh. Example of a mesh not optimal for flatback airfoils.

flatback and the blunt airfoils studied.

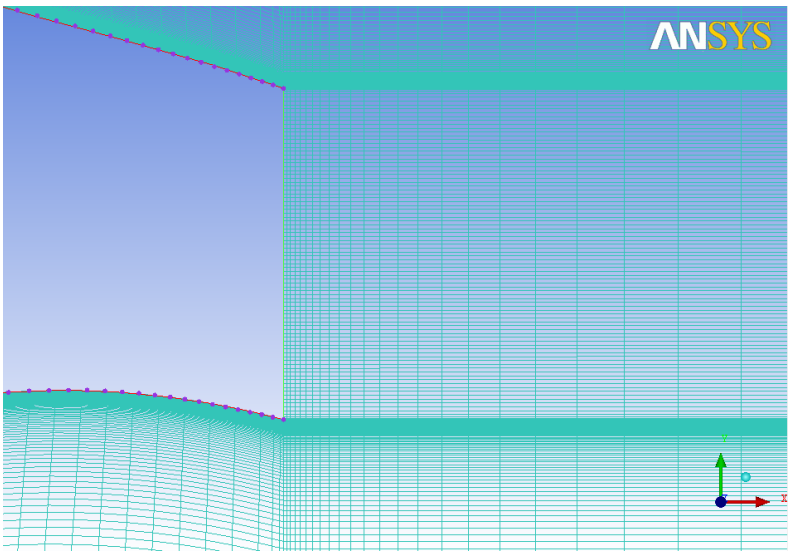

Figure 3.3: Zoom at the trailing edge of the Airfoil FB-3500-0875 meshed using a C-mesh. Example of a mesh not optimal for flatback airfoils.

The expansion ratios used are below 1.2 in all the edges used in order to mesh the domain solved. In the direction normal to the wall this ratio has to be between 1.05 and 1.1 while using the model to predict the transition between the laminar and the turbulent boundary layer as it is stated in the

best practices for this model used, already mentioned in 2.5. Thus, it is fixed to a value of 1.06 in this edge.

It is decided to use a downstream and an upstream distance of 60 chord lengths, it will be shown further in chapter 4 a sensitivity study of the size of the domain.

Once the meshes are created with ANSYS ICEM HEXA and converted to Fluent format, they are imported to OpenFOAM using the tool of this software *fluent3DMeshToFoam*.

OpenFOAM has a tool called *checkMesh* that checks for mesh issues such as the aspect ratios, the non-orthogonality and the skewness. This tool is run every time one mesh is generated. The software complains for aspect ratios (AR) higher than 1.000. Thus, all the meshes used have AR lower than this value. This does not mean though that it can not run meshes with aspect ratios higher than 1.000, it has been tested and depending on the value got (between 1.000 and 3.000), complaints from *checkMesh* are obtained but the results are run giving good results (in terms of convergence of the solution and its quality after comparing it with experimental results or other CFD codes). However, while using meshes with much higher aspect ratios the solution starts to diverge, there is one example about this given in appendix A, where it is explained how a NACA0012 is meshed using a C-mesh topology with high aspect ratios.

Chapter 4

NACA0012 - Sensitivity Studies

4.1 NACA0012 vs NACA0012 blunt

At the beginning of the thesis and taking into account that it was the first time that I was going to use OpenFOAM to study flow around an airfoil, it was decided to study the airfoil NACA0012 at Re=3.000.000. The different sensitivity studies are done for the airfoil NACA0012 with a blunt trailing edge (where 4,3 % of the chord is cut off), thus a mesh with an O-mesh topology is used, the same as the one used for the flatback airfoils. This will generate an airfoil with different geometrical characteristics, shown in figure 4.1 and table 4.1. The results got for the aerodynamic coefficients will be different than the ones obtained for the airfoil NACA0012 with the sharp trailing edge, this difference is shown in figures 4.16a and 4.16b, where the k-ω SST turbulence model is used.

The sharp airfoil requires a C-mesh topology in order to mesh it, in appendix A there is an explanation of the procedure done in order to create it and a comparison between results with OpenFOAM and ANSYS CFX for this NACA0012 with a sharp trailing edge.

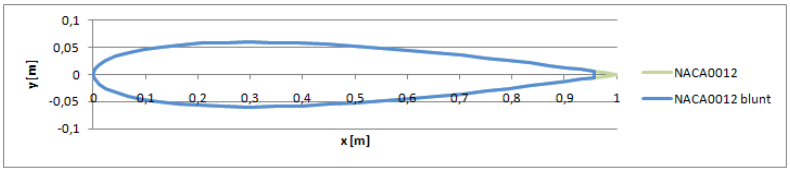

Figure 4.1: Geometry of the NACA0012 airfoil and the NACA0012 airfoil with the blunt trailing edge.

The results for the airfoil NACA0012 have been compared to experimental results from [11], these are shown in the different figures and are called "TWS".

	Max. thickness	at x/c	Max. camber	at x/c
NACA0012	12 %	30,1 %	0 %	-
NACA0012 blunt	12,47 %	31,04 %	0 %	-

Table 4.1: Characteristics of the airfoils shown in 4.1 relative to the chord.

Since these results only go up to an angle of attack of 12 degrees for the drag coefficient and 18 degrees for the lift coefficient there is also included experimel data from reference [10]. The results obtained were also compared with CFD results computed with the programme ANSYS CFX version 13.0 using exactly the same meshes.

As it can be seen, the airfoil NACA0012 with the blunt trailing edge is not stalled at an angle of attack of 18 degrees as it happens for the case of the NACA0012 with the sharp trailing edge. In figure 4.16b it is seen that the drag coefficient is higher for the NACA0012 with the blunt trailing edge.

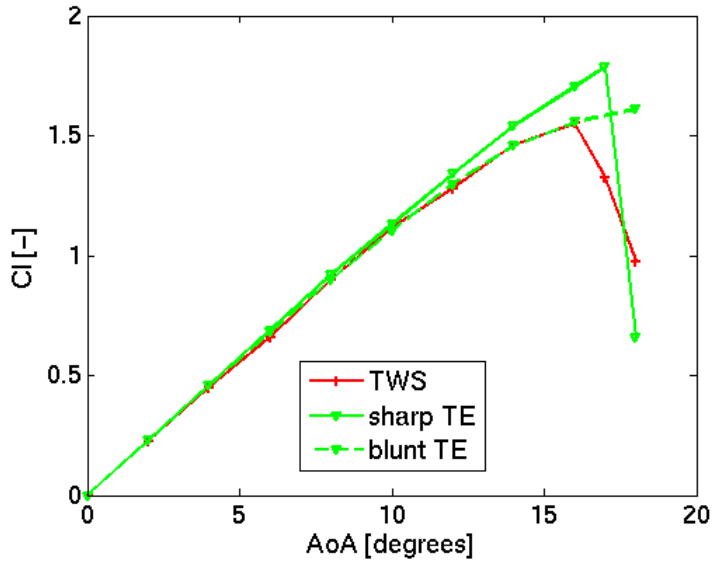

(a) Lift coefficient.

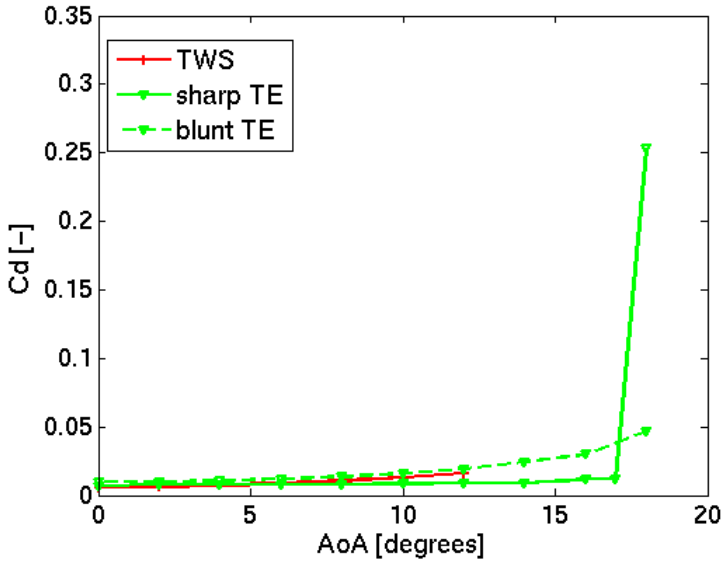

(b) Drag coefficient.

Figure 4.2: Aerodynamic coefficient curves for the airfoil NACA0012 original and truncated, for Re=3.000.000. Curves obtained with OpenFOAM.

The different sensitivity studies performed in this section have been done, unless it is stated something different, using the $k-\omega$ SST turbulence model without transition model applied in the boundary layer, meshes with 130.000 cells, boundaries placed 60 chords away from the outlet and linear upwind numerical scheme for the convective terms.

4.2 Comparison of both $k-\omega$ SST and Spalart-Allmaras turbulence models

The $k-\omega$ SST turbulence model is supposed to work better than the Spalart-Allmaras turbulence model, mainly for the stall region, since it was designed for flows with adverse pressure gradients. It is compared the performance of this turbulence model in OpenFOAM with the results obtained with ANSYS CFX for computations with the same characteristics. The only difference found is in the numerical schemes, for OpenFOAM it was chosen a 2nd order scheme (linearUpwind), while for ANSYS CFX it was chosen one option available called "High Resolution", which is a bending between first and second order accuracy. Thus, the optimal scheme for both convergence and accuracy is chosen for these computations with ANSYS CFX. The results for this comparison are shown in figures 4.3 and 4.4. In this figure they are also shown results from computations done with XFOIL, which uses the method explained in XXX. It was tried to run higher angles of attack with XFOIL but the programme said that the solution did not converge.

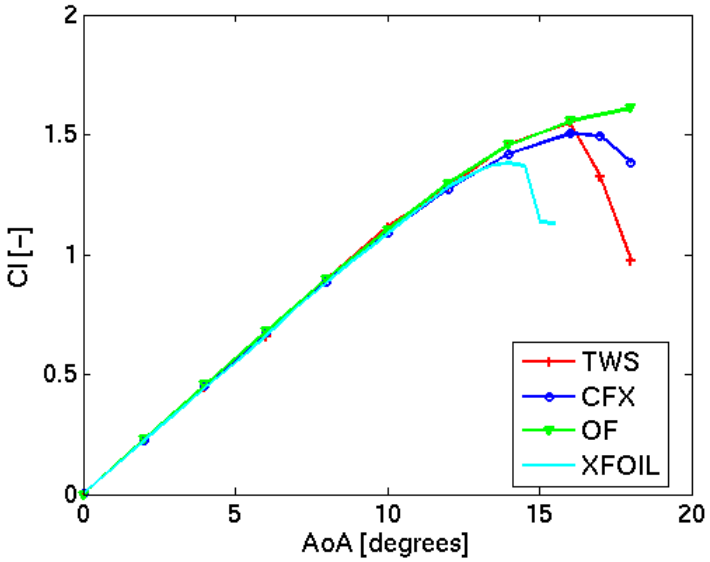

Figure 4.3: Lift coefficient curves for the airfoil NACA0012 with the blunt trailing edge using the $k-\omega$ SST turbulence model. Re=3.000.000

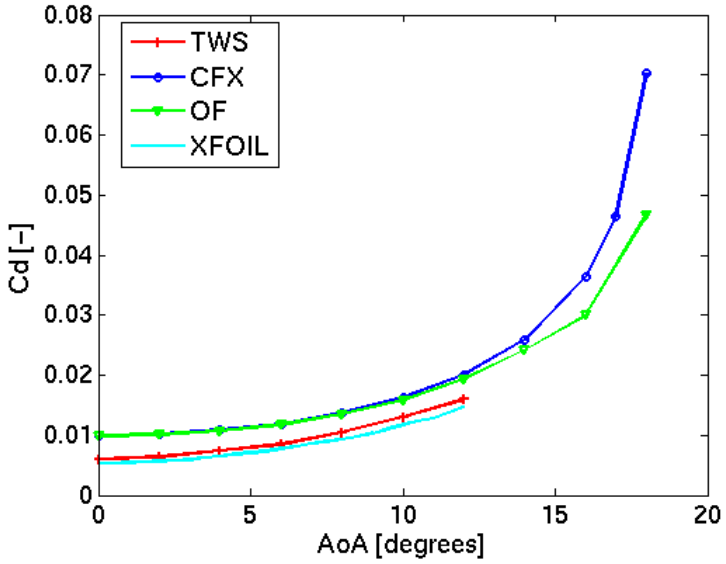

Figure 4.4: Drag coefficient curves for the airfoil NACA0012 with the blunt trailing edge using the $k-\omega$ SST turbulence model. Re=3.000.000.

In figure 4.3 it can be seen that ANSYS CFX captures better the stall region than OpenFOAM compared to the experimental results from reference [11]. On the other hand, in figure 4.4 it is shown that both programmes over predict the drag coefficient.

Convergence of the solutions

In figures 4.5 and 4.6 are shown the residuals for the computations performed with the different turbulence models for a certain angle of attack (8 degrees). As it can be seen the residuals for the momentum equations in both directions and the residuals for the pressure look very similar. The residuals for the equations of each the turbulence model $k-\omega$ SST are lower than the residuals for the equation $\tilde{\nu_t}$ of the turbulence model Spalart-Allmaras.

In order to check whether the solution has converged completely or not the history of the force coefficients during the simulation, (i.e. the graph of the force coefficients and the number of iteration) are also checked for every simulation. One example of these for both turbulence models used is shown in figures 4.7 and 4.8.

Force coefficients

To sum up, they are plotted the solutions obtained for both turbulence models, obviously the rest of settings of the computation is the same (mesh, boundary conditions and numerical schemes). This comparison can be seen on figures

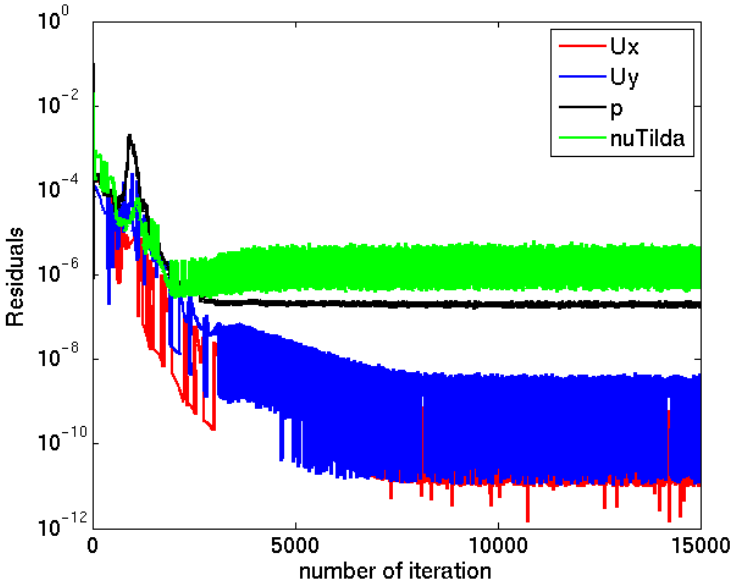

Figure 4.5: Residuals during the computation performed for the Spalart-Allmaras turbulence model and an angle of attack of 8 degrees. Simulation run for the airfoil NACA0012 with the blunt trailing edge at Re=3.000.000 using OpenFOAM.

4.9a and 4.9b. The turbulence model $k-\omega$ SST gives a better prediction of the flow behavior in the stall region. This is the reason why this turbulence model was considered the one to be used to study the thick flatback airfoils. However, as it will be shown in chapter 5 it is not possible to make computations for the thick airfoils without the transition model for the boundary layer. This is the reason why this transition model is tried also in the NACA0012 airfoil with the blunt trailing edge, this comparison is shown in the following section.

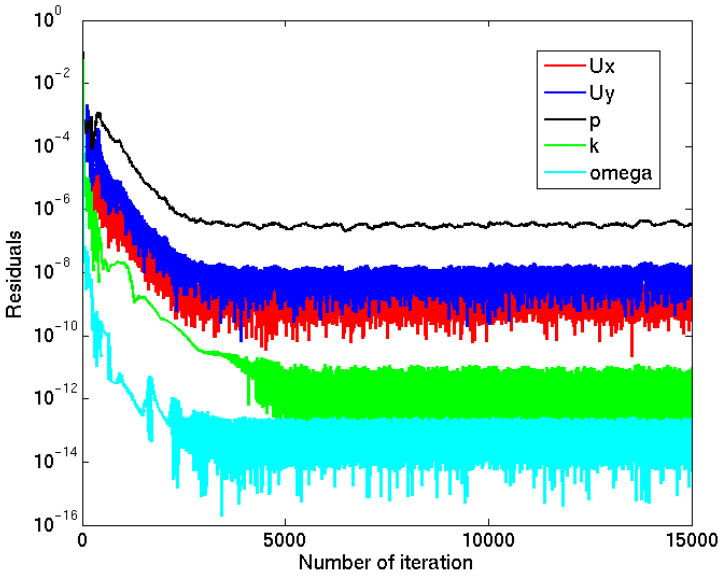

Figure 4.6: Residuals during the computation performed for the $k-\omega$ SST turbulence model and an angle of attack of 8 degrees. Simulation run for the airfoil NACA0012 with the blunt trailing edge at Re=3.000.000 using OpenFOAM.

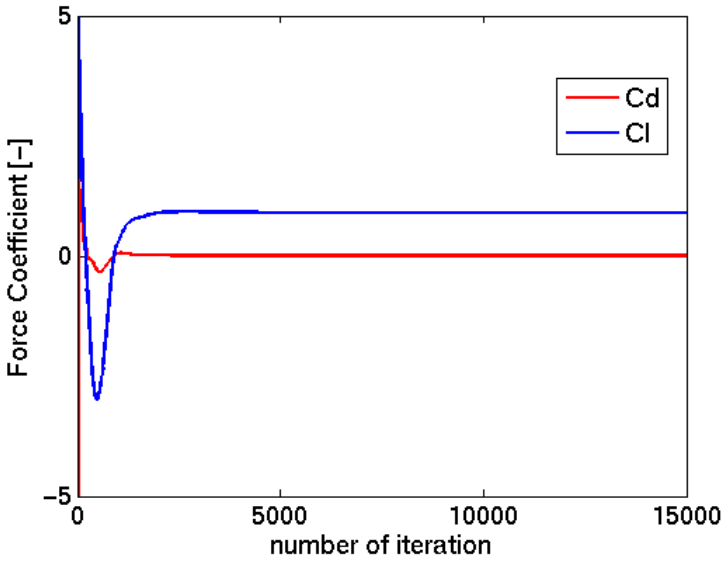

Figure 4.7: Force coefficients history for the Spalart-Allmaras turbulence model and an angle of attack of 8 degrees. Simulation run for the airfoil NACA0012 with the blunt trailing edge at Re=3.000.000.

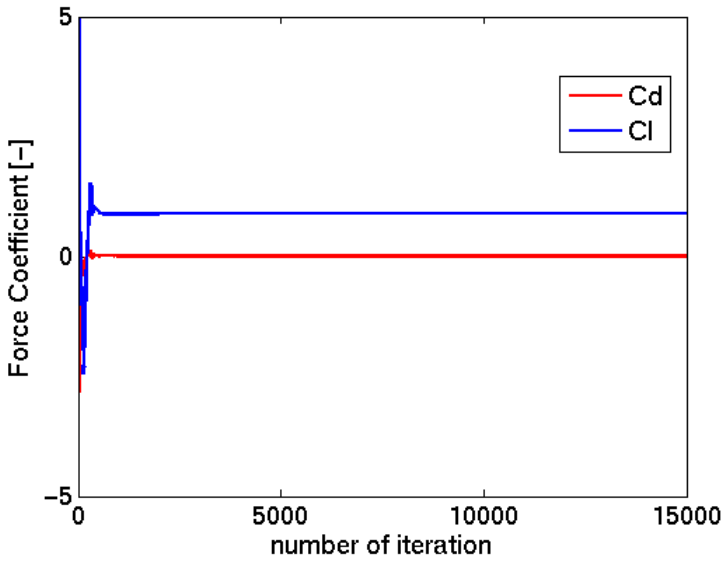

Figure 4.8: Force coefficients history for the $k-\omega$ SST turbulence model and an angle of attack of 8 degrees. Simulation run for the airfoil NACA0012 with the blunt trailing edge at Re=3.000.000.

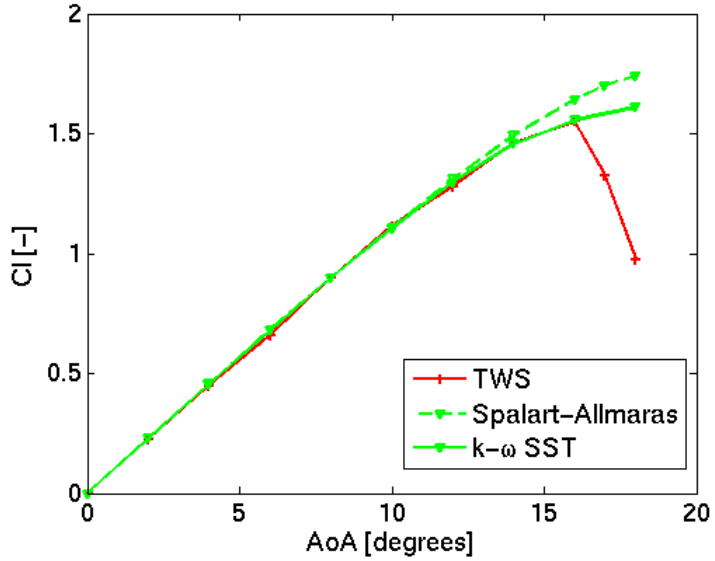

(a) Lift coefficient.

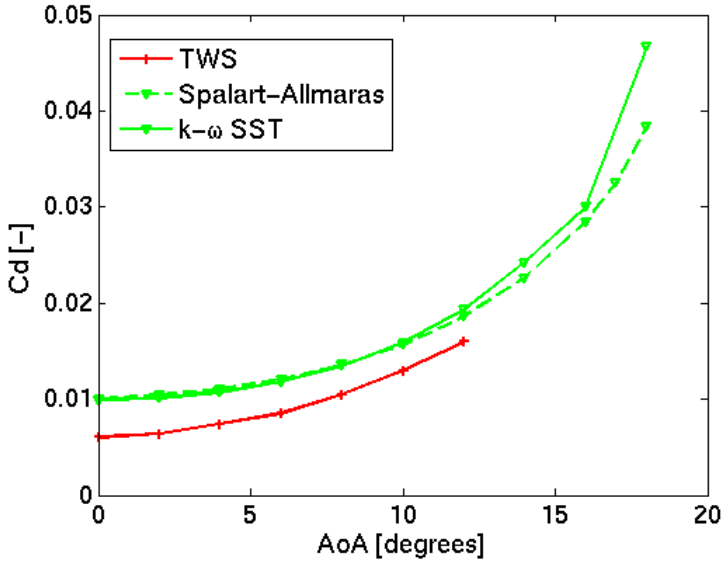

(b) Lift-drag curve.

Figure 4.9: Aerodynamic coefficient curves for the computations using both turbulence models using OpenFOAM. NACA0012 with blunt trailing edge at Re=3.000.000.

4.3 Introducing the transition prediction model

In this point the curves for the lift and drag coefficients are compared for the computations with the turbulence model $k-\omega$ SST and for computations with this model and the transition model introduced in 2.5 from laminar to turbulent boundary layer using OpenFOAM. As it can be seen in figures 4.10a and 4.10b, for the airfoil NACA0012 studied while introducing the transition model at the boudnary layer it is captured the stall at an angle of attack of 18 degrees while this is not happening while running the $k-\omega$ SST turbulence model without the transition model.

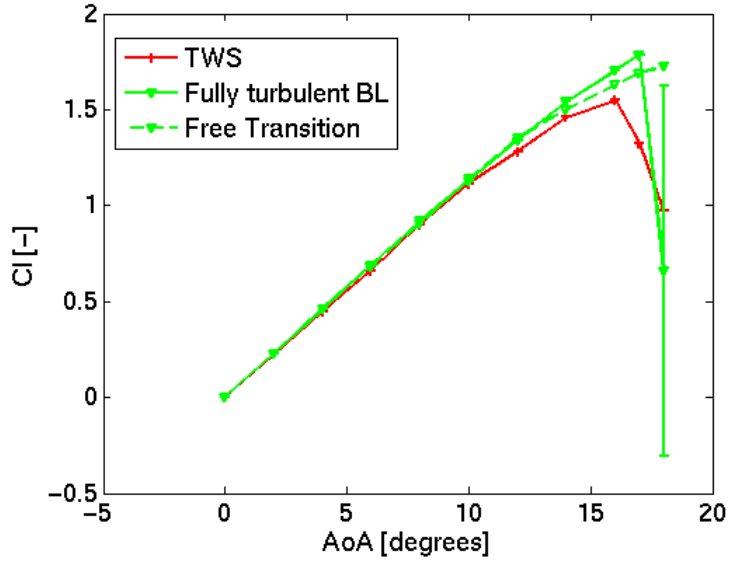

(a) Lift coefficient.

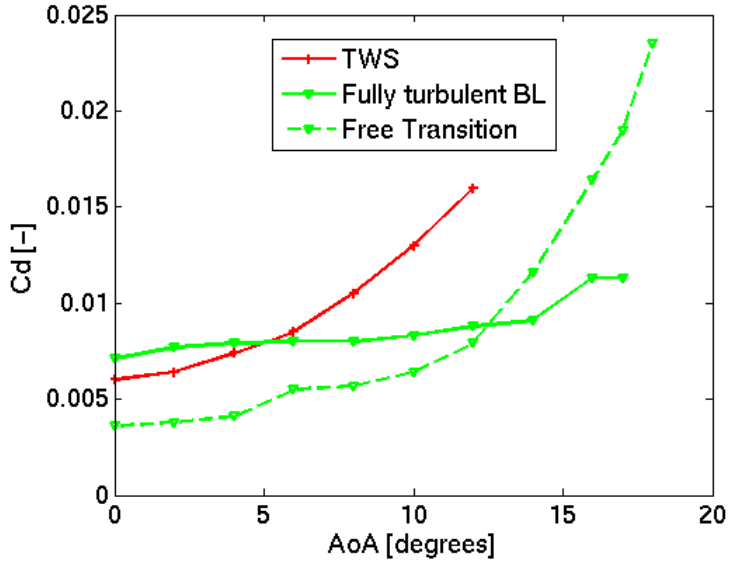

(b) Drag coefficient.

Figure 4.10: Aerodynamic coefficient curves for the computations with OpenFOAM with and without transition model for the boundary layer. NACA0012 at Re=3.000.000.

Cp and Cf curves validation

In this section it was used experimental data from reference [29] in order to compare a Cp curve obtained with OpenFOAM and ANSYS CFX for an incoming flow at an angle of attack of 10 degrees. The cases were run with free transition at the boundary layer.

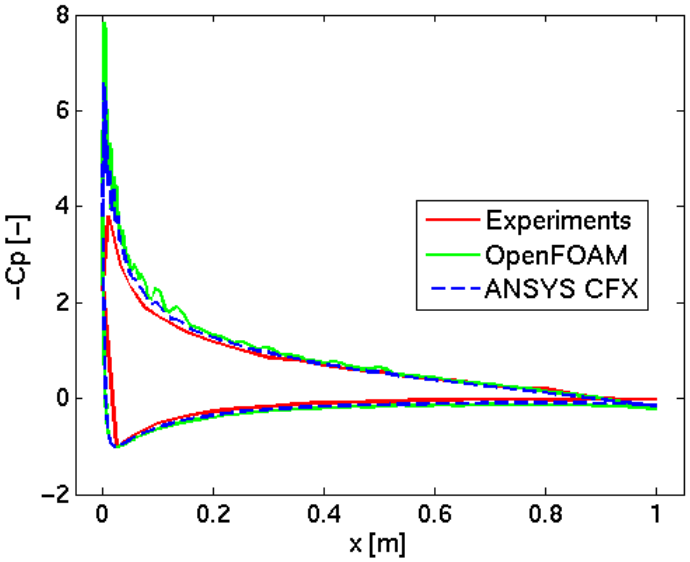

Figure 4.11: Curves of the pressure coefficient Cp for the NACA0012 at an angle of attack of 10 degrees and Re=3.000.000. Experimental data taken from [12].

It can be seen in figure 4.14 that the Cp curve for both CFD programmes is the same since they are computed with the same mesh. It is seen that the pressure difference is slightly higher for the computations than for the experiments.
The friction coefficient curve all over the airfoil, Cf, has not been validated with experimental results because these were not found. It was compared though for a Cf curved obtained with ANSYS CFX at both pressure and suction side of the airfoil, this is shown in figure 4.12. In figure 4.12a they are seen wiggles close to the trailing edge for both results obtained with ANSYS CFX and OpenFOAM, this yields a clear evidence that these are due to the meshing done.

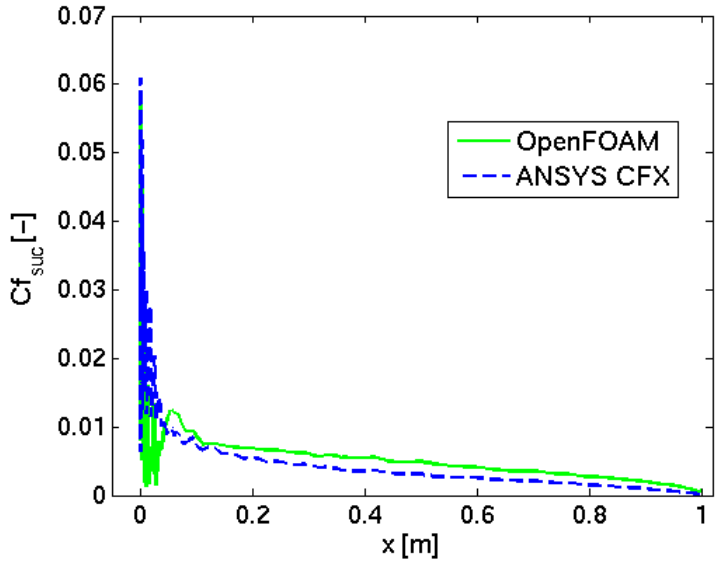

(a) Lift coefficient.

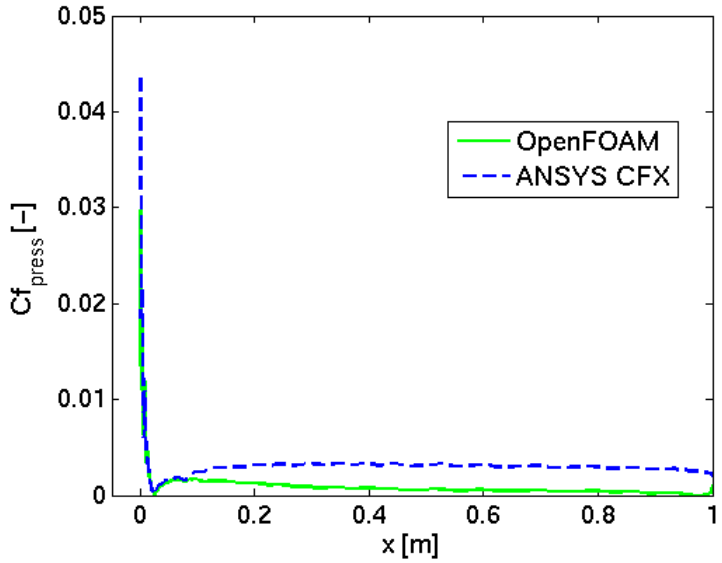

(b) Drag coefficient.

Figure 4.12: Friction coefficient curves for the airfoil NACA0012 at an angle of attack of 10 degrees and Re=3.000.000.

Prediction of the transition point

As it has been explained in section 2.5 the point where the transition region of the boundary layer from laminar to turbulent starts is called transition point. In figures 4.13 and 4.14 they are shown both C_f and C_p curves, respectively, for a NACA0012 at Re=3.000.000 and an angle of attack of 2 degrees. In figure 4.13 the location of the transition point at both suction and pressure side can be seen in the friction coefficient curve. The curve representing the C_f for the case run with transition model applied presents a sudden variation of C_f at the transition point, based on reference [25]. The drag coefficient is higher for the case run without transition model at the boundary layer as it is shown in figure 4.10b because the friction coefficient is higher for this case. On the other hand, in figure 4.14, showing the pressure coefficient C_p for both cases run with fully turbulent boundary layer and free transition at the boundary layer, it is seen that both C_p curves are slightly different. Thus, it is shown why the lift coefficients at an angle of attack of 2 degrees are very similar in figure 4.10a (the difference can not really be appreciated).

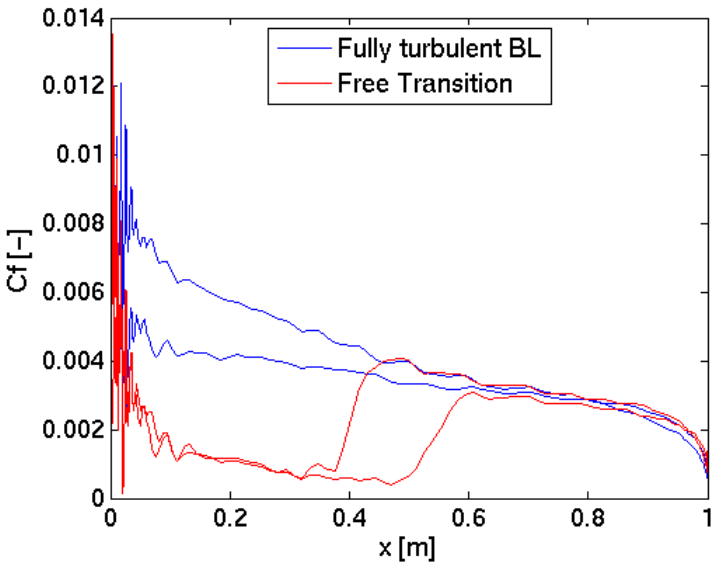

Figure 4.13: C_f curves at both pressure and suction side for the different cases specified for a NACA0012 at an angle of attack of 2 degrees at Re=3.000.000.

In figure 4.15 it is shown the position predicted for the transition point at the suction and pressure side of the airfoil predicted with both OpenFOAM, ANSYS CFX and XFOIL compared to experiments (obtained from [30] and [31]). In figure 4.15 it can be seen that OpenFOAM and XOIL are giving very similar results for the position of the transition point compared to experiments

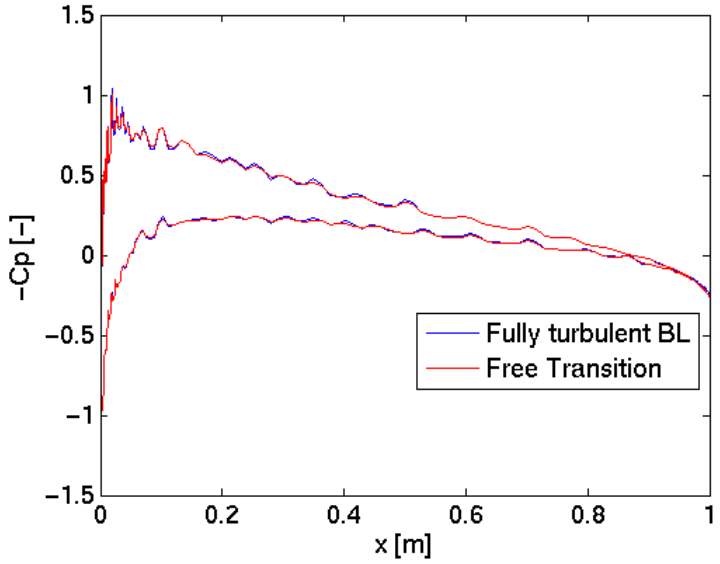

Figure 4.14: C_p curves for the different cases specified for a NACA0012 at an angle of attack of 2 degrees at Re=3.000.000.

in the suction side, while ANSYS CFX results are not that similar. On the other hand, in the pressure side, none of them is giving a similar result to the experimental results, OpenFOAM's results are better compared to these than the ones obtained with ANSYS CFX are. As it has been explained in 2.5 one of the differences between ANSYS CFX and the computations obtained with OpenFOAM are the correlation factors used while defining the transition model, but this is not thought to give a lot of differences in the behavior of the flow.

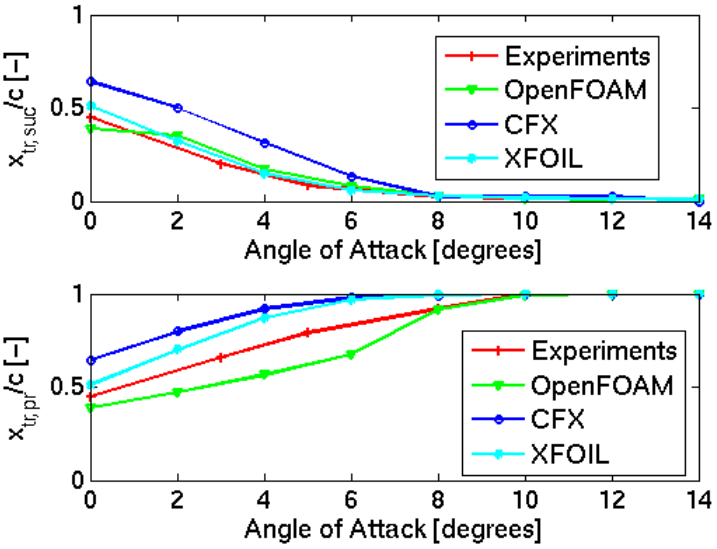

Figure 4.15: Position predicted for the transition point on the airfoil NACA0012 at Re=3.000.000.

4.4 y^+ dependence study

In this part it is studied the dependence of the solution for different values of y^+, which has been previously defined in section 2.6. Thus, in order to get the different points of figure 4.16 they are done simulations using exactly the same characteristics, the only thing that was changed was the height of the cells closest to the wall. The mesh with the lowest value of maximum y^+ has a cell height closest to the airfoil of $1e^{-6}$ m, while the one with the highest value of maximum y^+ is $1e^{-4}$ m. This sensitivity study is done for both the sharp and the blunt NACA0012.

It is used the maximum value of y^+ found all over the airfoil in order to do the study. The results for this study are shown in figures 4.16. Although the results do not show perfectly an asymptotic behavior while decreasing the value of $max(y^+)$ shown, the small difference seen between the points with lowest $max(y^+)$ is about 0,4 %. The curve for the NACA0012 blunt shown in 4.16b does not show an asymptotic behavior while decreasing the value of $max(y^+)$ as it was expected beforehand, it is thought though that this is because the drag obtained due to the bluntness of this airfoil. However, the difference observed between the point at lowest $max(y^+)$ and the point at $max(y^+) = 2$ is 5 %.

Thus for all the computations done from now on it is checked that the value of the maximum y^+ over the airfoil is less than 2 according to reference [17].

4.5 Domain extent

A sensitivity study of the domain extent used in order to do the computations is done. In order to do it the computations had exactly the same characteristics but the only aspect that has been changed is the distance from the airfoil to the boundaries. It was thought that the study could be more accurate if the region close to the airfoil was not modified, thus the solution of the boundary layer would not be affected by increasing the mentioned distance. Thus, it was done a split in the edge normal to the wall as it is shown in figure 4.17. In the edges normal to the wall "A" there was no modification done for the different computations while for the edges "B" they were increased both the distance and the number of cells (in order to maintain constant the width of the cell closest to the boundaries).

The results obtained for this study are shown in figures 4.18a and 4.18b for angles of attack of 2 and 10 degrees respectively. It can be seen the asymptotic behavior for both force coefficients curves, both of them tend to the value closest to reality, i.e. ∞ distance.

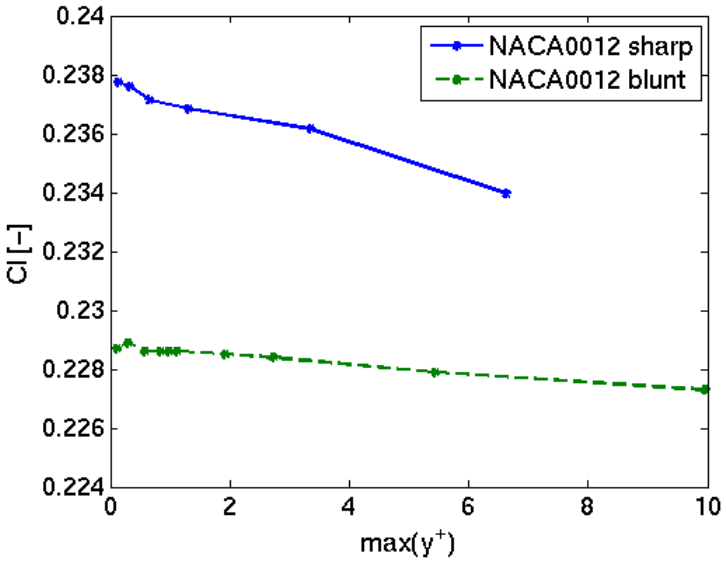

(a) Lift coefficient.

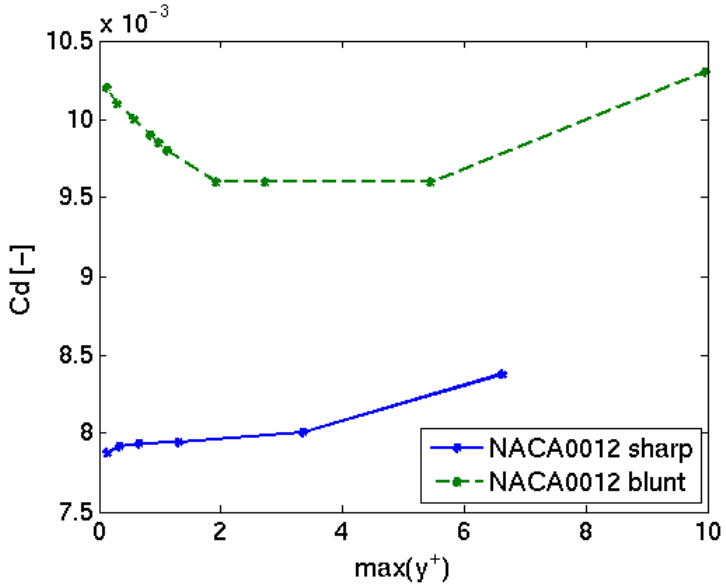

(b) Drag coefficient.

Figure 4.16: y^+ sensitivity study on the NACA0012 airfoil with the trailing edge blunt at Re=3.000.000.

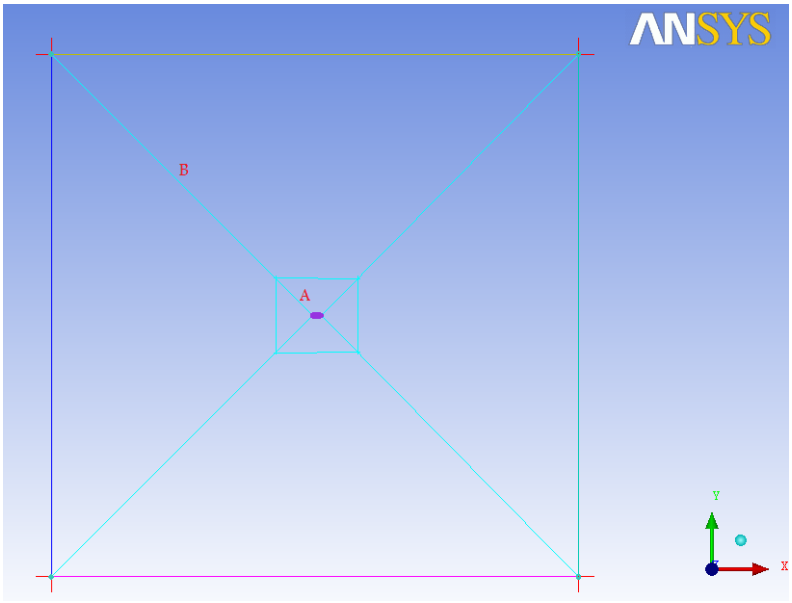

Figure 4.17: Topology view of the meshes done in order to do the domain extent sensitivity study.

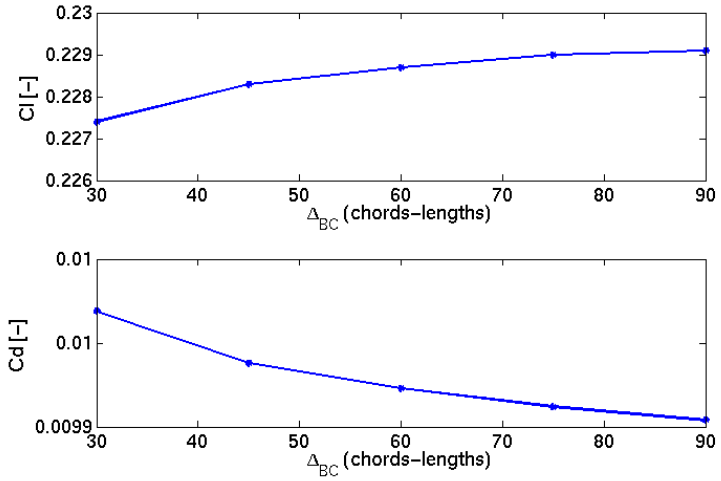

(a) Angle of attack = 2 degrees.

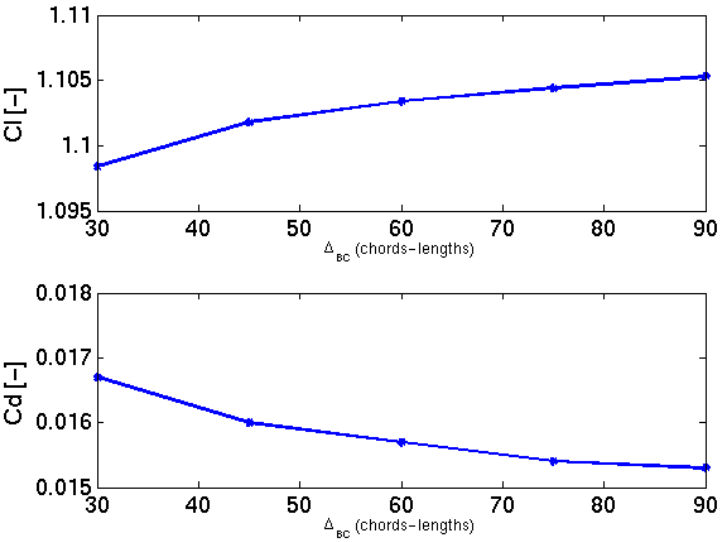

(b) Angle of attack = 10 degrees.

Figure 4.18: Sensitivity study of the domain extent. Simulations for the airfoil NACA0012 with the blunt trailing edge at Re=3.000.000.

4.6 Cell count dependence study

Choosing a mesh with the optimal number of cells in order to do a CFD simulation is very important. This optimal is based on both accuracy of the results and speed of the solution to converge. The meshes used for the different simulations performed have between 130.000 and 155.000 cells, then some refinement is done in order to check how the number of cells affects the accuracy of the solution.

For the NACA0012 airfoil with the blunt trailing edge these different refinements are done so that the only thing that changes is the number of cells in the x-y plane, where the airfoil is allocated.

In figure 4.19 it is shown the mesh dependence study for an angle of attack of 2 degrees. It is seen that the results look as expected, i.e. asymptotic behavior while increasing the number of cells. It is shown that decreasing the amount of cells to half of the number of cells used, yields higher differences than the ones obtained while making the different refinements. This is due to the coarsest mesh has not enough cells to solve the flow properly.

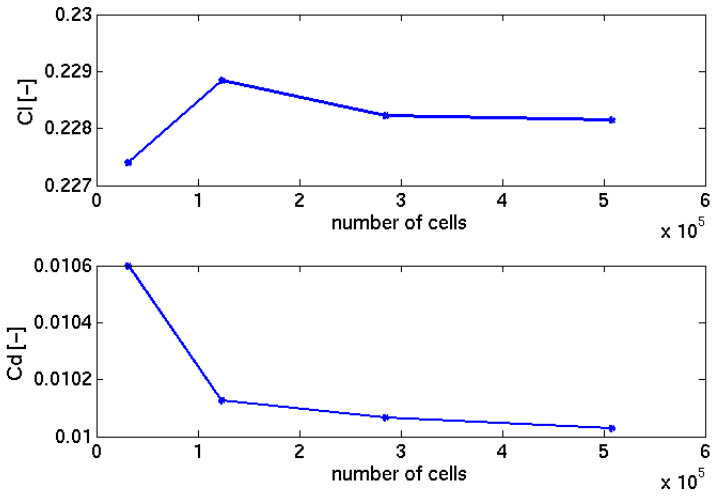

Figure 4.19: Mesh dependence study for the NACA0012 with the blunt trailing edge for an angle of attack of 2 degrees at Re=3.000.000.

They are also done mesh dependence studies for the same airfoil for angles of attack of 8 degrees and 14 degrees, these are shown in figures 4.20 and 4.21, respectively. It can be seen that the asymptotic behavior is not present in all the curves shown but the differences between the points obtained with less cells and the ones with the finest meshes is about 1 %. Thus, the results of this mesh dependence study are considered to be correct.

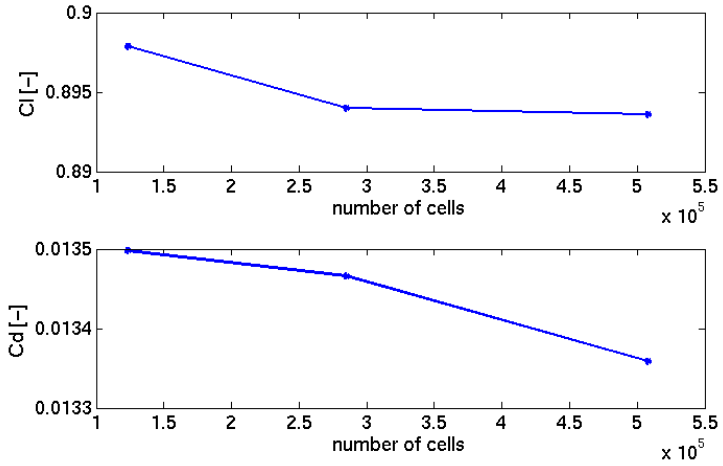

Figure 4.20: Mesh dependence study for the NACA0012 with the blunt trailing edge for an angle of attack of 8 degrees at Re=3.000.000.

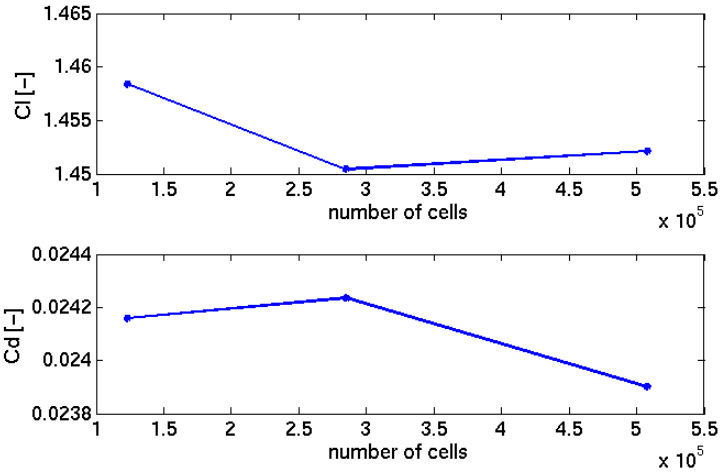

Figure 4.21: Mesh dependence study for the NACA0012 with the blunt trailing edge for an angle of attack of 14 degrees at Re=3.000.000.

4.7 Numerical schemes dependence

The sensitivity to different numerical schemes used in order to solve the convective terms of the Navier-Stokes equation, equation 2.13, is checked for the NACA0012 airfoil with the blunt trailing edge. The sensitivity study is only performed for the points of the polar curve that are approaching the stall region (i.e. angles of attack of 12, 14 and 16 degrees).
The numerical schemes checked are QUICK and linear upwind. The upwind differencing scheme is not checked since it presents first order accuracy and the central differencing scheme is not checked either due to the issues they can appear due to the transportiveness and boundedness issues that may appear. The results of this sensitivity study are shown in figures 4.22a and 4.22b. Since the experimental data used up to this point (from [11]) for the comparisons had results for the drag coefficient up to an angle of attack of 12 degrees it is added experimental data from [10], which is for a different Reynolds number, as it is specified in 4.7.

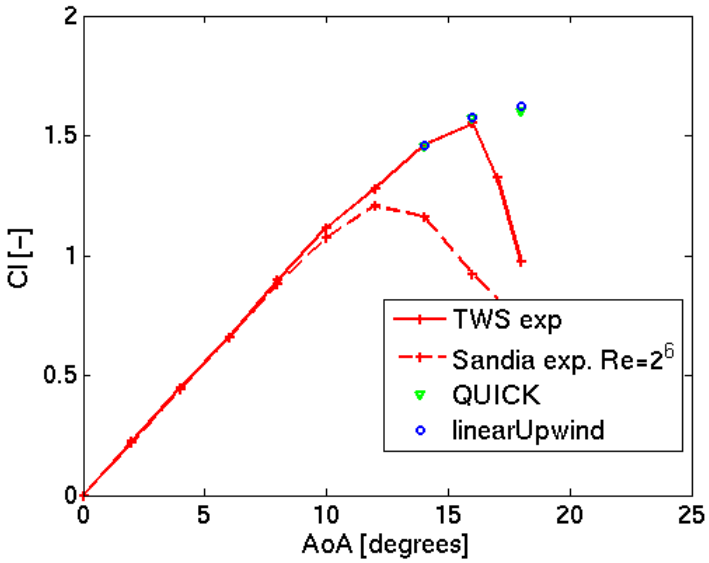

(a) Lift coefficient.

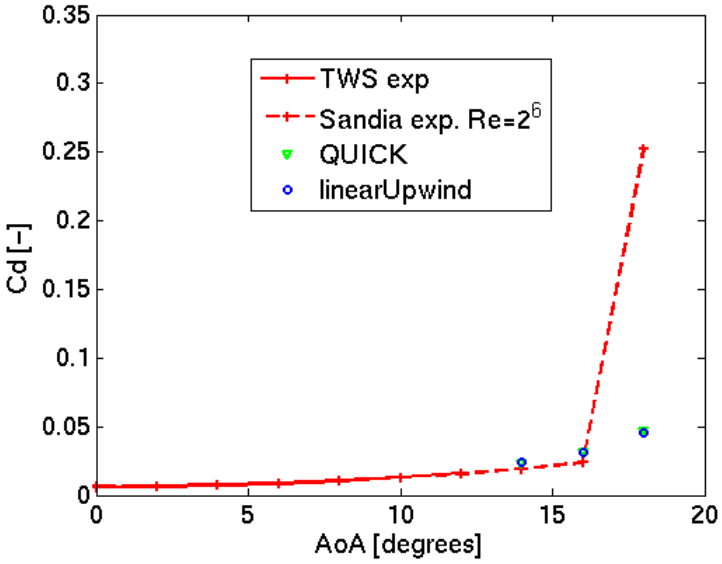

(b) Drag coefficient.

Figure 4.22: Aerodynamic coefficients obtained for different differencing schemes in the convective terms of the RANS equation. Tested at the airfoil NACA0012 with the blunt trailing edge at Re=3.000.000.

Chapter 5

Thick-blunt airfoils validation

In the previous chapter they were done some studies for the NACA0012 airfoil in order to validate the programme OpenFOAM. In order to get to the goal of this thesis, the flatback airfoils, thick blunt airfoils are studied to see the accuracy of the results given by the programme for these. The airfoils chosen in order to do this study are FX-77-W-343, FX-77-W-400 and FX-77-W-500, these were studied by Stuttgart University by wind tunnel experiments, the results can be found in [26]. Risø DTU has also been studying these airfoils with their in-house CFD code EllipSys (results shown in [27]), these results have also been introduced in the comparison. As it was done before for the NACA0012 in order to continue comparing the programme OpenFOAM with ANSYS CFX, results from the latter software obtained with the same meshes are also included.
The computations run for these airfoils (and for the airfoils shown in the following chapters) use meshes with 140.000-155.000 cells, the distance from the airfoil to the boundaries is 60 chord lengths, turbulence intensity at the inlet of 0.07 % and eddy viscosity ratio of 10. This low value of the turbulence intensity at the inlet is the same as the computations shown in [27]. They are done mesh dependence studies for some angles of attack of one airfoil of these group of airfoils. These are shown in G.
The geometry of the studied airfoils is shown in figure 5.1 and table 5.1. The airfoils FX-77-W-343, FX-77-W-400 and FX-77-W-500 have trailing edge thicknesses of 4,22 %, 11,1 % and 26,77 % relative to the chord, respectively.

	Max. thickness	at x/c	Max. camber	at x/c
FX-77-W-343	34,3 %	32,8 %	4,5 %	26,8 %
FX-77-W-400	40,1 %	37 %	5 %	29,4 %
FX-77-W-500	50,05 %	46,95 %	5,9 %	34,3 %

Table 5.1: Characteristics of the airfoils shown in 5.1 relative to the chord.

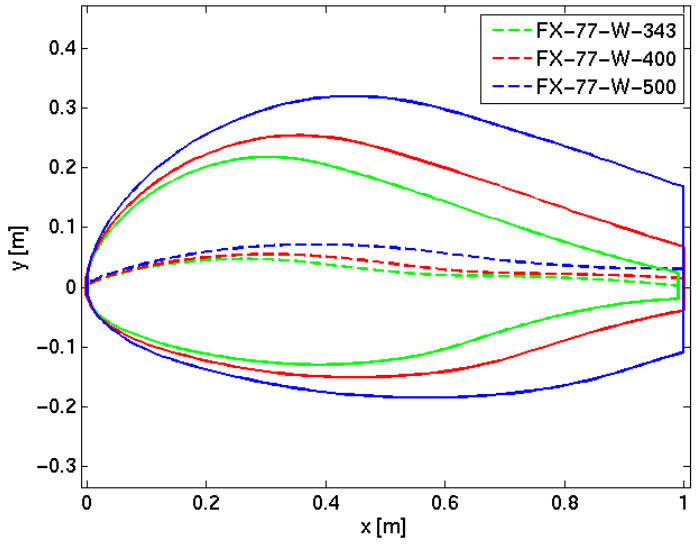

Figure 5.1: Comparison of the geometry of the airfoil FX-77-W studied.

5.1 Fully Turbulent vs Free Transition

In Stuttgart University, they did tests for fixed transition at the boundary layer between laminar and turbulent regime by fixing it at a certain point in both sides of the airfoil and also for free transition. This last one is the one that is checked in OpenFOAM. At the beginning, these airfoils were run without any transition model for the boundary layer, i.e. for a fully turbulent boundary layer with the $k-\omega$ SST turbulence model. A comparison for the airfoil FX-77-W-343 between the results obtained for this turbulence model with and without transition model is done in figures 5.2a and 5.2b.

As it can be seen in figures 5.2a and 5.2b the results obtained for fully turbulent boundary layer are much worse than the results with the transition model applied compared to the experimental results. These curves where also calculated with ANSYS CFX and the conclusion was the same because of the results obtained, this is shown in figures 5.3a and 5.3b. Thus, for the thick airfoils studied from now on it is decided not to use the $k-\omega$ SST turbulence model without the transition model for the boundary layer.

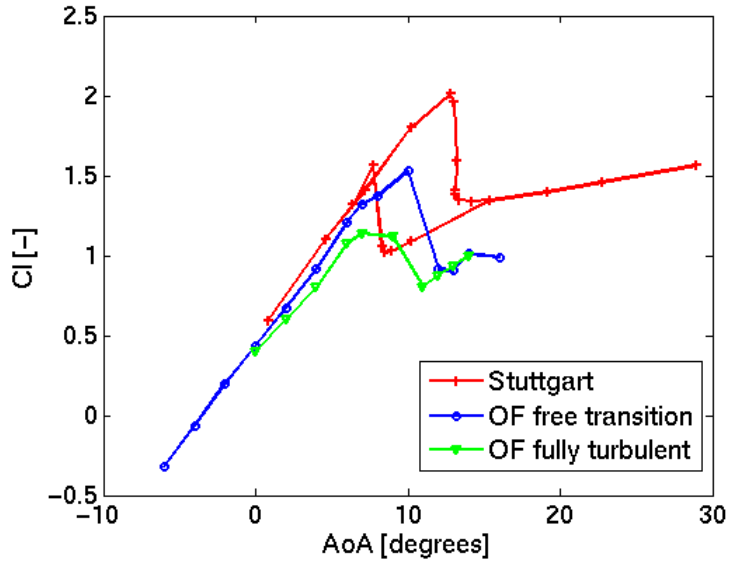

(a) Lift coefficient.

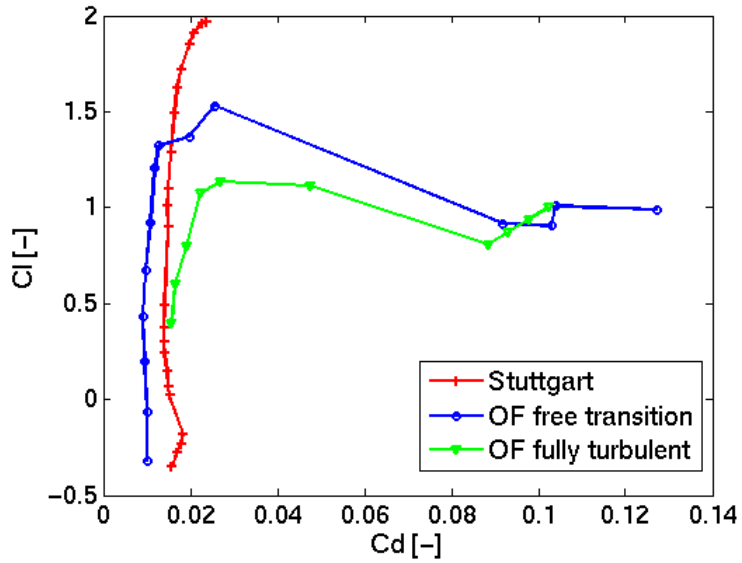

(b) Drag coefficient.

Figure 5.2: Aerodynamic coefficients for the airfoil FX-77-W-343 with and without transition model applied at Re=3.000.000.

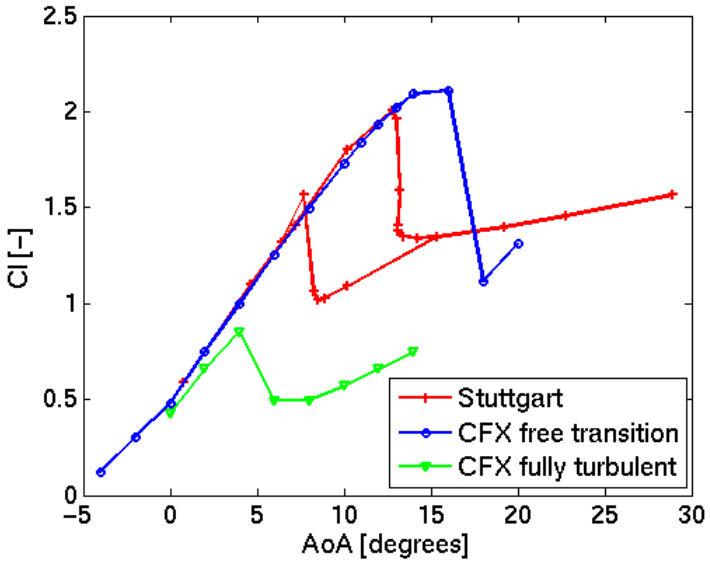

(a) Lift coefficient.

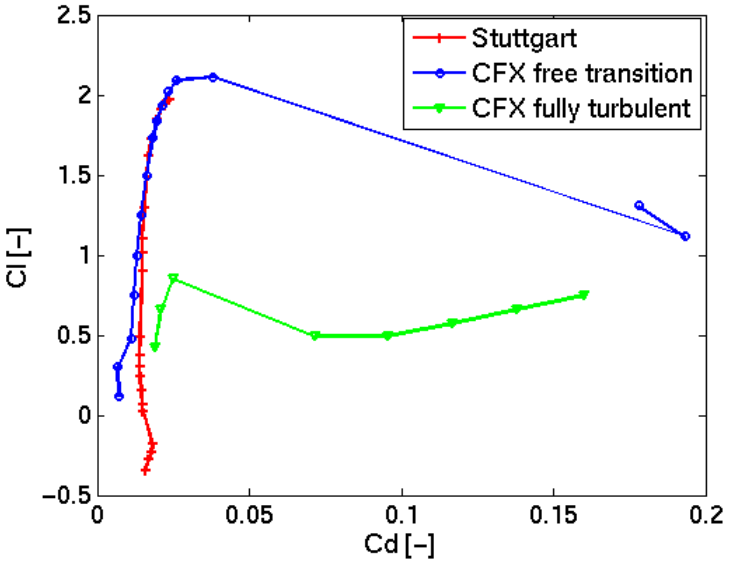

(b) Drag coefficient.

Figure 5.3: Aerodynamic coefficients for the airfoil FX-77-W-343 with and without transition model applied at Re=3.000.000. Results obtained with ANSYS CFX

5.2 Comparison of different CFD codes for the airfoil FX-77-W-343

The solution given by three different CFD codes and by the panel method (XFOIL) for the airfoil FX-77-W-343 have been compared. The results of this comparison is given in figures 5.4a and 5.4b. It is seen good agreement between the solutions given by both OpenFOAM and Ellipsys, both of them give the maximum lift coefficient for an angle of attack of 12 degrees, the highest difference found is for an angle of attack of 13 degrees because OpenFOAM shows that the airfoil is deep into stall while Ellipsys shows that it is getting to stall. On the other hand ANSYS CFX gives the highest lift coefficient for an angle of attack of 16 degrees and it is deep into stall for an angle of attack of 18 degrees. They are only shown the standard deviations that are not negligible. XFOIL, as it was supposed over predicts the lift coefficient. As it can be seen, from all the results shown in figure 5.4a ANSYS CFX is the programme which is approaching more to the experimental results.

In figures 5.5a and 5.5b they are compared the contour plots for the velocity field obtained for an angle of attack of 14 degrees with both OpenFOAM and ANSYS CFX, the first shows that the airfoil is deep in to stall while the other shows the airfoil approaching the point of Cl_{max}. It can be seen that the flow calculated by OpenFOAM is fully separated while the one calculated by ANSYS CFX is not.

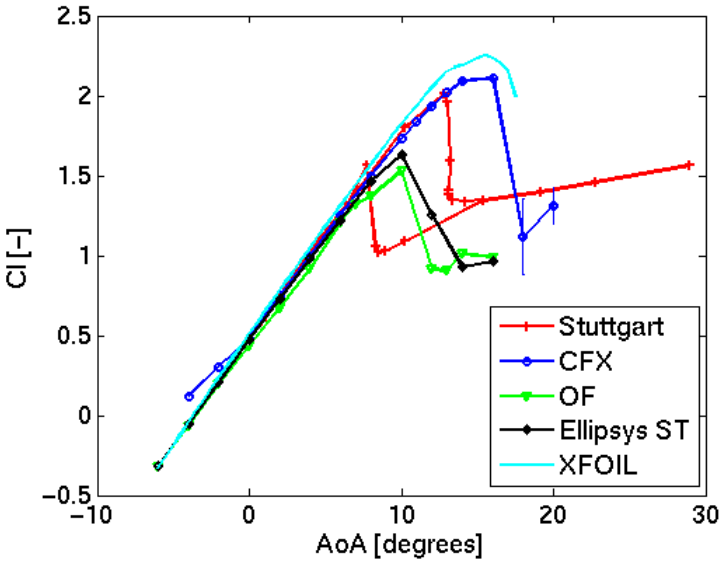

(a) Lift coefficient.

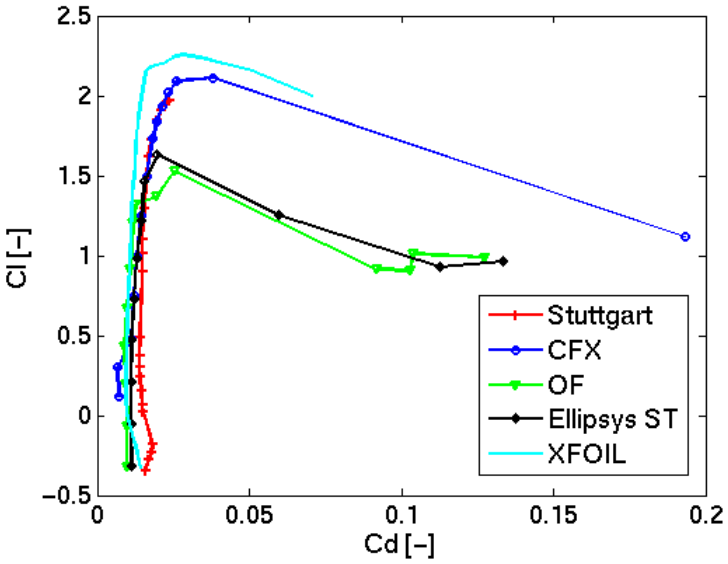

(b) Drag coefficient.

Figure 5.4: Aerodynamic coefficients for the airfoil FX-77-W-343 at Re=3.000.000.

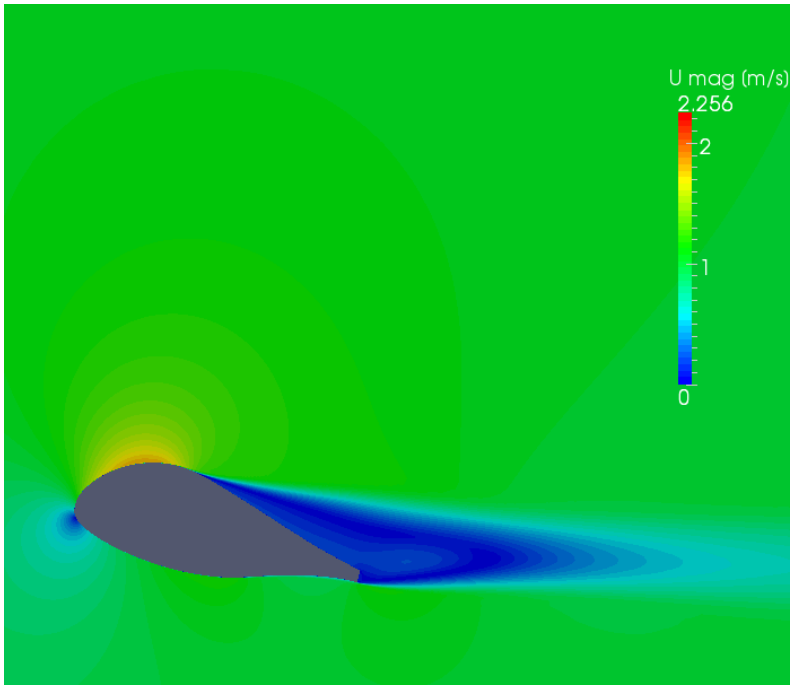

(a) Obtained with OpenFOAM.

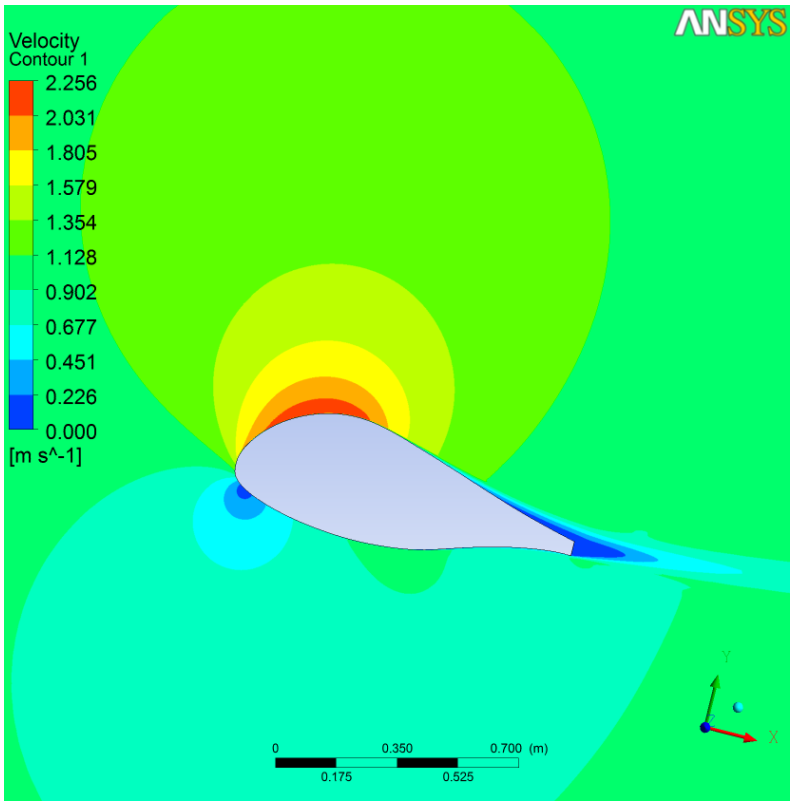

(b) Obtained with ANSYS CFX.

Figure 5.5: Contour plot of the velocity field for the airfoil FX-77-W-343 at Re=3.000.000 and an angle of attack of 14 degrees.

Numerical schemes dependence study for the airfoil FX-77-W-343

The only difference between the computations done with ANSYS CFX and the ones done with OpenFOAM are the numerical schemes used since the former one uses linear upwind differencing schemes while OpenFOAM are computed using QUICK differencing schemes for the convective terms. Ellipsys is using QUICK differencing schemes too for the these terms. This is the reason why the sensitivity study shown for the numerical schemes used in the convective terms is done in the points of the curve where results of OpenFOAM and ANSYS CFX differ the most, this is shown in figures 5.6a and 5.6b. The difference of the numerical schemes used by both programmes is not the reason of the difference of the solution.

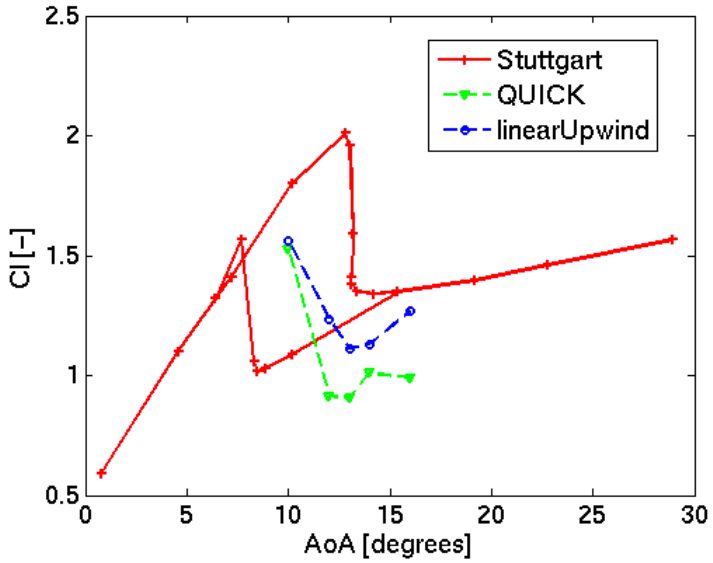

(a) Lift coefficient.

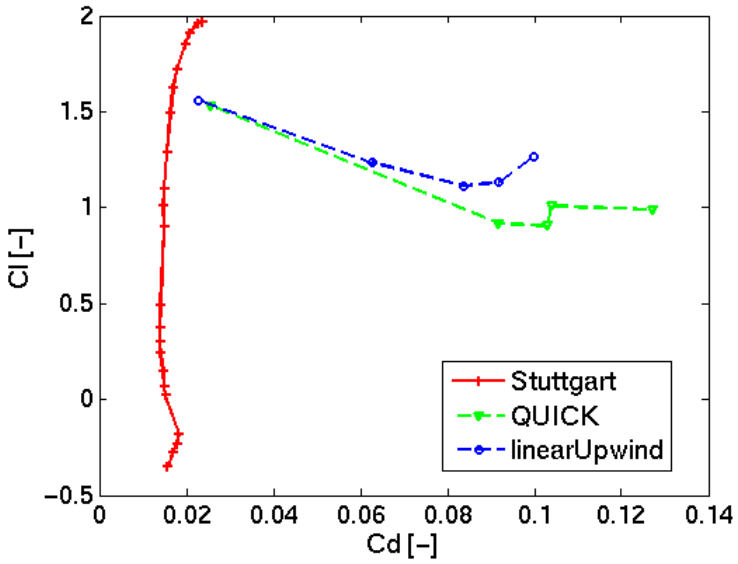

(b) Drag coefficient.

Figure 5.6: Numerical schemes dependence study for the airfoil FX-77-W-343 at the stall region at Re=3.000.000.

5.3 Comparison of different CFD codes for the airfoil FX-77-W-400

The comparison for the airfoil FX-77-W-400 is shown in figures 5.7a and 5.7b. For this airfoil OpenFOAM does not give results that similar to Ellipsys opposed to what it happened for the computations of the airfoil FX-77-W-343. It can be seen that compared to the experimental data from [26], OpenFOAM's results are closer than the results from ANSYS CFX for the lift coefficient. For this airfoil, the programme that is predicting the stall the best compared to the experimental data is Ellipsys but for the highest angles of attack the results of OpenFOAM and Ellipsys are similar. The drag coefficient is under predicted in the linear region by all the programmes. OpenFOAM is giving the closest result to the experimental data for the drag coefficient at highest lift coefficients.

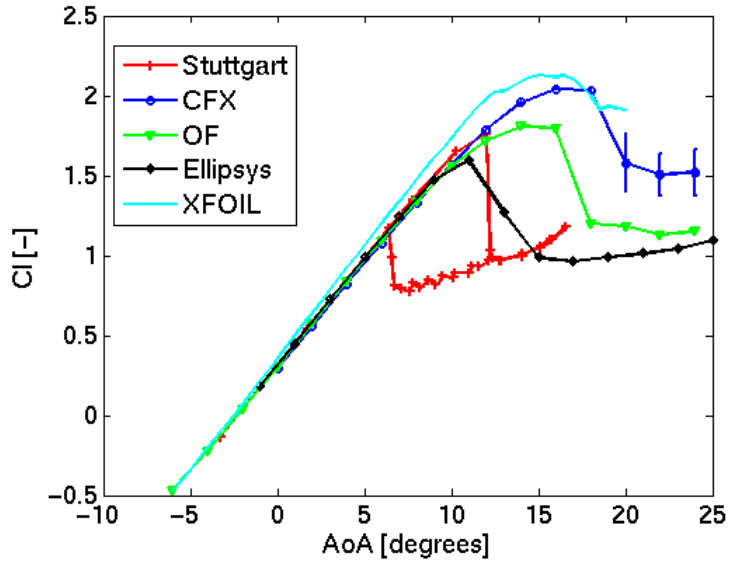

(a) Lift coefficient.

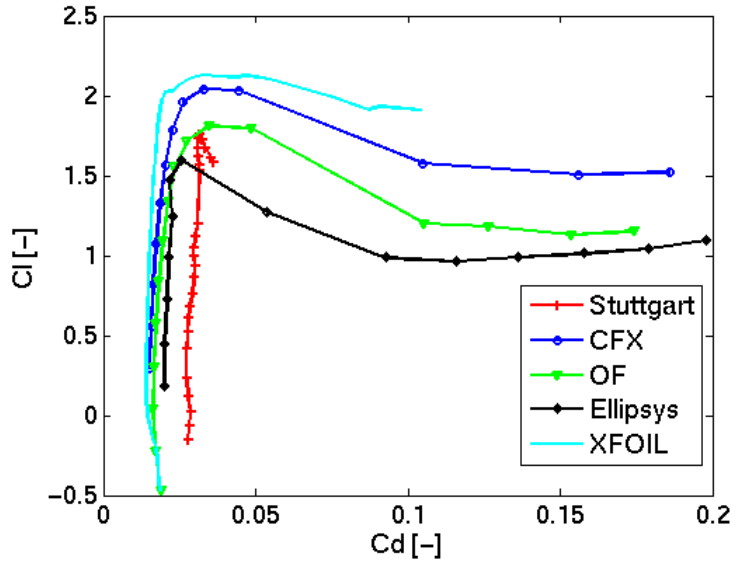

(b) Drag coefficient.

Figure 5.7: Aerodynamic coefficients for the airfoil FX-77-W-400 at Re=4.000.000.

5.4 Comparison of different CFD codes for the airfoil FX-77-W-500

Figures 5.8a and 5.8b show the lift and drag coefficients respectively for the airfoil FX-77-W-500. It can be seen that, for this airfoil, OpenFOAM shows very good agreement with results obtained with ANSYS CFX for both lift and drag coefficient curves until the airfoil begins to stall. For this airfoil simulated, Ellipsys is the programme that shows better agreement with the experimental results.

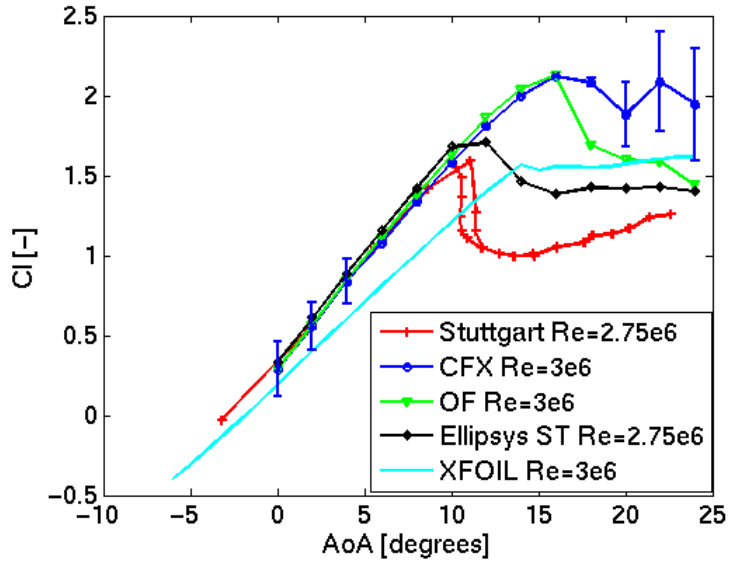

(a) Lift coefficient.

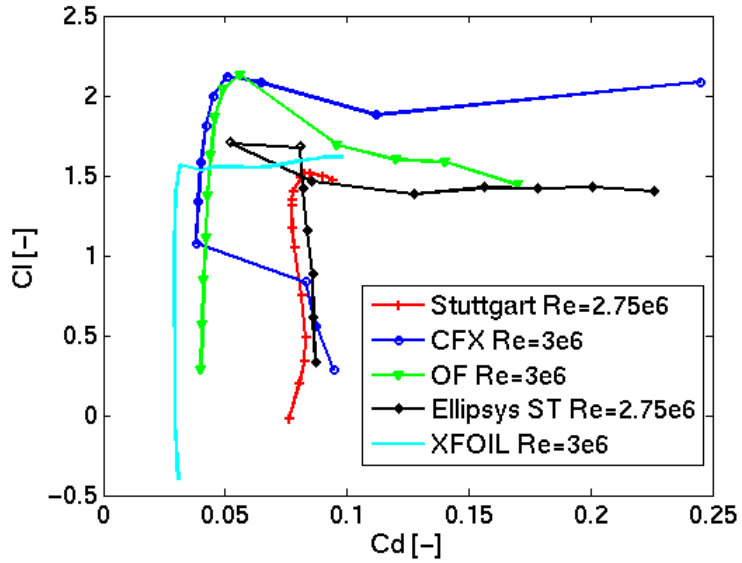

(b) Drag coefficient.

Figure 5.8: Aerodynamic coefficients for the airfoil FX-77-W-500 at the Reynolds number specified.

5.5 Comparison of the performance of the airfoils FX-77-W studied

The aerodynamic characteristics of the airfoils FX-77-W are are compared at this point of the report even though this is not relevant for the study of the flatback airfoils or the validation of the programme OpenFOAM. In order to do this comparison they are observed the force coefficient curves for all of them, obtained with wind tunnel experiments and with CFD simulations. The experimental data and the results obtained with Ellipsys given are for different Reynolds number for each airfoil, then the computations of the airfoils FX-77-W-343 and FX-77-W-400 done with OpenFOAM and ANSYS CFX were done with the same Reynolds number as for the data given ([26] and [27]). Then, once the programme OpenFOAM had already been compared with these two other programmes it was thought to do do a comparison of these three FX-77-W airfoils, this is the reason why the airfoil FX-77-W-500 is simulated for a Reynolds number of 3.000.000 instead of 2.750.000 as the data given, thus it is got data at the same Reynolds number as the one got for the airfoil FX-77-W-343.

In figures 5.9 and 5.10 the experimental results for the airfoils FX-77-W are compared. It can be seen that the airfoil with less relative thickness (FX-77-W-343) presents higher lift coefficient than the other ones for all the angles of attack shown. Also, the thicker the airfoil the sooner it begins to stall, based on this experimental results. It can be seen that the airfoils FX-77-W-400 and FX-77-W-500 have the same lift coefficient in the linear region of the curve. In figure 5.10 it can be seen that the thicker the airfoil the higher the drag coefficient.

The CFD results obtained with OpenFOAM are also shown in figures 5.9 and 5.10. Opposite to what it is shown for the experimental results, OpenFOAM is showing higher Cl_{max} the higher the relative thickness gets. A comparison of the results obtained with ANSYS CFX and Ellipsys previously shown are presented in the appendix B. The common conclusions obtained for all the results obtained with CFD are that the thicker the airfoil the later it begins to stall. Thus, after having a look at all the figures shown for both CFD results and experimental results, the conclusions for the airfoils FX-77-W are listed:

- The thicker the airfoil the higher the drag coefficient.
- The airfoil FX-77-W-343 presents higher lift in the linear region than the airfoils FX-77-W-400 and FX-77-W-500. These two last airfoils mentioned present the same lift coefficient in the linear region of the lift coefficient curve.
- In figure 5.10 it is seen that the airfoil FX-77-W-343 is the one that presents higher lift to drag ratio in the linear region of the lift coefficient curve.

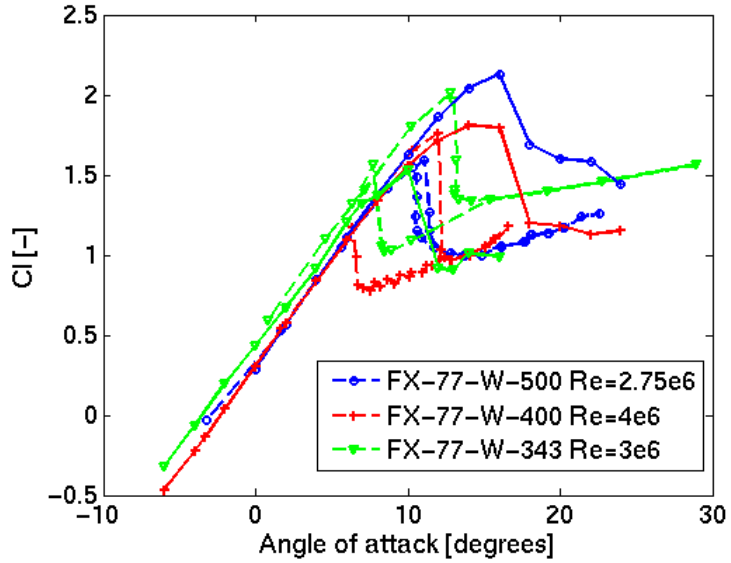

Figure 5.9: Comparison of the results for the lift coefficient of the airfoils FX-77-W at the different Reynolds number specified. OpenFOAM=solid line. Experiments=broken line.

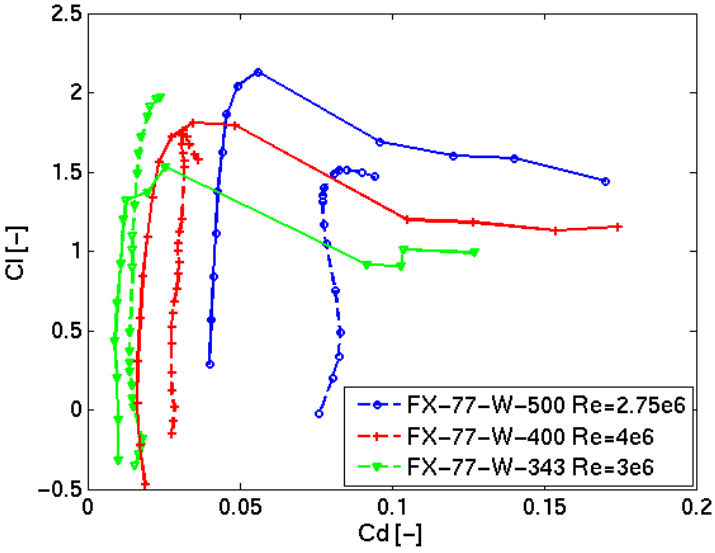

Figure 5.10: Comparison of the results for the drag coefficient of the airfoils FX-77-W at the different Reynolds number specified. OpenFOAM=solid line. Experiments=broken line.

Chapter 6

Thick-flatback airfoils validation

In this chapter it is going to be done a validation of the programme OpenFOAM with thick-flatback airfoils that had already been studied. These airfoils are designed based in the airfoil FB-3500-0050, i.e. the trailing edge of the mentioned airfoil is opened similarly to both the pressure and the suction side in order to get the desired thickness at the trailing edge. They are studied by Sandia Laboratories in wind tunnel experiments as it is explained in [3].

The flatback airfoils studied are the FB-3500-0875 and the FB-3500-1750, their geometries are shown in figure 6.1 and table 6.1. The first number of the name of the airfoil indicates the thicknesses of the different airfoils, i.e. they have a relative thickness of 35 % and the second number indicates the thickness of the trailing edge relative to the chord, i.e, they have trailing edge thicknesses of both 0.5 %, 8.75% and 17.5 %. The airfoil FB-3500-0050 is said to have a trailing edge thickness of 0.5 % because physically all the blades or wind tunnel models will have a trailing edge thickness which will not be 0. However, the airfoil computed has a thickness of 0.

The characteristics of the computations for these airfoils, meshes and parameters (such as turbulence intensity and eddy viscosity ratio) are the same as the ones explained for the airfoils FX-77-W in 5. In reference [3], where the experimental procedure followed is explained, it is stated that the wind tunnel used in order to experiment these airfoils has also low turbulence levels (<0.1 %).

	Max. thickness	at x/c	Max. camber	at x/c
FB-3500-0050	34,8 %	31,3 %	1,75 %	86,4 %
FB-3500-0875	34,99 %	34,9 %	1,87 %	84,8 %
FB-3500-1750	34,88 %	31,3 %	1,88 %	86,3 %

Table 6.1: Characteristics of the airfoils shown in 6.1 relative to the chord.

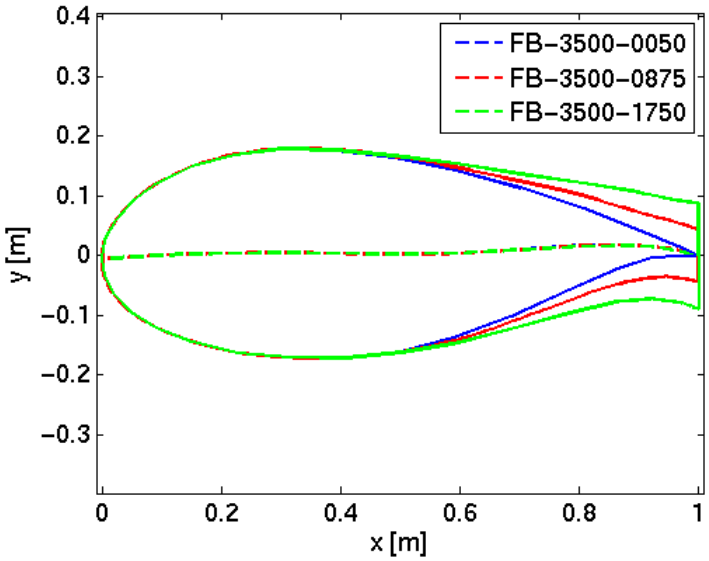

Figure 6.1: Comparison of the geometry of the airfoil flatback FB-3500-XXXX studied.

6.1 Comparison of different CFD codes for the airfoil FB-3500-0050

In figures 6.2 they are shown the experimental results, the CFD results and the results obtained with XFOIL for the airfoil FB-3500-0050. Since this one has a sharp trailing edge it has been used a C-mesh with the same distribution of cells explained in appendix A for the NACA0012 with the sharp trailing edge. It can be seen very good agreement with the experimental results for the results obtained with OpenFOAM. ANSYS CFX results, even though having used the same mesh as in OpenFOAM present the oscillations shown while plotting the standard deviation. As it was said in a previous point of the report, the standard deviation of the results for the other curves are not shown because they are negligible.

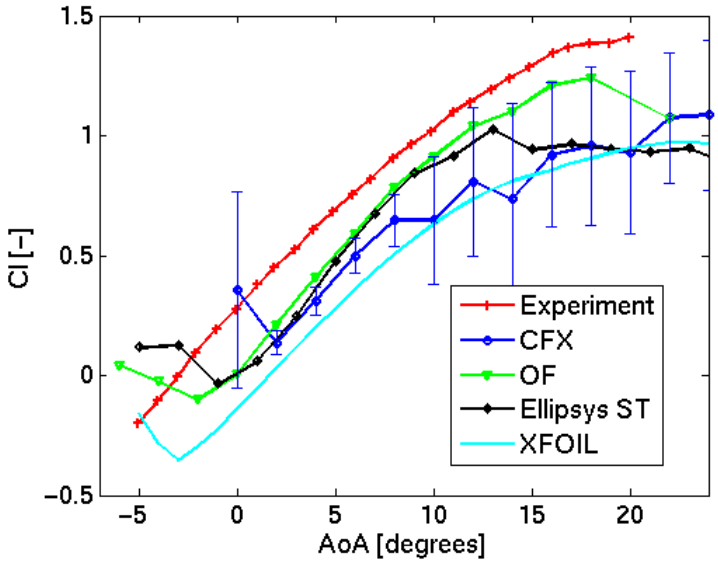

(a) Lift coefficient.

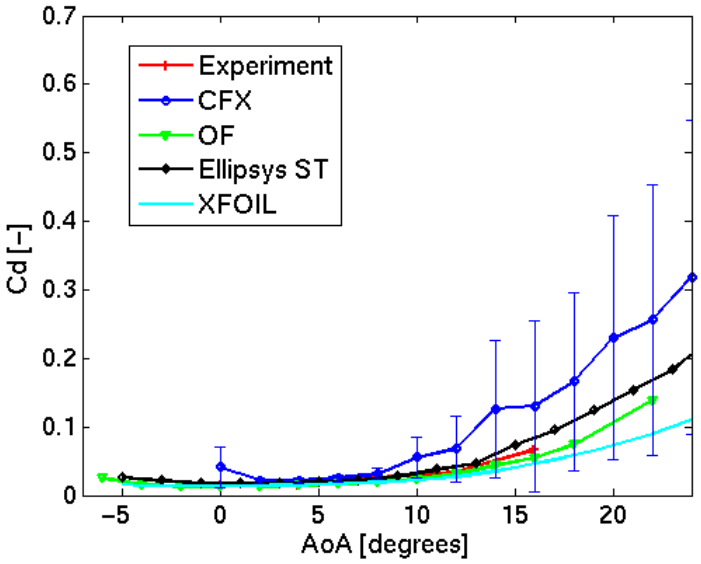

(b) Drag coefficient.

Figure 6.2: Aerodynamic coefficients for the airfoil FB-3500-0050 at Re=666.000.

6.2 Comparison of different CFD codes for the airfoil FB-3500-0875

The comparison between the solution obtained with the different programmes used for this flatback airfoil is shown in figures 6.3. It can be seen that all the programmes predict the linear region well compared to the experimental data but OpenFOAM is over predicting Cl_{max}, while the other two programmes used give a solution closer to the experiments realized.

It is seen, while having a look at the figures of the mesh dependence studies for the airfoil FB-3500-0875 (shown in appendix H) and the polar curves for this airfoil (figures 6.3a and 6.3b) that, while increasing the number of cells a result closer to CFX is obtained (i.e. lower lift coefficient and higher drag coefficient).

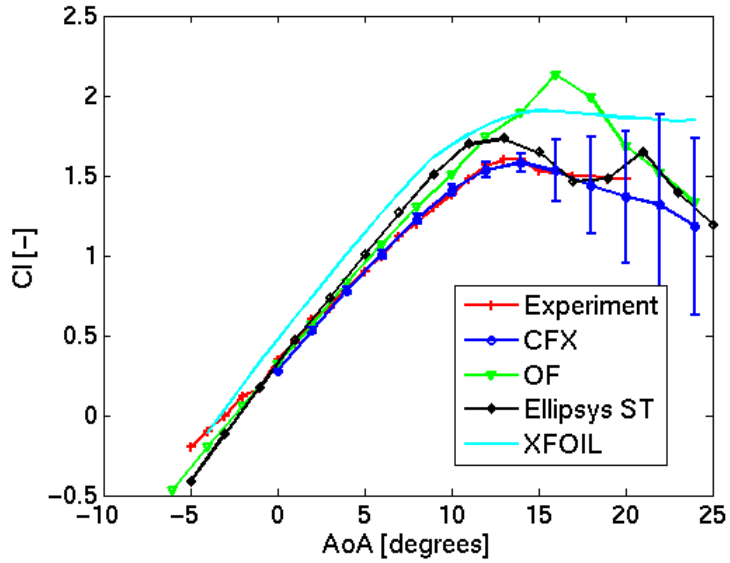

(a) Lift coefficient.

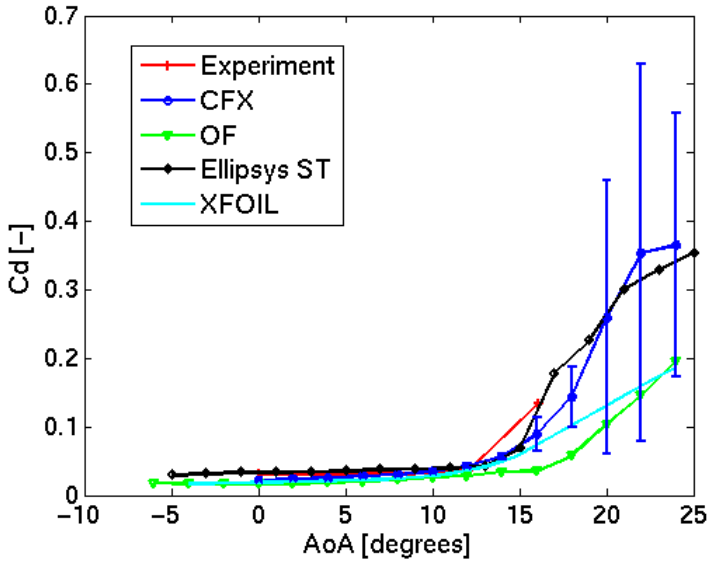

(b) Drag coefficient.

Figure 6.3: Aerodynamic coefficients for the airfoil FB-3500-0875 at Re=666.000.

6.3 Comparison of different CFD codes for the airfoil FB-3500-1750

As it happened in the previous flatback airfoil computed the Cl_{max} is over predicted with OpenFOAM as it can be seen in figure 6.4a. The programme ANSYS CFX is the one that predicts better the stall while comparing the CFD results with experimental results, but as it is seen oscillations in the solution given for the steady simulation appear once the airfoil is stalled. The drag coefficient, shown in figure 6.4b, is very well predicted by Ellipsys in the linear region of the lift curve (the only zone where experimental results are given). Both OpenFOAM and ANSYS CFX under predict this drag coefficient.

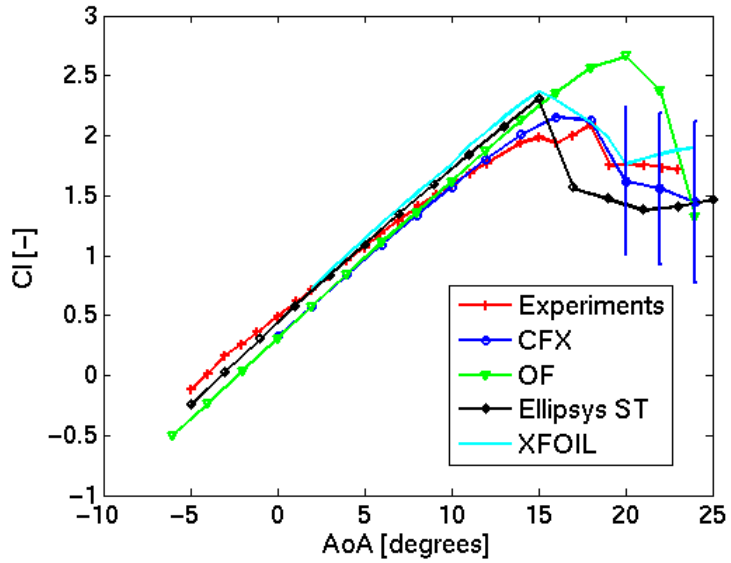

(a) Lift coefficient.

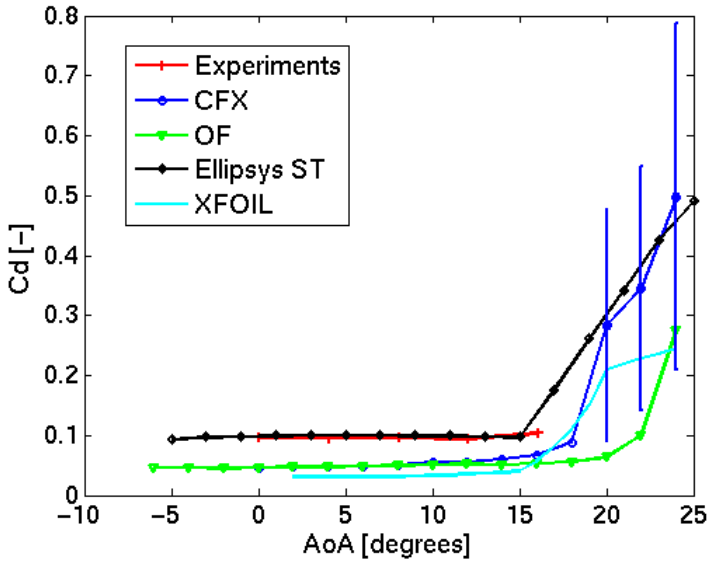

(b) Drag coefficient.

Figure 6.4: Aerodynamic coefficients for the airfoil FB-3500-1750 at Re=666.000.

6.4 Comparison of the performance of the airfoils FB-3500 studied

In figure 6.1 it is done a comparison of the geometries of the flatback airfoils created after opening the trailing edge of the airfoil FB-3500-0050.

The results for these airfoils are compared in figures 6.5, 6.6 and 6.7 for both experimental and CFD results obtained with OpenFOAM. The CFD results obtained with both ANSYS CFX and Ellipsys are shown in appendix C. By looking at all these figures, the conclusions for these airfoils FB-3500 are:
- The thicker the thickness of the trailing edge (i.e. the more the trailing edge is opened), the higher lift coefficient is obtained.
- The thicker the thickness of the trailing edge, the higher drag coefficient is obtained. This is clearly seen for the experimental results and for the results of the computations with Ellipsys but it can not be as clearly appreciated for the computations with OpenFOAM. However, as it has been said while commenting the mesh dependence studies for the airfoil in H, changes in the drag coefficient appear while refining the mesh. Thus, the drag coefficient curve for the airfoil FB-3500-0875 shown in 6.6 would not be as close to the drag coefficient curve for the airfoil FB-3500-0050.
- While having a look at figure 6.7, it can be seen that OpenFOAM's results show a desirable trend for the lift-to-drag ratio for angles of attack higher than 18 degrees, i.e. this ratio increases the higher the trailing edge thickness. There are no experimental results at this angles of attack, but for low angles of attack (from 0 to 6 degrees) the experimental results show that the higher the thickness of the trailing edge, the lower this lift-to-drag ratio.

Contour and streamlines plots of the airfoils FB-3500

They are done contour plots of the velocity and turbulent kinetic energy fields for the airfoils FB-3500 at an angle of attack of 14 degrees in order to see how the flow is behaving around the different airfoils. While increasing the thickness of the trailing edge, it can be seen in figures 6.8, 6.9 and 6.10 how the flow is more attached to the airfoil, this is the reason why higher lift coefficient is seen in figure 6.5 for all the angles of attack for the airfoil with the thickest trailing edge. In figure 6.11 it can be seen the Cp curve for the airfoils FB-3500, it can be appreciated that the Cp curve is much smaller for the airfoil FB-3500-0050 than for the flatback airfoils.

Regarding the friction coefficient curves for all the airfoils FB-3500 shown in 6.12, it can be seen that this C_f on the suction side is higher the thicker the trailing edge of the airfoil is, this yields to higher drag the thicker the trailing edge, as it is seen in figure 6.6 for an angle of attack of 14 degrees.

Comparing figures 6.13 and 6.14 it can be seen that bigger standing vortexes are found around the airfoil FB-3500-1750 than for the airfoil FB-3500-

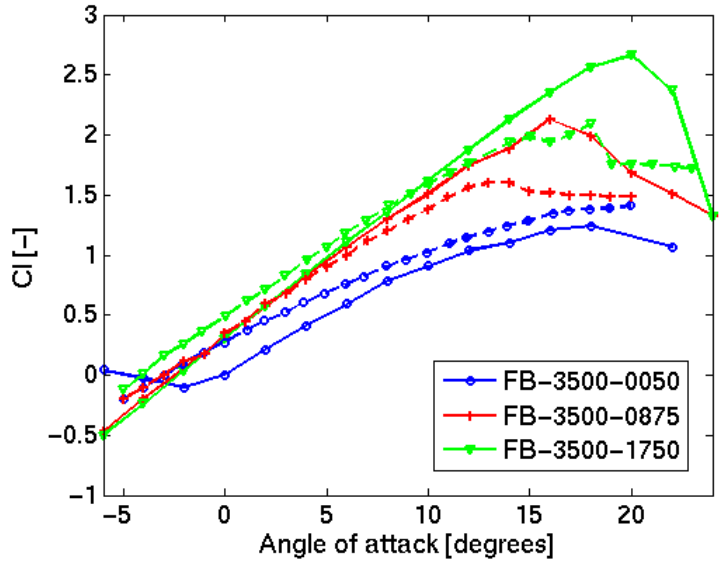

Figure 6.5: Comparison of the the lift coefficient for the airfoils FB-3500 at Re=666.000. OpenFOAM = solid line, Experiments = broken line.

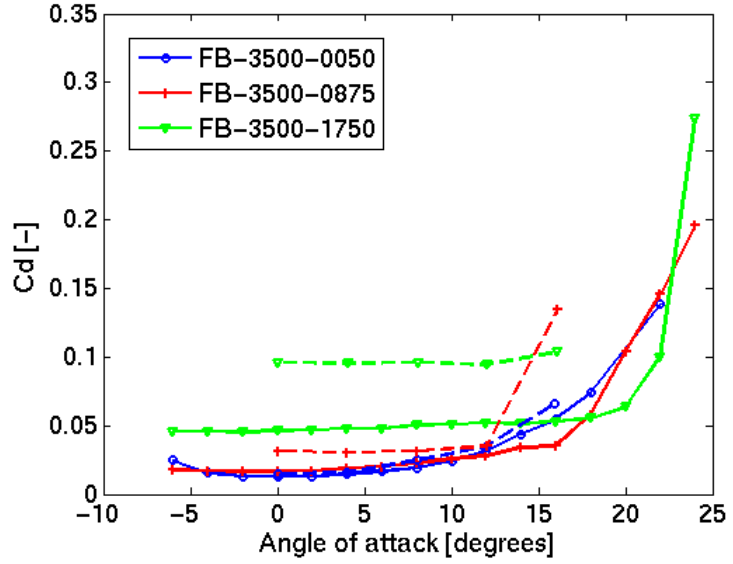

Figure 6.6: Comparison of the drag coefficient for the airfoils FB-3500 at Re=666.000. OpenFOAM = solid line, Experiments = broken line.

0050. This is also seen in the wake, close to the trailing edge, at figures 6.8 and 6.10.

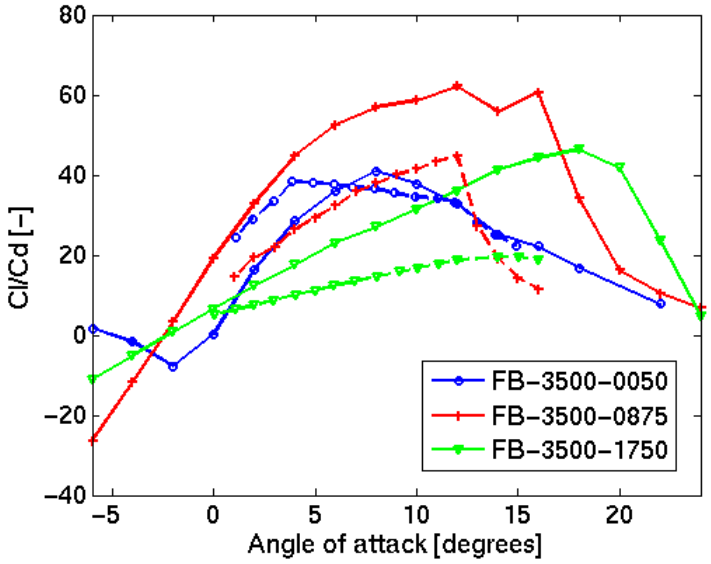

Figure 6.7: Comparison of the lift to drag ratio of the airfoils FB-3500 at Re=666.000. OpenFOAM = solid line, Experiments = broken line.

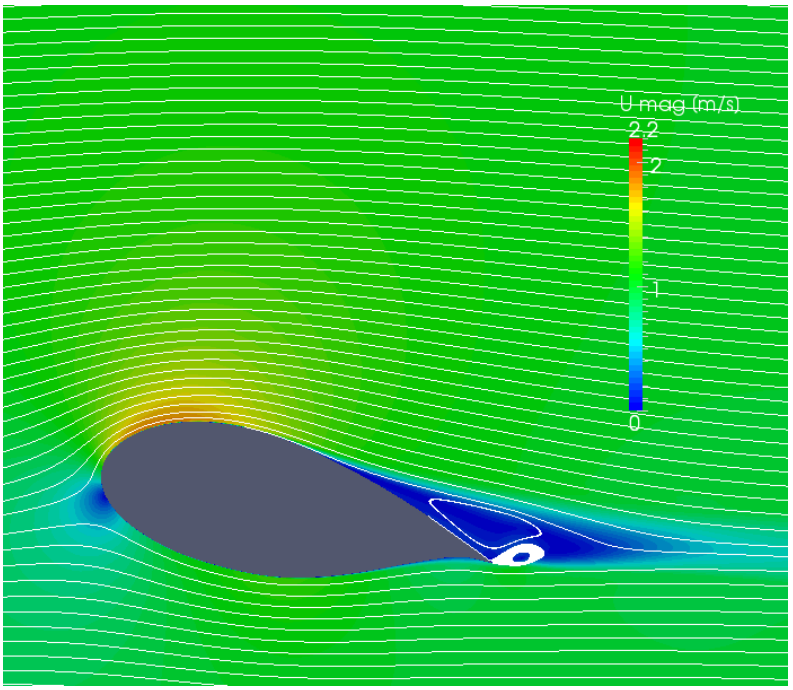

Figure 6.8: Streamlines for the airfoil FB-3500-0050 at an angle of attack of 14 degrees at Re=666.000.

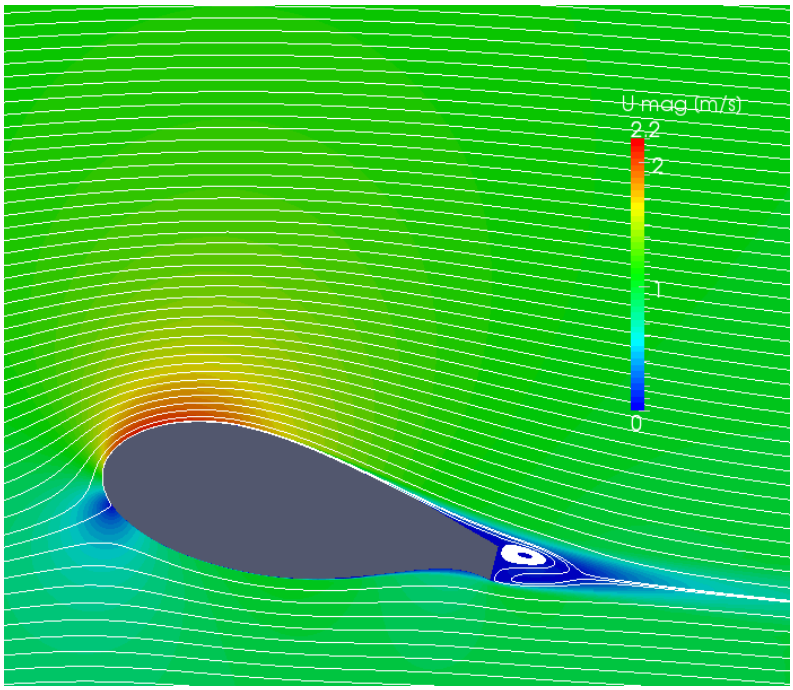

Figure 6.9: Streamlines for the airfoil FB-3500-0875 at an angle of attack of 14 degrees at Re=666.000.

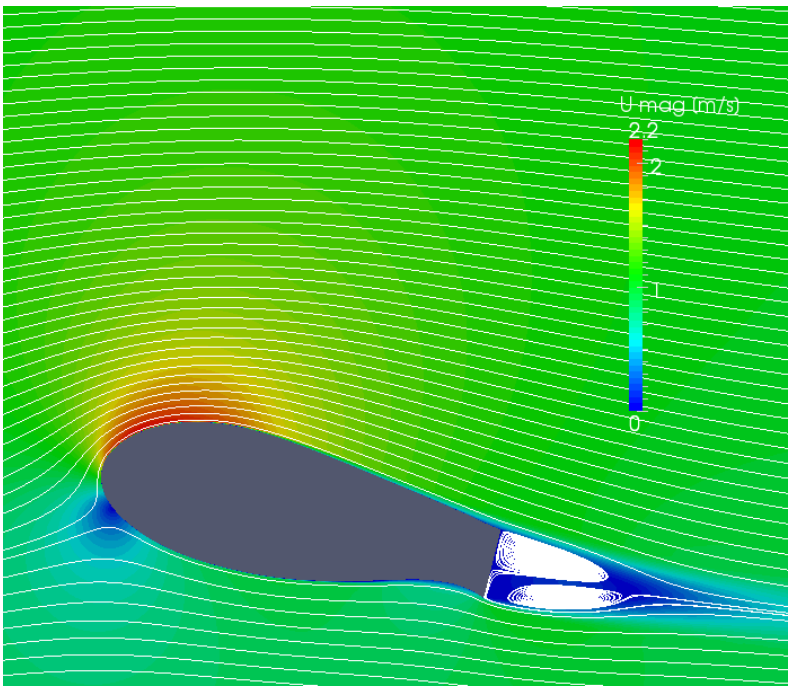

Figure 6.10: Streamlines for the airfoil FB-3500-1750 at an angle of attack of 14 degrees at Re=666.000.

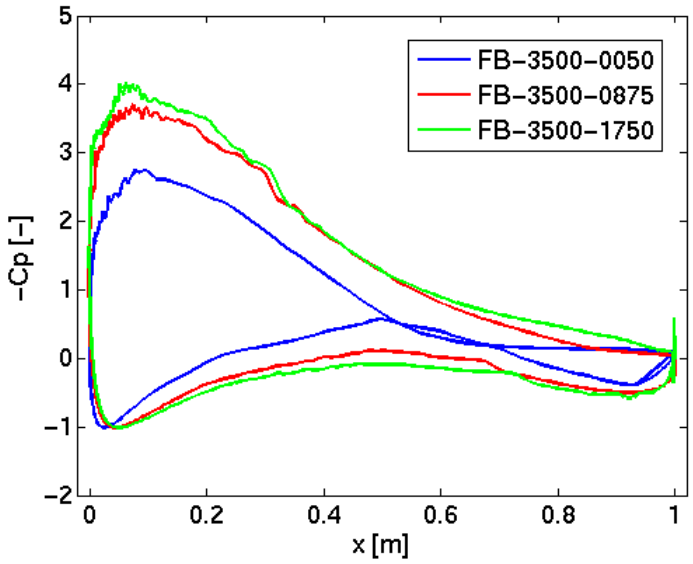

Figure 6.11: Cp curves for the airfoils FB-3500 simulated with OpenFOAM for an angle of attack of 14 degrees at Re=666.000.

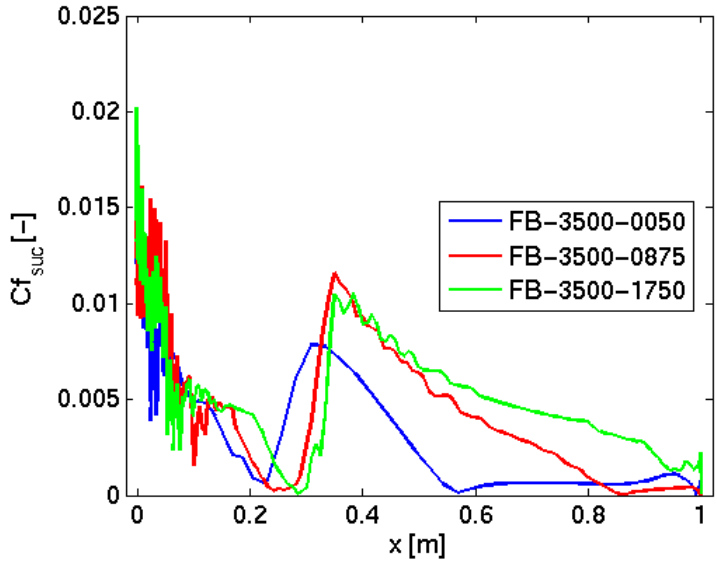

(a) Suction side.

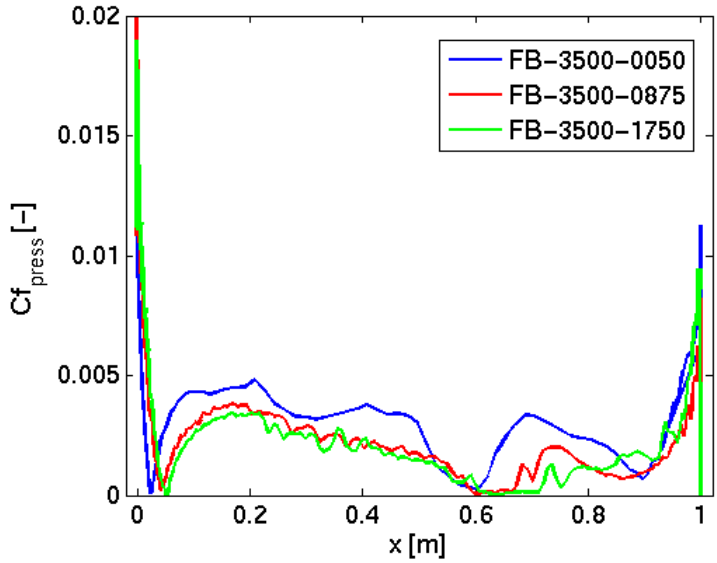

(b) Pressure side.

Figure 6.12: Friction coefficient curves for the airfoils FB-3500 simulated with OpenFOAM for an angle of attack of 14 degrees at Re=666.000.

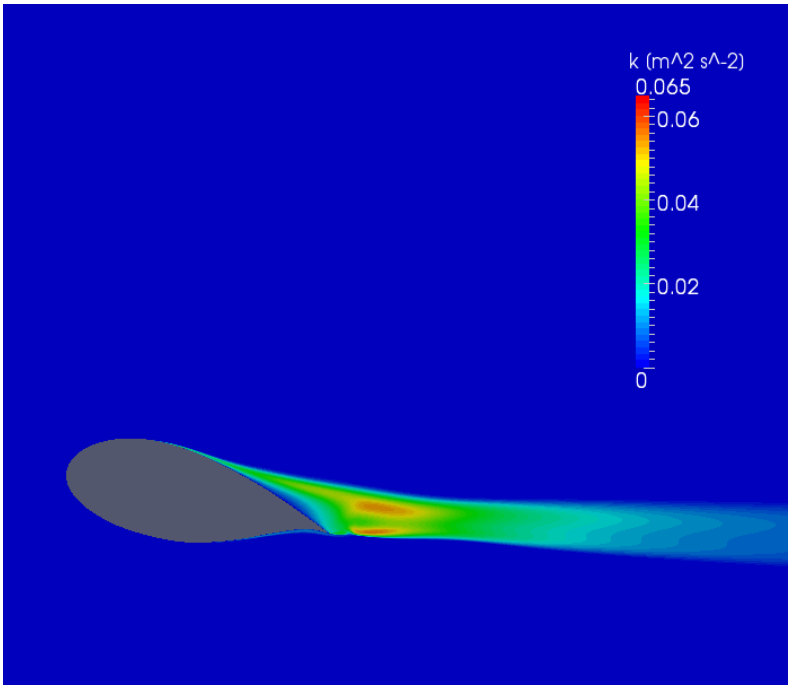

Figure 6.13: Turbulent kinetic energy field for the airfoil FB-3500-0050 at an angle of attack of 14 degrees at Re=666.000.

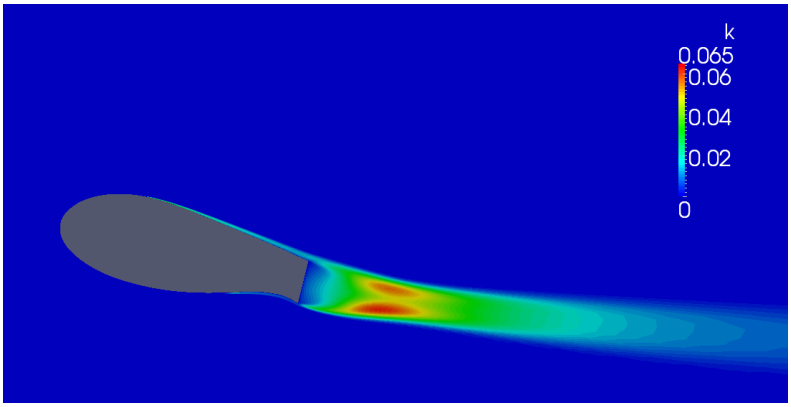

Figure 6.14: Turbulent kinetic energy field for the airfoil FB-3500-1750 at an angle of attack of 14 degrees at Re=666.000

Transition point for the airfoils FB-3500

In figure 6.15 it can be seen a comparison of the location of the transition point at both suction and pressure sides of the airfoils FB-3500. As it can be seen in figure 6.15a, the thicker the trailing edge gets, the closer this transition point is to the trailing edge. This involves bigger laminar region of the boundary layer, i.e. higher velocities and suction at the region of the upper side of the airfoil where the suction peak is found. This can be seen in figure 6.11.

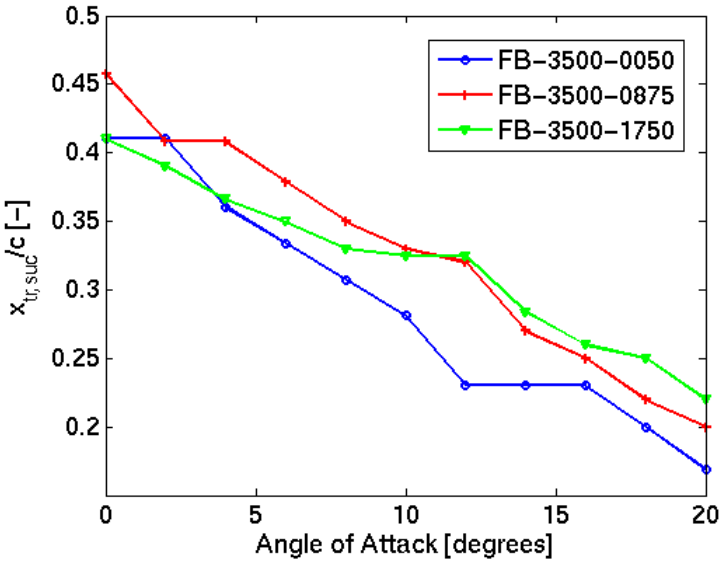

(a) Suction side.

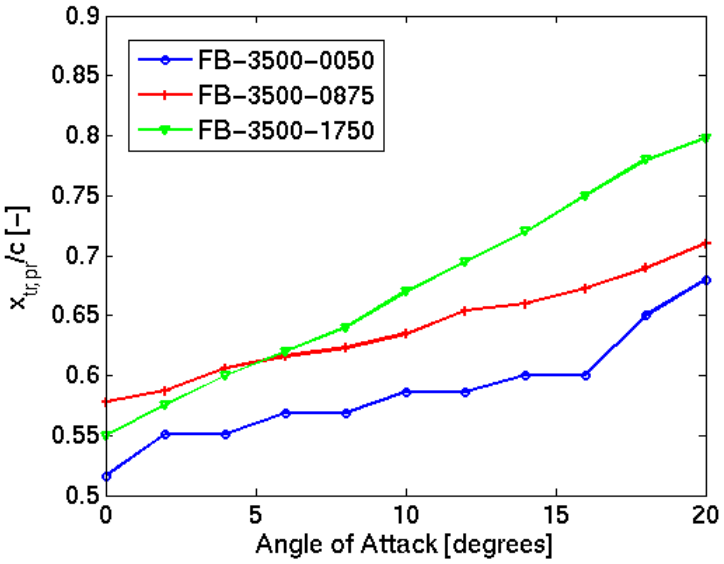

(b) Pressure side.

Figure 6.15: Comparison of the location of the transition point for the different airfoils specified at Re=666.000.

6.5 Study of the flow around flatback airfoils

While trying to think on the behavior of the flow and why is happening that the flatback airfoils have higher lift than the original airfoil out of which they are created it is thought that the flow around FB-3500-1750 is behaving as if it was around a longer airfoil, with the same shape and the trailing edge in the dead water region behind the airfoil FB-3500-1750 shown in figure 6.10.

It was decided to generate two new airfoils from airfoil FB-3500-1750, the geometry of them is shown in figure 6.18. In order to do that it was studied the profile of the wake, shown in figure 6.17 and the vector field of the velocities shown in figure 6.17. The size of the airfoil was increased making sure that the tail of the new airfoil was inside the wake of the airfoil FB-3500-1750.

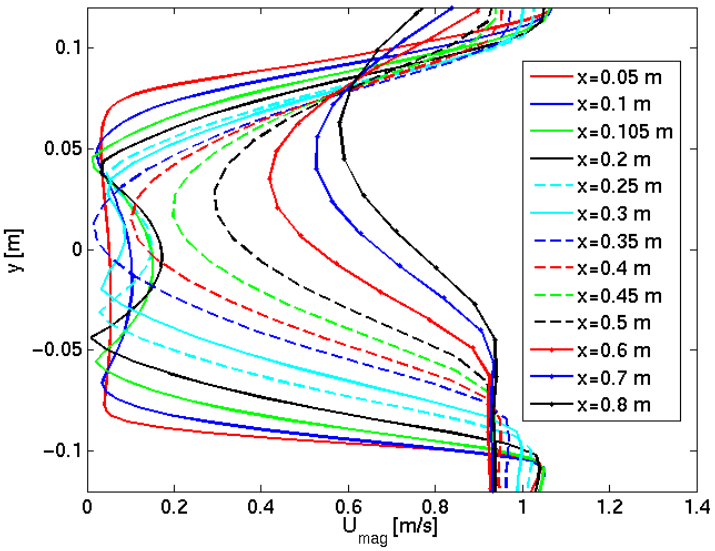

Figure 6.16: Comparison of the magnitude of the velocity at the wake of the airfoil FB-3500-1750 at a distance x from the trailing edge. Re=666.000 and angle of attack 14 degrees.

In table 6.2 they are shown the differences between the aerodynamic forces of the different airfoils created and the airfoil they come from after doing addition of chord, the airfoil FB-3500-1750. In figures 6.19 and 6.20 they are shown both Cp and Cf curves of the airfoils mentioned.

Figure 6.19 shows that the pressure distribution all over the airfoil is very similar for the airfoil FB-3500-1750 and the modifications made to it. This is also shown in the differences of the lift force, shown in table 6.2, because there is almost no difference in the lift forces of the airfoils mentioned. The reason why the airfoil FB-3500-1750 + 35 % chord presents lower lift than the airfoil

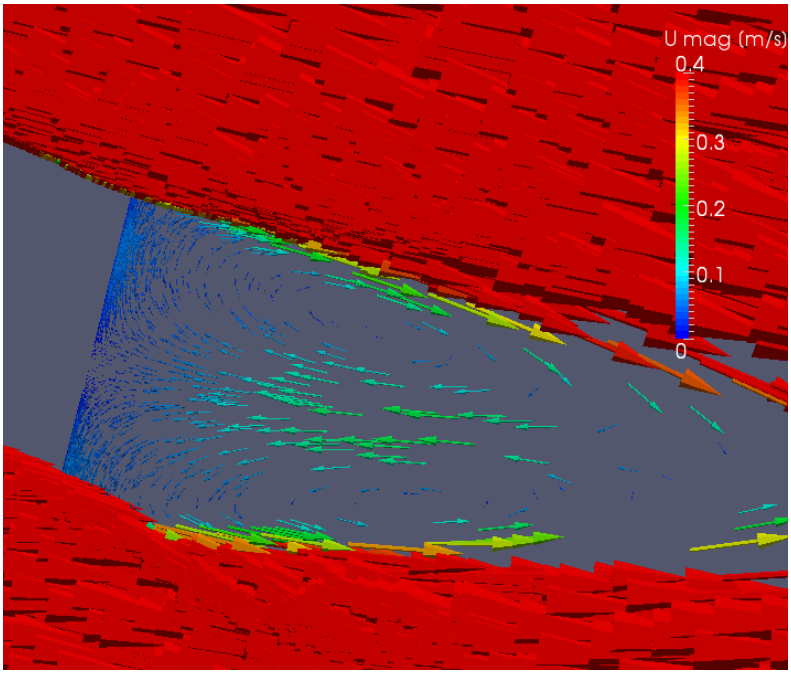

Figure 6.17: Vector field of the velocity at the wake of airfoil FB-3500-1750 at Re=666.000 and an angle of attack of 14 degrees.

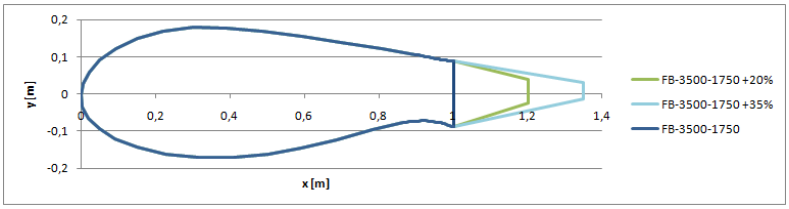

Figure 6.18: Comparison of the geometry of the airfoil FB-3500-1750 and the airfoils generated adding chord downstream in the dead water region.

FB-3500-1750 + 20 % is because the suction present in its pressure side at $x = 1$, seen on the Cp curve of figure 6.19.

The friction coefficient curves shown in figure 6.20 show also very good agreement of the behavior of the flow between the airfoils FB-3500-1750 and the two modifications made to it. It is supposed that the decrease in the drag while making the modifications to the airfoil FB-3500-1750 is due to, while doing so, the trailing edge is decreased and smaller standing vortices are observed. This is shown in the figures of the velocity field and streamlines, figures 6.21 and 6.22, and in the figures of the turbulent kinetic energy 6.23 and 6.24.

Thus, it has been proved that the aerodynamic behavior of the flatback

Airfoil	Lift difference compared to FB-3500-1750	Drag difference compared to FB-3500-1750
FB-3500-0050	-47.378 % chord	-17.77 %
FB-3500-1750 + 20 % chord	0.32 %	-31 %
FB-3500-1750 + 35 % chord	-3.67 %	-42.377 %

Table 6.2: Comparison of the aerodynamic forces of the different airfoils specified at Re=666.000 and an angle of attack of 14 degrees.

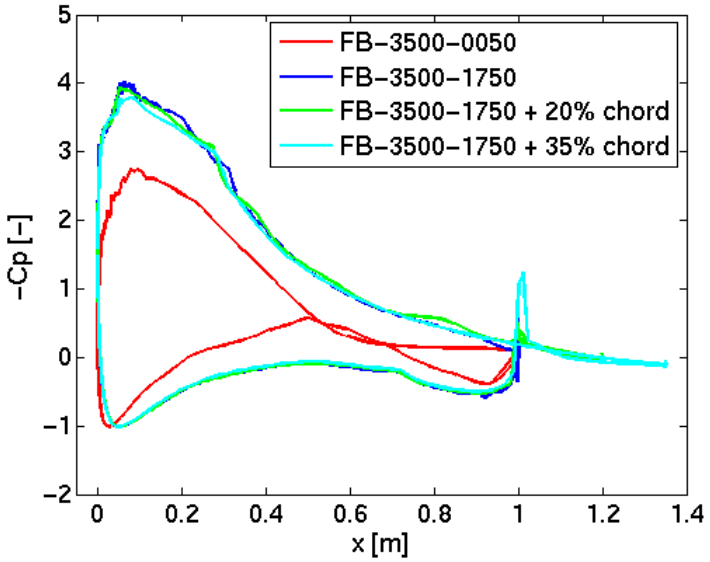

Figure 6.19: Vector field of the velocity at the wake of airfoil FB-3500-1750 at Re=666.000 and an angle of attack of 14 degrees.

airfoils is the same as one airfoil with chord added at the dead water zone created behind it.

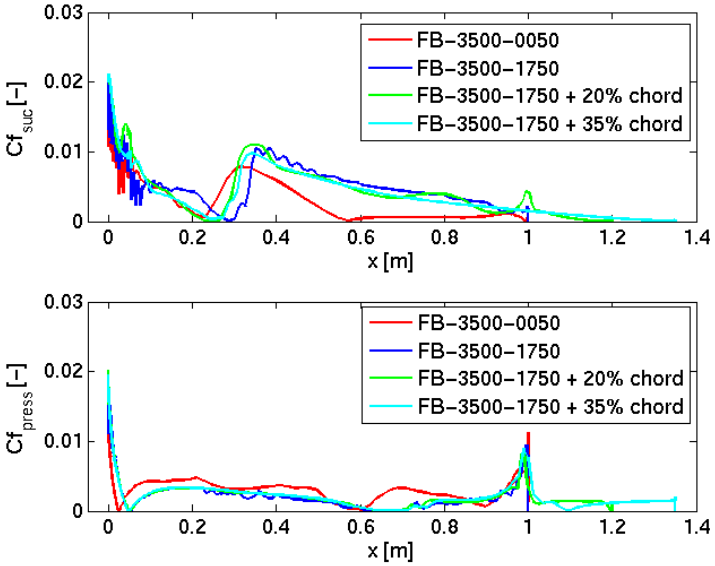

Figure 6.20: Comparison of the geometry of the airfoil FB-3500-1750 and the airfoils generated adding chord downstream in the dead water region.

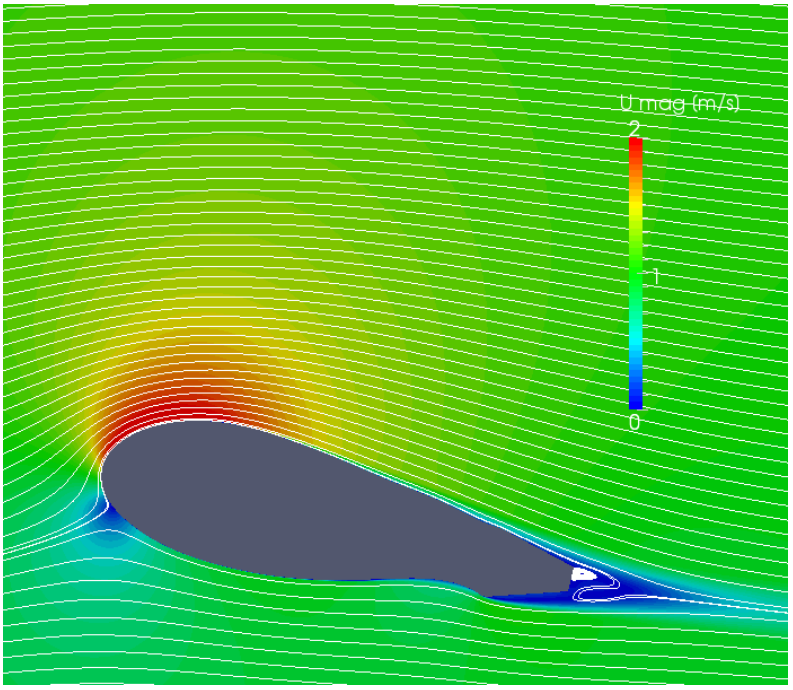

Figure 6.21: Velocity field and streamlines for the airfoil FB-3500-1750 with an addition of 20 % of the chord length into the dead water region shown in figure 6.10. Re=666.000 and angle of attack of 14 degrees.

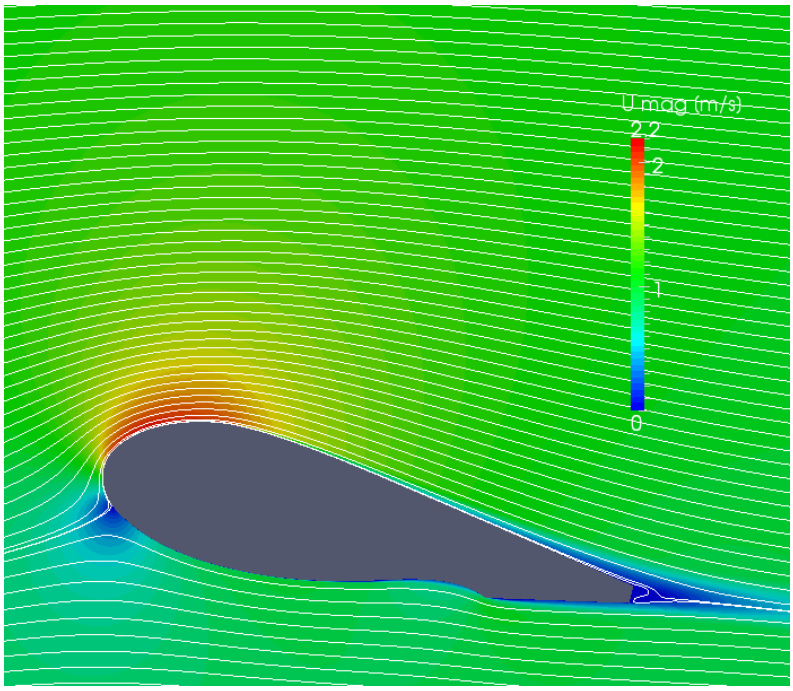

Figure 6.22: Velocity field and streamlines for the airfoil FB-3500-1750 with an addition of 35 % of the chord length into the dead water region shown in figure 6.10. Re=666.000 and angle of attack of 14 degrees.

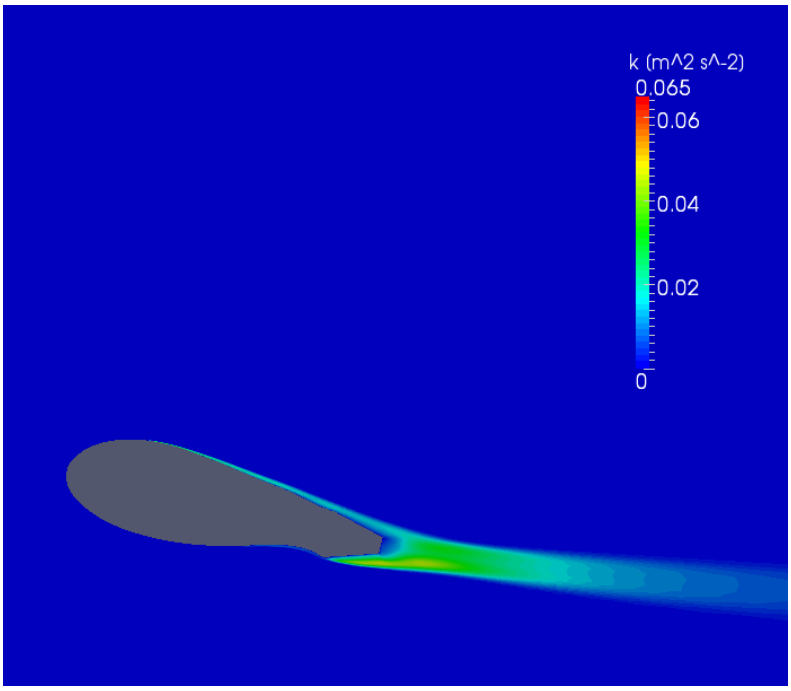

Figure 6.23: Turbulent kinetic energy field for the airfoil FB-3500-1750 with an addition of 20 % of the chord length into the dead water region shown in figure 6.10. Re=666.000 and angle of attack of 14 degrees.

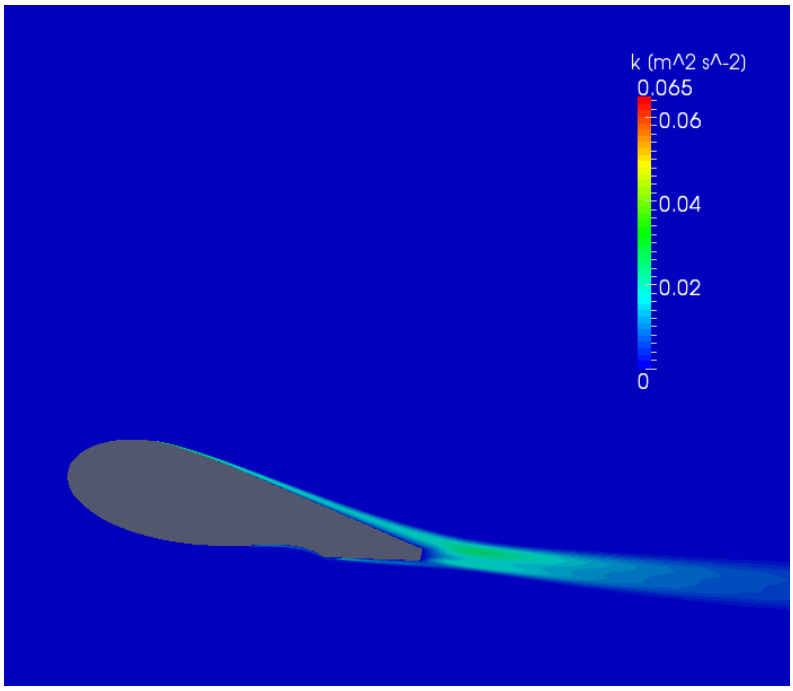

Figure 6.24: Turbulent kinetic energy field for the airfoil FB-3500-1750 with an addition of 35 % of the chord length into the dead water region shown in figure6.10. Re=666.000 and angle of attack of 14 degrees.

Chapter 7

Thick-flatback airfoils study

Once the programme OpenFOAM has been validated by doing the different sensitivity studies shown in chapter 4 and the comparison of cases run with other CFD codes and experimental results shown in chapters 5 and 6, the trailing edge of different airfoils chosen has been thickened in order to study how this is affecting to their performance. The airfoils that are shown in this chapter are run at Re=4.000.000 with free transition at the boundary layer, turbulence intensity at the inlet of 0.07 % and eddy viscosity ratio of 10. The meshes used in order to run the computations have 150.000 cells and the outer boundaries are placed 60 chords away from the airfoil.
They have been studied three airfoils which belong to Suzlon and the airfoil NACA8648 generated with XFOIL as it is explained in 2.10. The coordinates of the airfoils belonging to Suzlon are not given due to proprietary reasons and the results obtained have been normalized. It has been chosen an airfoil with thickness 36 % (called *NEW*), a symmetric airfoil called *NEW sym* obtained after setting 0 camber to the previous airfoil mentioned (thus, it also has a thickness of 36 %) and an airfoil with a thickness of 57 % called *NEW thick*.

7.1 Flatbacking of the airfoils studied

In reference [27] Niels Sørensen, first, studies the airfoil FB-3500-0050 and the modifications made to its trailing edge in order to check how well Ellipsys predicts the behavior of the flow for the flatback airfoils. Once this is done, they are done different openings towards pressure and suction side of the airfoil DU-97-W-300. In this study, the thickness of the trailing edge of this airfoil is increased the same percentage (30 %) by doing different cases. These are thickened differently towards either pressure or suction side (i.e. it is not created a case where the trailing edge of the airfoil is opened 15 % towards both pressure and suction side). The different cases studied by Risø DTU are shown in figures 7.1.

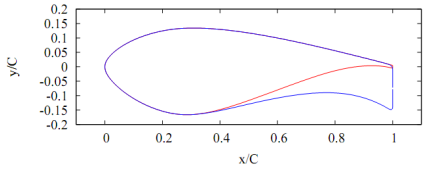

(a) Suction-30 %, Pressure-0 %.

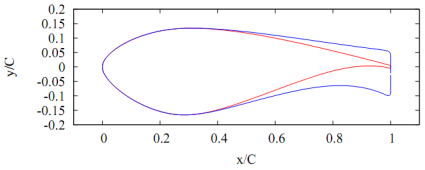

(b) Suction-10 %, Pressure-20 %.

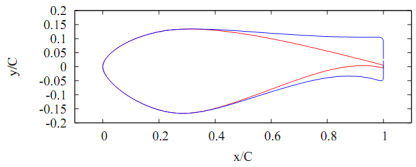

(c) Suction-20 %, Pressure-10 %.

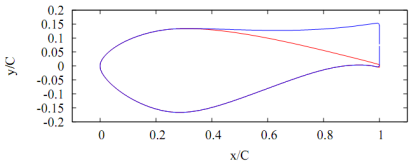

(d) Suction-0 %, Pressure-30 %.

Figure 7.1: Different openings done by Risø DTU at the airfoil DU-97-W-300 (shown in red color). Figures obtained from [27].

The results in [27], shown in figures 7.2 show that for the different cases created the drag coefficient is always increased, as it is shown in figure 7.2b. For the cases where the trailing edge thickness is increased more to the suction side than the pressure side (i.e. an airfoil with higher camber is created) the lift coefficient increases, as it is observed in 7.2a. While, when this camber is decreased by increasing the trailing edge thickness more towards the suction side than the pressure side, this lift coefficient is decreased.

It was decided to thicken the trailing edge of the different airfoils studied the same percentage towards both pressure and suction side.

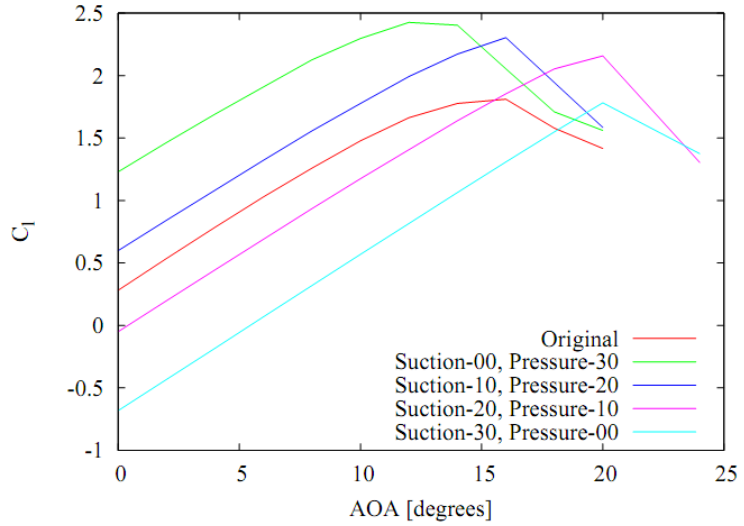

(a) Lift coefficient.

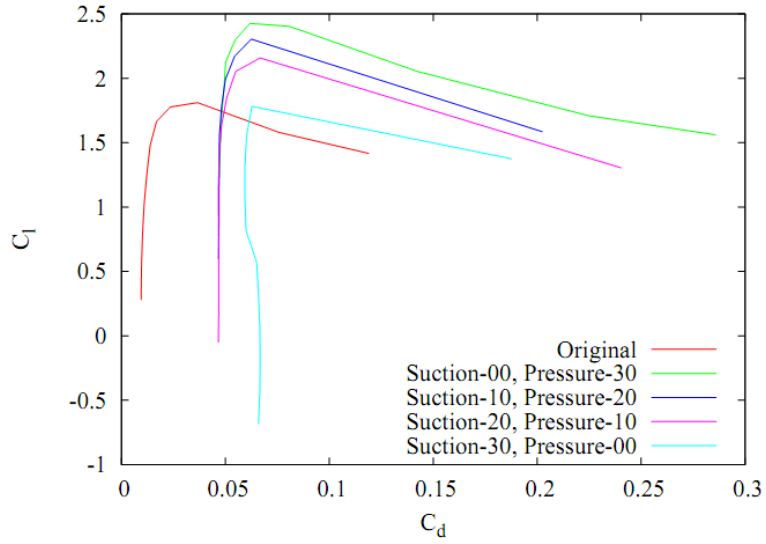

(b) Drag coefficient.

Figure 7.2: Results for the different flatback airfoils created by Risø DTU, shown in figures 7.1. Figures obtained from [27].

7.2 *NEW* flatback airfoils

The coordinates of this airfoil and the maximum camber are not given due to proprietary reasons. As it has been said previously, the first group of flatback airfoils studied have a relative thickness of 36 %. The results shown in 7.3, 7.4 and 7.5 have been normalized with the maximum value of each figure such that the trend after doing the different openings at the different aerodynamic characteristics can be perfectly appreciated even though the actual value of the force coefficients is not given.

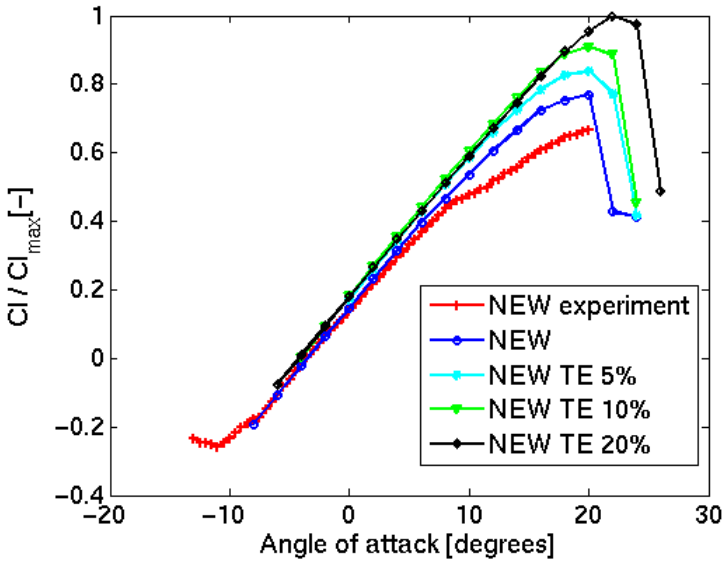

Figure 7.3: Lift coefficient normalized for the airfoil *NEW* at Re=4.000.000.

The results just shown in figures 7.3, 7.4 and 7.5 are compared with results obtained with ANSYS CFX for the same meshes and boundary conditions in the appendix D.

The changes of the shape of both lift and drag curves of the experimental results shown in figures 7.3 and 7.4 indicate that these experiments predict earlier stall than CFD results do. It is not possible either to give details about the wind tunnel used to obtain these results.

For these airfoils, the thicker the trailing edge, the higher the angle of attack at which the airfoil begins to stall. Similarly to what it was seen for the previous flatback airfoils studied (FB-3500-XXXX), results from both OpenFOAM and ANSYS CFX show that the lift coefficient is increasing in the region of the curve where the flow is about to get to Cl_{max}. A maximum increment of the lift coefficient before the stall is observed for the airfoil with a trailing edge thickness of 20 % at an angle of attack of 20 degrees, this is an increment of 24 %. The drag coefficient increases dramatically though, for example, for the

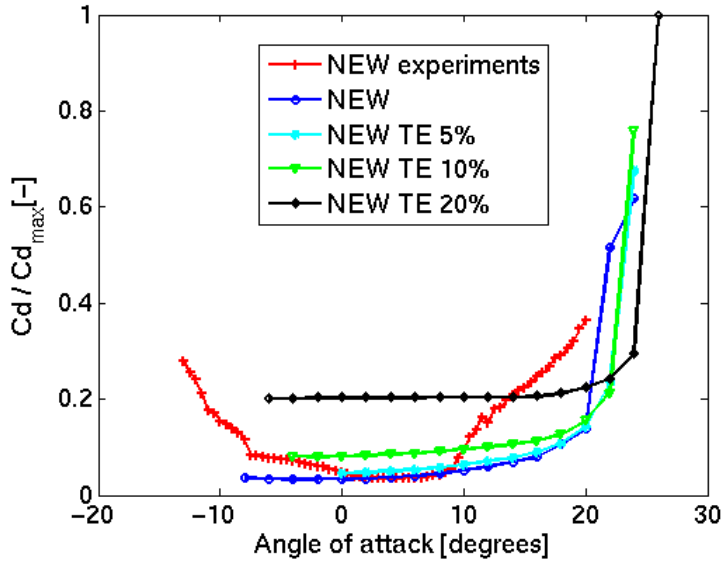

Figure 7.4: Drag coefficient normalized for the airfoil *NEW* at Re=4.000.000.

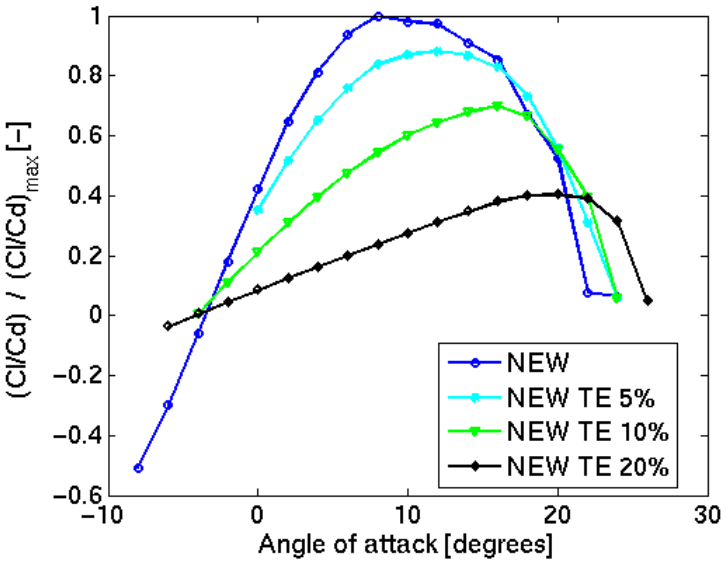

Figure 7.5: Lift-to-drag ratio normalized for the airfoil *NEW* at Re=4.000.000.

same flatback airfoil just mentioned at an angle of attack of 8 degrees there is an increment of 360 %, while for an airfoil which trailing edge has been thickened just 5 % relative to chord, at the same angle of attack this drag increment is of 30 %. However, for all the flatback airfoils generated these changes yield to a big decrease of the lift-to-drag ratio for all the angles of

attack at which the airfoil has not begin to stall as it is shown in figure 7.5.

7.3 *NEWsym* flatback airfoils

The coordinates of this airfoil and the maximum camber are not given either due to proprietary reasons. The normalized results of the computations done for this airfoil are shown in figures 7.6, 7.7 and 7.8. It is seen that the lift obtained at both modified airfoils (with a trailing edge of 10 % and 20 %) is very similar for all the angles of attack, except for the points where the airfoil is stalled. Figure 7.6 and 7.7 show that the airfoils with the modified trailing edge present later stall than the airfoil *NEWsym*. In the linear region, all the airfoils shown in 7.6 have the same lift coefficient at the linear region of the curve shown, but it is possible to obtain higher Cl_{max} with the modified versions. On the other hand, the drag for the airfoil with higher trailing edge thickness is increasing more compared to the drag of the airfoil *NEWsym*. This is the reason why, as it was shown previously for the airfoil *NEW* the lift-to-drag ratio is decreasing while increasing the thickness of the trailing edge.
The results shown in figures 7.6, 7.7 and 7.8 have been computed also with ANSYS CFX, they are shown in the appendix E. The trend observed for the lift-to-drag ratio is the same seen by looking at OpenFOAM's results. However, it is obtained a higher Cl_{max} for the airfoil with the highest thickness at the trailing edge and it presents stall at a higher angle of attack than the airfoil with a thickness of 10 % at the trailing edge. At the angle of attack at which the airfoil *NEWsym* is deep into stall, and for higher angles of attack, it is seen a positive effect of the modifications done to the airfoil *NEWsym*. However, this airfoil would not be supposed to study at such angles of attack.

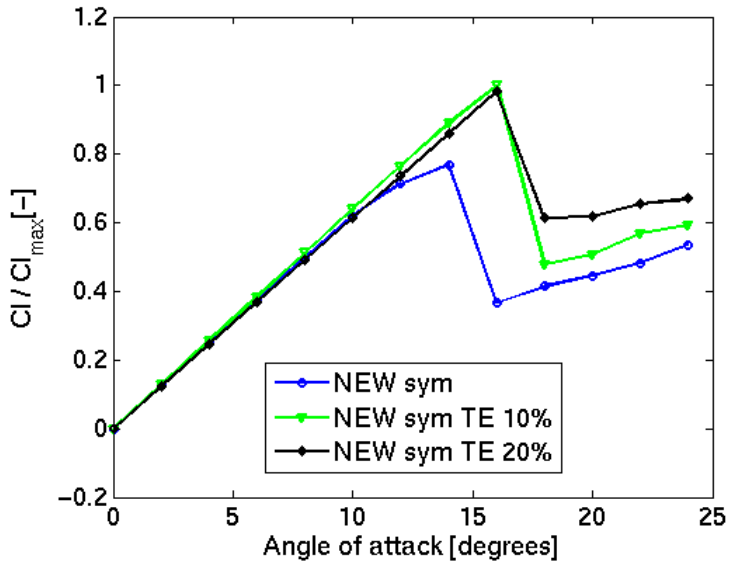

Figure 7.6: Lift coefficient normalized for the airfoil *NEWsym* at Re=4.000.000.

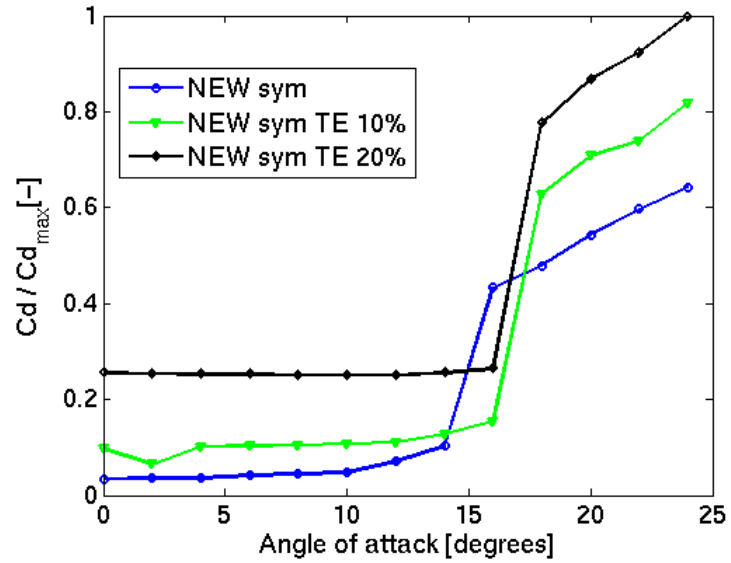

Figure 7.7: Drag coefficient normalized for the airfoil *NEWsym* at Re=4.000.000.

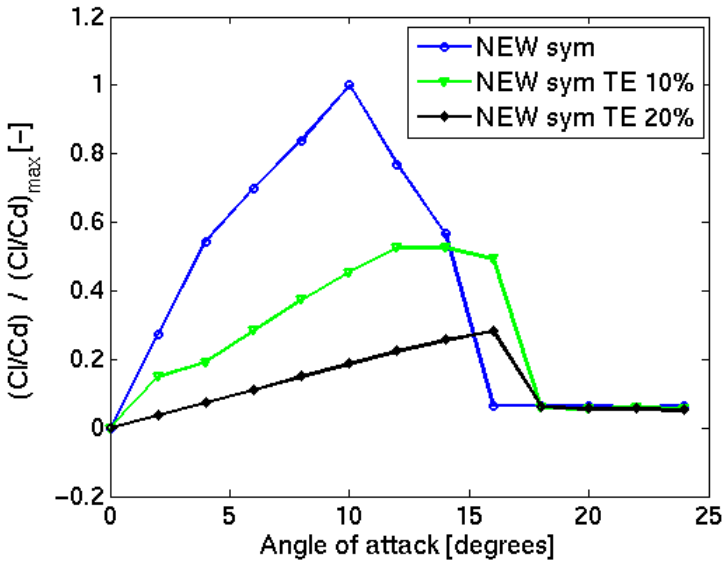

Figure 7.8: Lift-to-drag ratio normalized for the airfoil *NEWsym* at Re=4.000.000.

7.4 *NEWthick* flatback airfoils

For the flatback airfoils studied so far there is no positive effect in terms of lift-to-drag ratio because this decreases while opening the trailing edge. It is said in presentation [8] that while trying to optimize an airfoil with thickness higher than 35 % one may end in an airfoil with a blunt trailing edge. Since the airfoils studied so far have a relative thickness of 35 % (FB-3500-0050) and 36 % (*NEW* and *NEWsym*), which are values very close to the limit stated in this presentation, it is decided to study one airfoil with much more thickness to see the behavior that it presents while making it flatback. It is chosen an airfoil property of Suzlon Blade Technology which has a thickness of 57 %.

The results obtained with OpenFOAM are shown in figures 7.9, 7.10 and 7.11. It is also done a comparison with results obtained with OpenFOAM and ANSYS CFX in appendix F. Both programmes show an increase of the lift coefficient at all the angles of attack while making the airfoils flatback, for example, at an angle of attack of 10 degrees the lift coefficient increases 180 % from the airfoil *NEWthick* to the airfoil *NEWthick TE20*. The drag coefficient, at the angles of attack where the airfoils are not yet stalled, increases a maximum of 20 % for the airfoils with a trailing edge of 5 % and 10 % chord lengths while for the airfoil with a trailing edge of 20 % chord increases between 10 and 85 %. This yields to a higher lift-to-drag ratio at the points where the airfoil is not yet stalled, for example, thereis an increment of 120 % while thickening the trailing edge of the airfoil *NEWthick* 20 % relative to chord. Thus, based on these CFD results it would be positive to use the flatback airfoils with the trailing edge thickened up to 20 % at the sections where they are supposed to work, which are at angles of attack between 12 and 16 degrees. However, there is one limit that has to be taken into account in the different openings done at the trailing edge. For example, the airfoil *NEWthick TE30*, does not follow this trend shown while increasing the trailing edge thickness up to 20 % at the range of angles of attack these airfoils work, this is due to the huge increase in the drag coefficient that this airfoil presents. This airfoil though, presents better performance at the highest angles of attack than the other airfoils do.

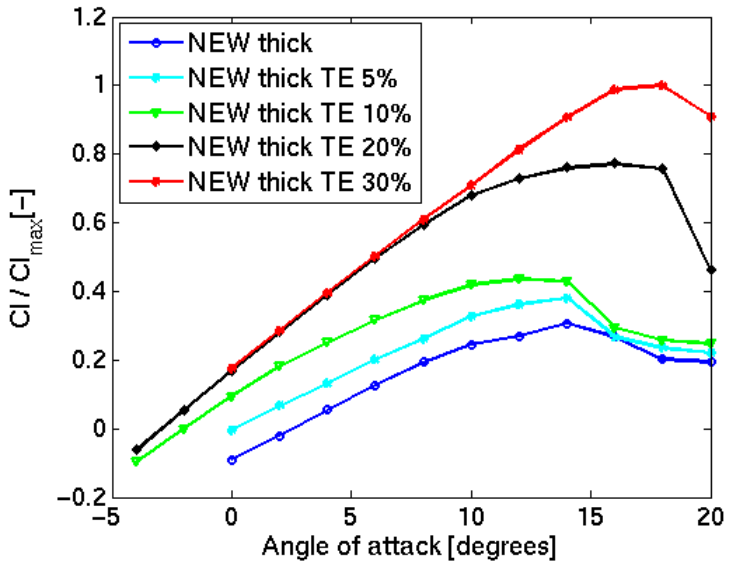

Figure 7.9: Lift coefficient normalized for the airfoil *NEWthick* at Re=4.000.000.

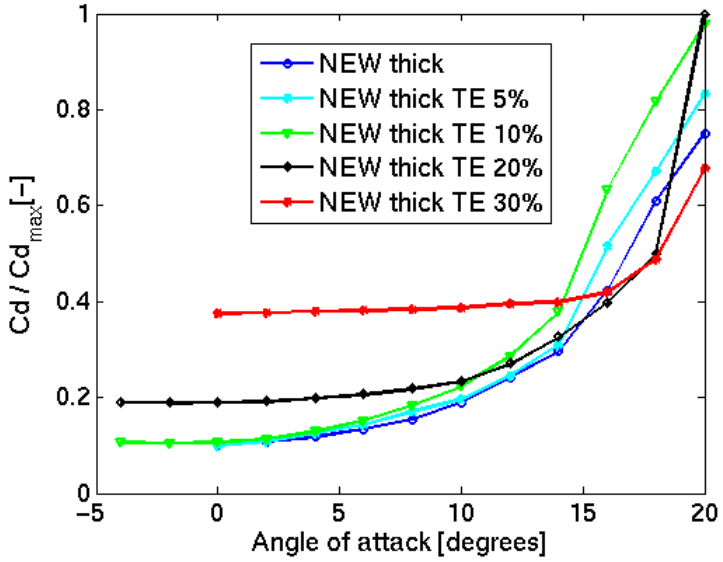

Figure 7.10: Drag coefficient normalized for the airfoil *NEWthick* at Re=4.000.000.

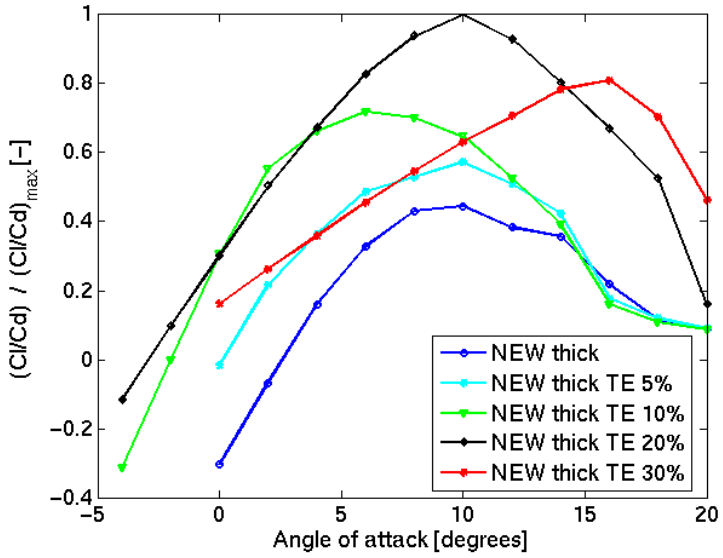

Figure 7.11: Lift-to-drag ratio normalized for the airfoil *NEWthick* at Re=4.000.000.

7.5 NACA8648 flatback airfoils

The four-digit series NACA airfoil, NACA8648 and the corresponding flatback airfoils made after opening its trailing edge have been generated using XFOIL. This airfoil has a thickness of 48 %, thus, it can be seen how the performance of a very thick airfoil (but not that thick as the previous one, which had a relative thickness of 57 %) is affected after making it flatback. The geometry of this airfoil is shown in figure 7.12 and table 7.1.

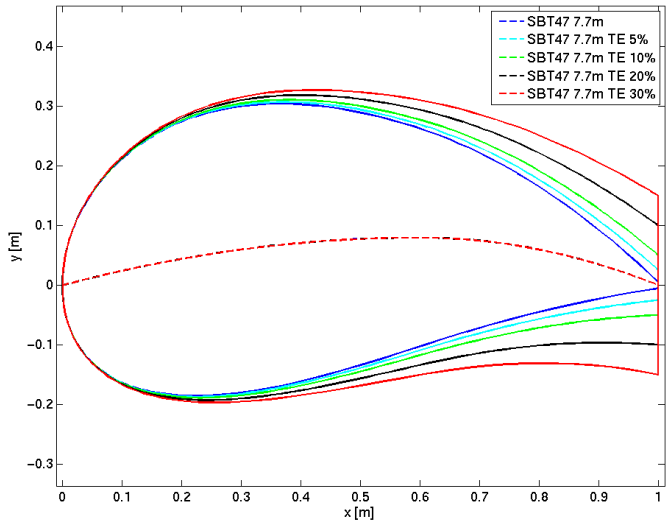

Figure 7.12: Comparison of the geometry of the flatback airfoils NACA8648.

	Max. thickness	at x/c	Max. camber	at x/c
NACA8648	48 %	29.5 %	8 %	59,2 %
NACA8648 TE 5 %	48,43 %	30,1 %	8 %	59,9 %
NACA8648 TE 10 %	48,99 %	31,1 %	8 %	59,9 %
NACA8648 TE 20 %	50,15 %	33,2 %	8 %	59,9 %
NACA8648 TE 30 %	51,41 %	34,9 %	8 %	59,2 %

Table 7.1: Geometrical characteristics of the airfoils shown in 7.12 relative to the chord.

Figures 7.13, 7.14 and 7.15 show the aerodynamic characteristics obtained with OpenFOAM for the airfoil NACA8648 and the different flatback airfoil generated by opening the trailing edge as it is shown in 7.12. It can be seen

that both lift and drag coefficients increase for the angles of attack from 0 to 22 degrees which make the lift-to-drag ratio (shown in figure 7.15) also increase for these. The highest increments for the lift-to-drag ratio are given for the lowest angles of attack computed. However, for the angles of attack at which the inner parts of the blade work (i.e. 10-15 degrees), these increments seen in the lift-to-drag ratio are up to 32 %.

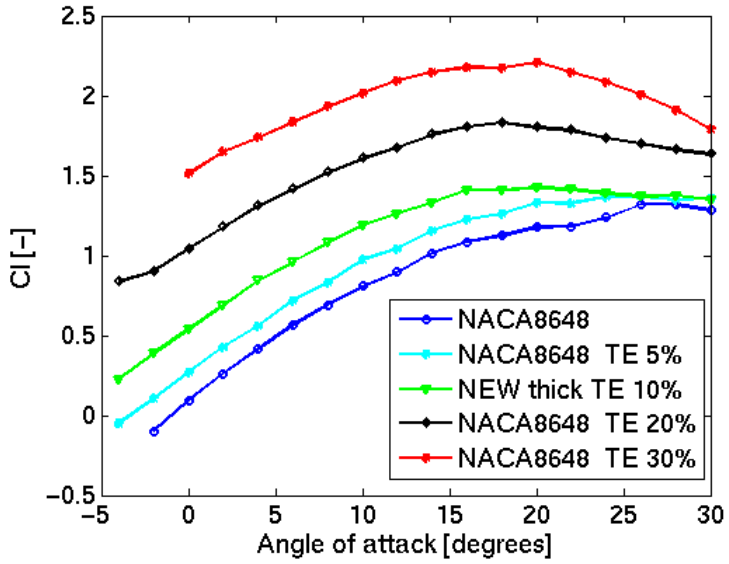

Figure 7.13: Lift coefficient normalized for the airfoil NACA8648 at Re=4.000.000.

In figure 7.16 they are shown the location of the transition points at both suction and pressure side of the airfoil. As it was shown previously in chapter 6 the transition point moves closer to the trailing edge while thickening it. This yields to more region of laminar boundary layer, which involves higher velocities at the suction side and a higher suction peak, as it is shown in figure 7.17. Due to the shape of the airfoil the boundary layer remains more attached while the trailing edge thickens yielding to higher Cp (in absolute value) all over the wall of the airfoil. Regarding the drag coefficient increment it can be seen in figure 7.18a that the friction coefficient is increasing at the suction side the thicker the trailing edge of the airfoil gets, while on the pressure side (as it can be seen in figure 7.18b) this is decreasing. Since the values of Cf on the suction side are higher, this yields to the increment in the drag coefficient shown in figure 7.14.

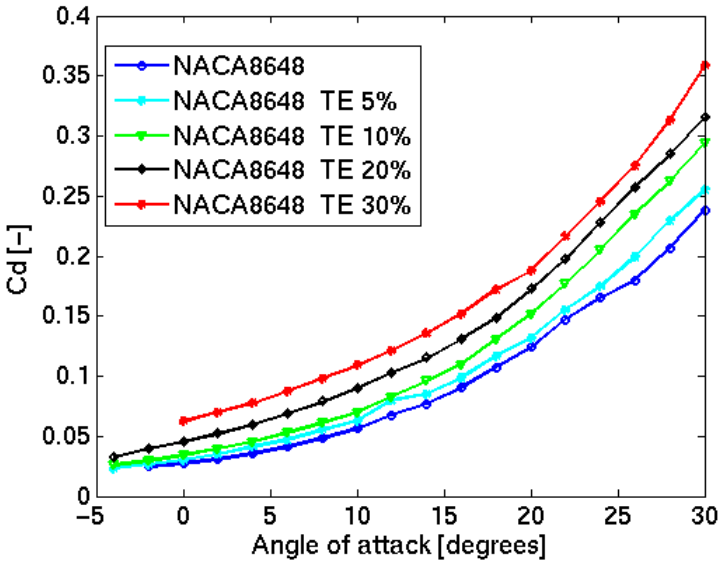

Figure 7.14: Drag coefficient normalized for the airfoil NACA8648 at Re=4.000.000.

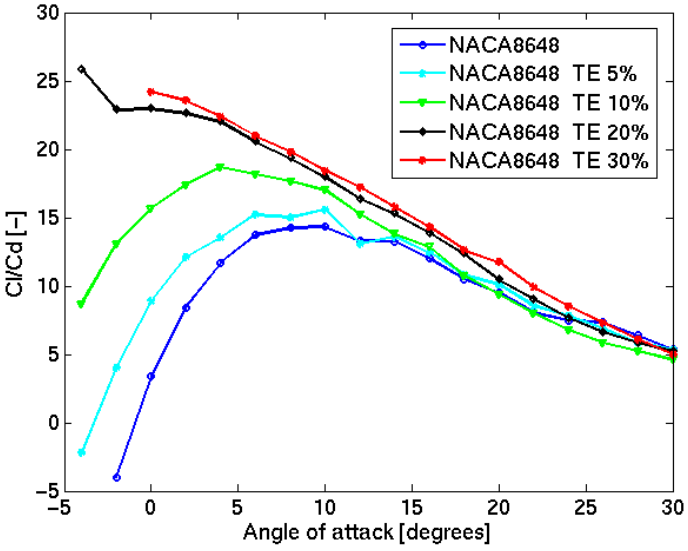

Figure 7.15: Lift-to-drag ratio normalized for the airfoil NACA8648 at Re=4.000.000.

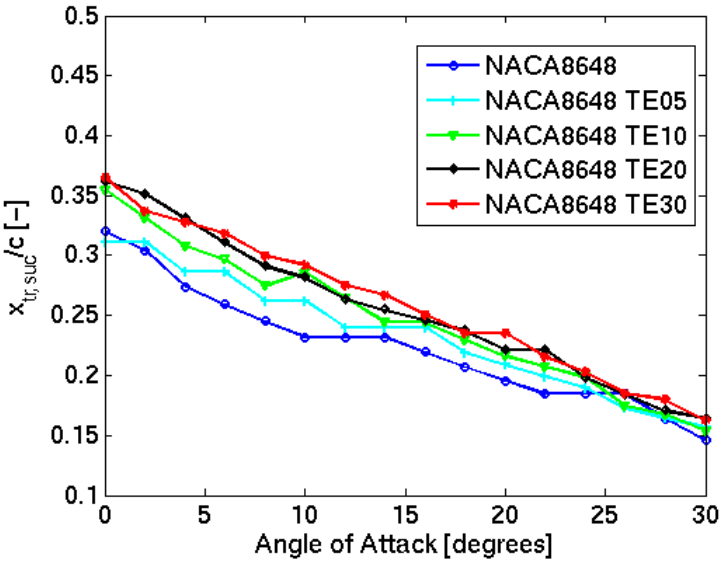

(a) Suction side.

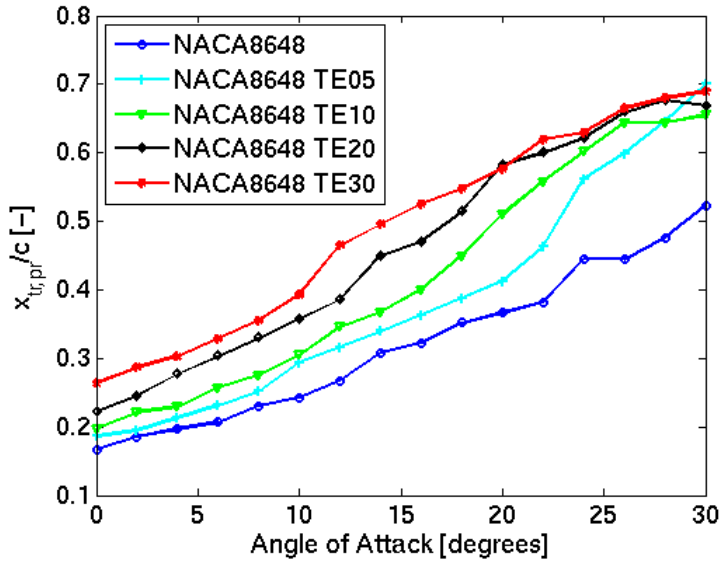

(b) Pressure side.

Figure 7.16: Location of the transition point for laminar to turbulent boundary layer at the airfoil NACA8648 at Re=4.000.000.

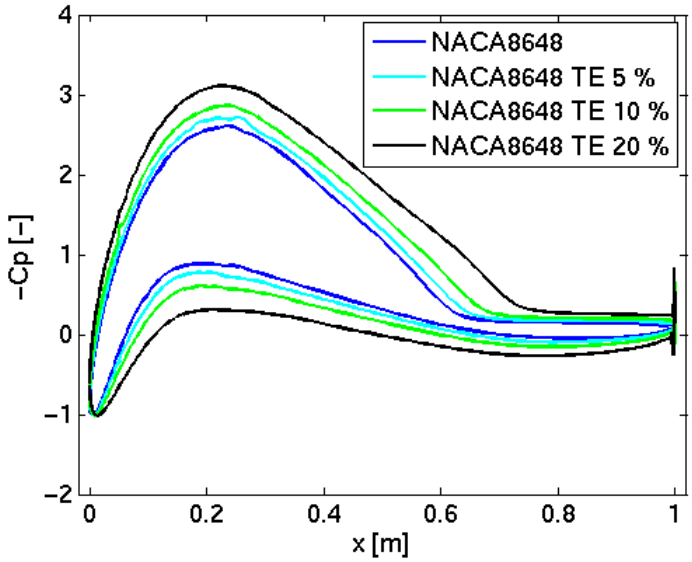

Figure 7.17: Pressure coefficient at the airfoil NACA8648 at Re=4.000.000 and an angle of attack of 10 degrees.

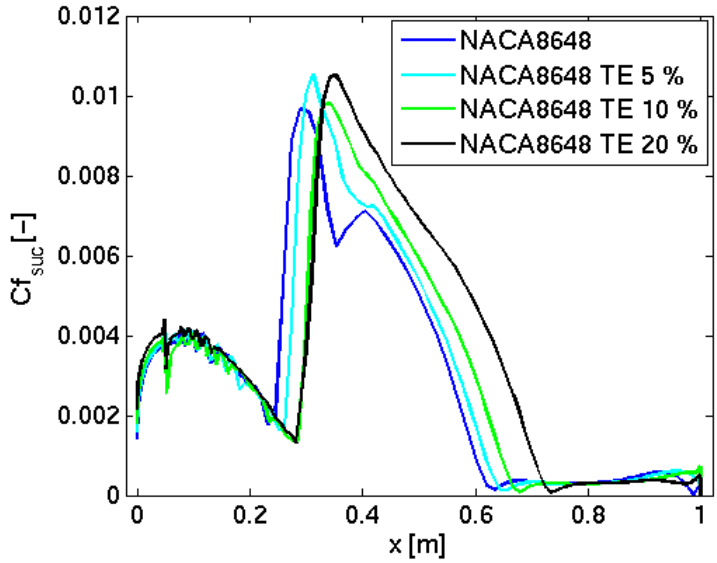

(a) Suction side.

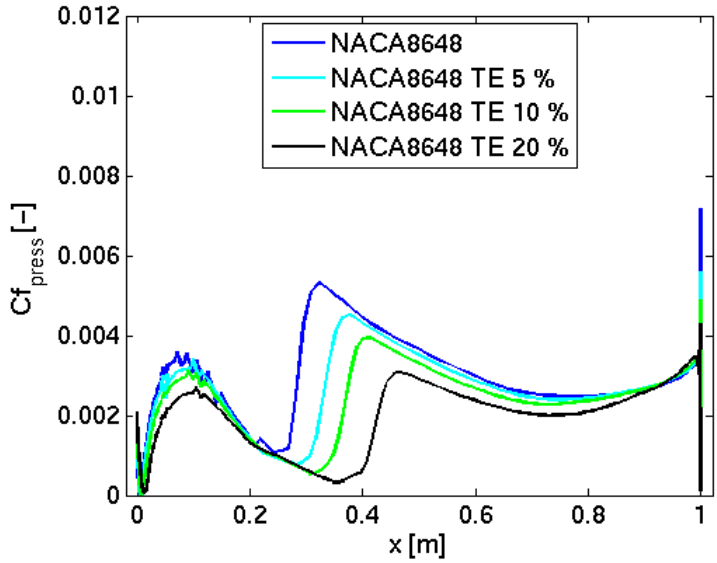

(b) Pressure side.

Figure 7.18: Friction coefficient at the airfoil NACA8648 at Re=4.000.000 and an angle of attack of 10 degrees.

Chapter 8

Comments to the convergence of the solution

As it has been shown in the previous chapters the results obtained with OpenFOAM are good compared with the results obtained using other programmes (ANSYS CFX and Ellipsys) or obtained by wind tunnel experiments. There is one aspect that has to be investigated though, this is related with the speed and the convergence of the solution.

8.1 Initialization of the field with *potentialFoam*

In order to gain some computational time, the solutions performed are initialized with a solver called *potentialFoam*. This basically gives a velocity field for the given initial conditions by assuming that it has a irrotational velocity field.

It is shown an example of how this initialization helps with the convergence of the results. It is run a simulation for a flat plate. In figures 8.2 and 8.1, it can be appreciated how the fields look like at time step 15 for the case with the *potentialFoam* initialization (figure 8.1) and without this initialization (figure 8.2). In the case initialized with *potentialFoam* it can be seen a developed boundary layer opposite to the case not initialized with *potentialFoam*.

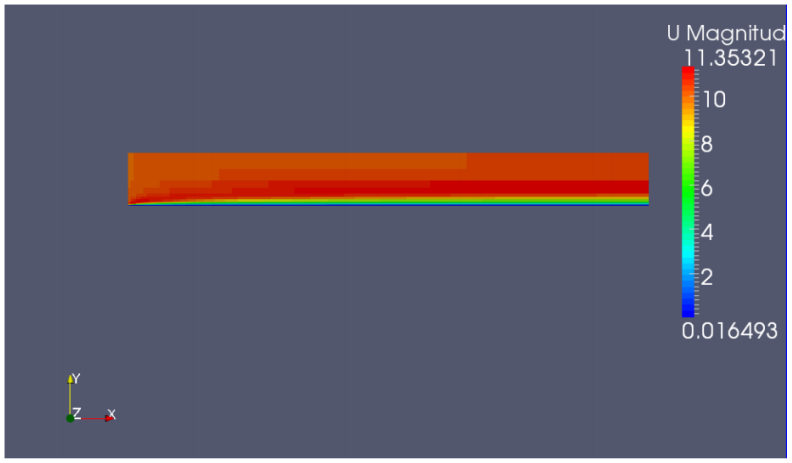

Figure 8.1: Solution for the flow around a flat plate at time step 15, field initialized with *potentialFoam*.

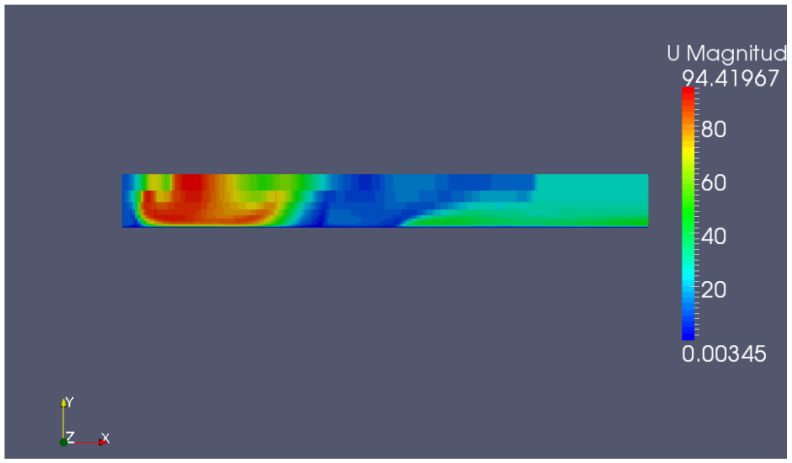

Figure 8.2: Solution for the flow around a flat plate at time step 15, field not initialized with *potentialFoam*.

8.2 Sensitivity Study

In order to look for the settings that give teh fastest solution, it has been done a sensitivity study on how changing the different parameters of OpenFOAM's *fvSolution* file affect the speed and convergence of the solution. This file is where the equation solvers, tolerances and algorithms to be used are defined. A copy of this file is shown in appendix I. Information about the different possibilities available in OpenFOAM and a brief explanation of all the parameters that can be set is explained in [15]. The flow over a NACA0012 with a blunt trailing edge (where 4.3 % of the chord is removed as stated in 4) at Re=3.000.000 and an angle of attack of 4 degrees is studied using $k-\omega$ SST turbulence model without transition model applied at the boundary layer. The mesh used has 130.000 cells and the cases are run in single mode, with one processor.

First of all, it was done a sensitivity study on how different values of *relTol* could affect the speed of the convergence of the solution obtained. This parameter sets the reduction of the residuals within every iteration of the SIMPLE algorithm. As it is stated in OpenFOAM's User Guide [15], it is uneconomical to set a low value of *relTol*. A value between 0.01 and 0.1 is recommended, but as stated, it depends on each case because there can be cases which require a value for *relTol* of 0.9. The range of *relTol* tried is $0.001 < relTol < 0.5$ and the fastest solutions have been for $0.01 < relTol < 0.05$.

Then, they have been tried different solvers for the pressure and velocities equations. These are PCG and GAMG for the pressure equation and PBiCG and GAMG for the velocity equation. Further information can be found in [15], PCG and PBiCG are Pre-conditioned (bi-)conjugate gradient solvers and GAMG (Generalized geometric-algebraic multi-grid solver). It was found that using GAMG solver for both pressure and velocities equations yield to faster solutions. It was also tried the GAMG solver for k and ω equations and the force coefficients started to diverge. As it is explained in [15], this multigrid solver uses a coarser mesh than the one given in principle to obtain a solution, then refines it and maps the solution to a finer mesh generated. One of the parameters to set in this solver is *nCellsInCoarsestLevel*, this gives an approximation of the mesh size at the coarsest level. As it is stated in a post in one forum of the internet [32] by Hrvoje Jasak (one of OpenFOAM's developers), any value for *ncellsInCoarsestLevel* between 12 and 200 will give the same result. They have been tried values for this parameter between 80 and 240 and the conclusion was that any value between 120 and 180 yield to the same optimal *ClockTime*. In this GAMG solver, they can be also set different values for the speed at which the coarsening levels is done by changing the parameter *mergeLevels*. In OpenFOAM's UserGuide [15] it is recommended to do one coarsening at a time (i.e. $mergeLevels = 1$), but is also said that for simple meshes a value of *mergeLevels* of 2 can be used. They

were tried values of *mergeLevels* of 1, 2 and 3 and the fastest result seen is for 1 coarsening at a time.

The fastest solution for the mentioned case with all the specified settings with OpenFOAM was obtained after two hours and 30 minutes of computation. While in ANSYS CFX a solution for the same mesh and boundary conditions is obtained within one hour and fifteen minutes, with comparable hardware. There is a difference in the solver used though, the former uses the SIMPLE algorithm, which is explained in [19] and the latter uses the coupled solver. Information about this solver can be found in ANSYS CFX manual. This fastest solution found was obtained using the *fvSolution* file shown in appendix I.

The same airfoil at the same conditions was run with free transition at the boundary layer, it took 15 hours to get to the converged solution. The transition modeled implemented is not found in the version of OpenFOAM used (v 1.7.1), the transition model explained in [20] was compiled in order to use it during this thesis. Thus, the fact that it has not been studied deep by OpenFOAM's developers may be the reason of this high clock-time obtained.

Chapter 9

Conclusion

This chapter shows the conclusions obtained while developing the thesis and gives some recommendations to be done in future work within this thesis.

OpenFOAM validation

In the first part it has been shown how the programme OpenFOAM (v1.7.1) is comparing it to other commercial software like ANSYS CFX (v13.0) and Ellypsis and to some experimental results for 2D airfoils. Good agreement in the linear region of the lift curves for all the airfoils is found. At high angles of attack, when the flow begins to stall, usually little agreement is found for any results shown for the other programmes either. On the other hand, the drag coefficients results are also difficult to judge whether they are good or not compared to each other because usually no perfect coincidence is shown for the results obtained. However, the results obtained with OpenFOAM are always within the range the other programmes show.

Furthermore, in order to validate the programme OpenFOAM different sensitivity studies for a thin airfoil, NACA0012, have been performed. 4,3% of the chord of this airfoil has been cut off in order to do it so a mesh topology like the one used for the thick flatback airfoils computed is used, i.e. O-mesh. These sensitivity studies are for 1) the maximum y^+ obtained over the airfoil, 2) the size of the domain used in order to simulate the flow, 3) the numerical schemes used for the convective terms at angles of attack approaching the stall region, 4) the number of cells of the meshes used and 5) whether is suitable or not adding the transition prediction model for the boundary layer of the airfoils computed.

The speed of OpenFOAM is evaluated. A case with the same boundary conditions and mesh run with the k-ω SST turbulence model takes the double amount of wall clock time with OpenFOAM than with ANSYS CFX to get to the converged solution (2 hours and 30 minutes vs 1 hour and 15 minutes), run with 1 single CPU core with comparable hardware. It has to be taken

into account, though, that OpenFOAM uses the SIMPLE algorithm, while ANSYS CFX uses the coupled solver explained in ANSYS CFX manual.

Flatback airfoils study

The trailing edge of the flatback airfoils studied was thickened the same percentages of the chord length towards pressure and suction side. Airfoils with thicknesses of 35 % and 36 % relative to the chord were made flatback by thickening the trailing edge 5 %, 10 % and 20 % relative to the chord. It was seen that the drag coefficient was higher the thicker the trailing edge, the lift coefficient was increasing also (mainly for high angles of attack, where Cl_{max} is found), but the lift-to-drag ratio was decreasing while thickening the trailing edge of the airfoil. For example, for an angle of attack of 10 degrees, at which this airfoil would work, a decrease of the lift-to-drag ratio of 75 % is seen while thickening the trailing edge thickness from 1,5 % to 20 %.

The trailing edge of very thick airfoils (with thicknesses of 48 % and 56 % relative to the chord) was increased from 1,5 % to 5 %, 10 %, 20 % and 30 %. For the airfoils with the trailing edge opened up to 20 % chord lengths there is an increase of the lift-to-drag ratio the thicker their trailing edge is (even though both lift and drag are increasing). For example, for angles of attack between 12 and 16 degrees (at which these airfoils are supposed to operate because of being situated close to the root of the blade), it is found an increment of 142 %. However, while trying to thicken the trailing edge even more (up to 30 % chord lengths), its lift-to-drag ratio is below the lift-to-drag ratio of the airfoil with the trailing edge opened 20 % chord lengths due to the huge increase of its drag coefficient.

The behavior of the flow around one of the flatback airfoils was investigated. It is shown that while adding chord to one of these flatback airfoils into the dead water zone created behind it the lift force that it presents is not modified and the Cp curve of the airfoil at a certain angle of attack does not change either (despite of the pressure at the small part added is almost 0). Thus, the pressure distribution of a flatback airfoil is the same as the one of one airfoil with longer chord into this flatback airfoils wake. Regarding the drag of the airfoils with these modifications, their friction coefficient all over the airfoil is also very similar to the one of the flatback airfoil they are coming from.

9.1 Future work

In order to continue deeper with the study of flatback airfoils created after thickening the same percentage the trailing edge towards pressure and suction side, some ideas given are:

1. Investigate deeper in the influence of the thickness on the improvements obtained with the flatback airfoils.
2. Investigate more parameters that can be the reason of the good performance of the flatback airfoil. For example, position of the maximum thickness, maximum camber or the position of maximum camber.
3. Fix transition point to check if they are less sensitive to surface soiling. Which is said in reference [1] to be one of their advantages. This can be checked by fixing the transition point of the boundary layer from laminar to turbulent and studying the evolution of the aerodynamic performance.

In order to continue with the study of OpenFOAM, some ideas given are:

1. Realize unsteady simulations to check how good is the performance of the solution, i.e. (quality compared to experiments and other codes and speed of computations).
2. Investigate if there is a way in order to fix the transition point of the boundary layer to a desired location.

9.2 Future work

In order to continue deeper with the study of flatback airfoils created after thickening the same percentage the trailing edge towards pressure and suction side, some ideas given are:

1. Investigate deeper in the influence of the thickness on the improvements obtained with the flatback airfoils.
2. Investigate more parameters that can be the reason of the good performance of the flatback airfoil. For example, position of the maximum thickness, maximum camber or the position of maximum camber.
3. Fix transition point to check if they are less sensitive to surface soiling. Which is said in reference [1] to be one of their advantages. This can be checked by fixing the transition point of the boundary layer from laminar to turbulent and studying the evolution of the aerodynamic performance.

In order to continue with the study of OpenFOAM, some ideas given are:

1. Realize unsteady simulations to check how good is the performance of the solution, i.e. (quality compared to experiments and other codes and speed of computations).
2. Investigate if there is a way in order to fix the transition point of the boundary layer to a desired location.

Bibliography

[1] Tom Ashwill and Paul Veers
Innovative Design Approaches for Large Wind Turbine Blades
Sandia National Laboratories

[2] C.P. van Dam, J.P. Baker and E.A. Mayda
Experimental Analysis of Thick Blunt Trailing-Edge Wind Turbine Airfoils.
Department of Mechanical and Aeronautical Engineering. University of California

[3] Jonathon P. Baker, C.P. (Case) van Dam, and Benson L. Gilbert. Flatback Airfoil Wind Tunnel Experiment. Sandia National Laboratories

[4] Jonathon P. Baker and C.P. van Dam.
Drag Reduction of Blunt Trailing-Edge Airfoils
Department of Mechanical and Aeronautical University of California

[5] Fuller, Matthew (M.Eng.). Numerical simulation of a flat back airfoil for wind turbine applications. University of Louisville, 2010.

[6] L.Deng, Y.W. Gao. National Key Laboratory of Science and Technology on Aerodynamic Design and Research, Northwestern Polytechnical University, China.
J.T. Xiong [2]. Department of Mechanical and Aerospace Engineering. University of California, USA.
Computational aerodynamic analysis of flatback airfoils by coupling N-S equations and transition prediction codes.

[7] Aerodynamic and Aeroacoustic Properties of a Flatback Airfoil (Will it Rumble or Whisper?)
Dale E. Berg and Matthew Barone
Sandia National Laboratories

[8] Research on Thick Blunt Trailing Edge Wind Turbine Airfoils. C.P. (Case) van Dam. Mechanical and Aeronautical Engineering. University of California, Davis.

[9] C.P. Case Van Dam, Edward A. Mayda, David D. Chao, Dale E. Berg
Computational Design and Analysis of Flatback Airfoil Wind Tunnel Experiment
Sandia National laboratories

[10] Sheldahl, R.E. and Klimas, P.C. Aerodynamic Characteristics of Seven Airfoil Sections Through180 Degrees Angle of Attack for use in Aerodynamic Analysis of Vertical Aixs Wind Turbines. SAND80-2114, March 1981. Sandia National Laboratories, Albuquerque, New Mexico.

[11] Ira H. Abbott and Albert E. von Doenhoff. Theory of Wing Sections

[12] http://turbmodels.larc.nasa.gov/index.html

[13] F. R. Menter (August 1994)
Two-Equation Eddy-Viscosity Turbulence Models for Engineering Applications

[14] http://www.enercon.de/en-en/66.htm

[15] http://www.openfoam.com/docs/user/

[16] Harry B. Bingham, Poul S. Larsen and V. Allan Barker (2010). Computational Fluid Dynamics. Technical University of Denmark.

[17] Frank M. White. Viscous Fluid Flow (second edition). University of Rhode Island.

[18] David C. Wilcox. Turbulence modelling for CFD. California

[19] H K Versteeg and W Malalasekera (1995). An introduction to Computational Fluid Dynamics. The finite volume method.

[20] Robin Langtry, Florian Menter. ANSYS Germany GmbH. Overview of Industrial Transition Modelling in CFX.

[21] Georgi Kalitzin, Gorazd Medic, Gianluca Iaccarino, Paul Durbin. Near-wall behavior of RANS turbulence models and implications for wall functions. Flow Physics and Computation Division, Department of Mechanical Engineering, Stanford University, Stanford, CA 94305-3030, USA

[22] http://www.cortana.com/Drag_Description.htm

[23] http://www.free-online-private-pilot-ground-school.com/aerodynamics.html

[24] Niels N. Sørensen. CFD Modelling of Laminar-turbulent Transition for Airfoils and Rotors Using the $\gamma - \widetilde{Re}_\theta$ Model. Wind Energy Division, National Laboratory for Sustainable Energy, Risø-DTU.

[25] Jeppe Johansen. Prediction of Laminar/Turbulent Transition in Airfoil Flows. Risø-DTU

[26] Niedriggeschwindigkeitsprofile, Dieter Althaus, ISBN3-528-03820-9, Friedr. Vieweg und Sohn Verlagsgesellschaft mbH, Braunschweig/Wiesbaden, 1996. *Measured data taken from the disk of the book.*

[27] Niels Sørensen. Small Study of flatback airfoils. Risø DTU (27-01-2011).

[28] http://www.nioclibrary.ir/e-resources/introduction/Ebook/C14.PDF

[29] Ladson, C.L., Hill, A.S., and Johnson, Jr., W.G. "Pressure Distributions from High Reynolds Number Transonic Tests of a NACA0012 Airfoil in the Langley 0.3-Meter Transonic Cryogenic Tunnel"

[30] Abbott, I. H., and Von Doenhoeff, A.E. *Theory of Wing Sections*. Dover Publications, Inc., New York, 1959.

[31] Gregory, N. and O'Reilly, C.L. Low-Speed Aerodynamic Characteristics of NACA0012 Airfoil Section, Including the Effects of Upper-Surface Roughness Simulating Hoar Frost. Tech. rep., NPL AERO Rept. 1308, 1970.

[32] http://www.cfd-online.com/Forums/openfoam-solving/59936-amg-versus-iccg.html

[33] Marzocca, Pier. "The NACA airfoil series". Clarkson University.

[34] Drela, M. XFOIL: An Analysis and Design System for Low Reynolds Number Airfoils. Conference on Low Reynolds Number Airfoil Aerodynamics. University of Notre Dame, June 1989.

[35] http://web.mit.edu/drela/Public/web/xfoil/xfoil_doc.txt

[36] Drela, M. Integral Boundary Layer Formulation for Blunt Trailing Edges. Paper AIAA-89-2166, August 1989

Appendix A

Meshing a NACA0012 with a sharp trailing edge

In order to mesh the original NACA0012, with the sharp trailing edge, it has been used a C-mesh. In order to do so, a mesh like the one appearing in figure A.1a was done at the beginning. The problem was that the solution with OpenFOAM started to diverge because of the high aspect ratios present at this mesh, thus the different distribution of cells shown in figures A.1 were tried. The idea was to decrease the maximum aspect ratio obtained.

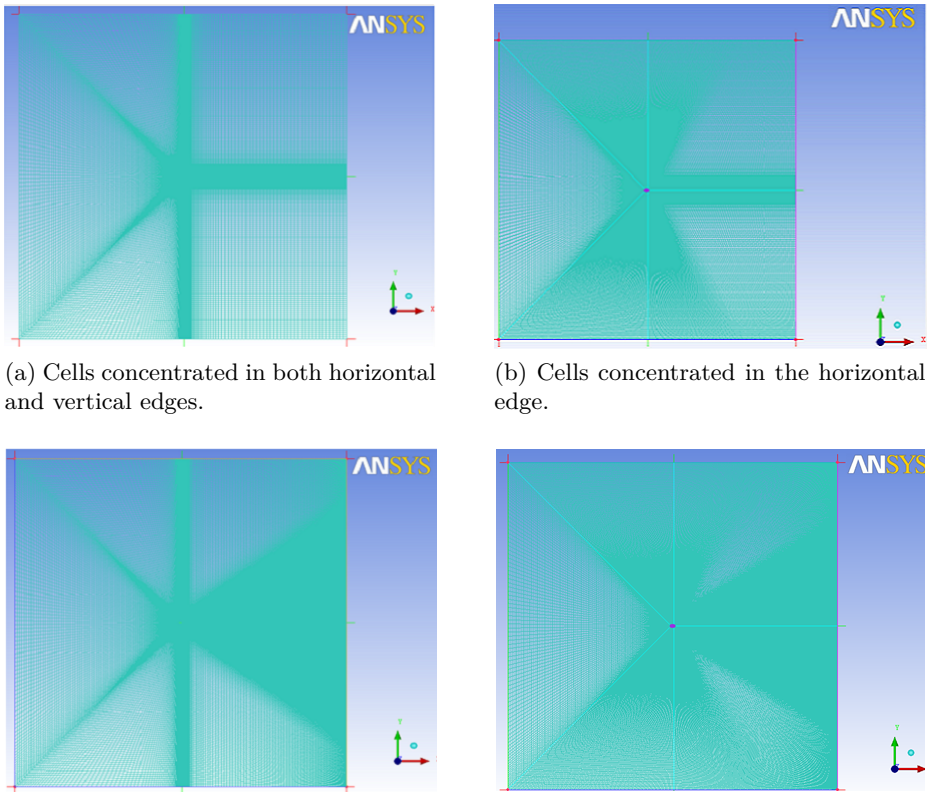

(a) Cells concentrated in both horizontal and vertical edges.

(b) Cells concentrated in the horizontal edge.

(c) Cells concentrated in the vertical edge.

(d) No cells concentrated.

Figure A.1: Different C-meshes tried for the airfoil NACA0012.

In table A.1 they are given the results for the force coefficients obtained for the different meshes from figures A.1 tried for the sharp NACA0012 airfoil with the C-mesh topology. While changing the concentration of the cells in the different edges the maximum aspect ratio obtained was different and also the results obtained for the lift coefficients (it varies $4,3\%$ from case 3 to 5) and the drag coefficient (it varies 43% from case 3 to 5). While avoiding the use of concentrated cells in both horizontal and vertical edges at the trailing edge the aspect ratio is decreased by using a different expansion ratio at the edge of the inlet or outlet, this is seen in table A.1, in columns referring to maximum aspect ratio and cells with aspect ratio higher than 1000. The

difference between meshes of case 4 and 5 are the expansion ratios used at the wall of the airfoil and the height of the cells closest to the airfoil. For case 5 run with OpenFOAM, for angles of attack from 12 to 18, the maximum y^+ found was between 2 and 2.6. For the same case, while being run with ANSYS CFX the maximum y^+ found was around 5, the reason of this difference even though being the same mesh is because OpenFOAM is a cell centered software and ANSYS CFX is a face centered software, thus the distance to the 1st node (y from equation 2.27) for the latest programme is the double as the distance for the former programme mentioned. The computations run with ANSYS CFX have been run with an option of the software called "automatic wall function", where the wall functions are activated for y^+ higher than 2.

The best solution considered is the solution of case 5 because it is the one with the drag closer to the experiments. It can be seen in table A.1 that the lift coefficient is over predicted compared to experimental data for the airfoil with the sharp trailing edge while for the airfoil with the blunt trailing edge the result is almost the same as the experimental value (there is a difference of $0,2\%$). It was expected though to have higher lift coefficient for the case with the blunt trailing edge. The drag coefficient is under predicted for the airfoil with the sharp trailing edge (there is a difference of 25% compared with the experimental data) while for the case with the blunt trailing edge it is over predicted (there is a difference of 35% compared with the experimental data).

Case	Mesh	Max. AR	High AR cells	Cl	Cd
1	A.1a	≈ 500000	36317	Divergence	Divergence
2	A.1b	≈ 500000	36317	Divergence	Divergence
3	A.1c	4355	4875	0.897	0.00525
4	A.1d	2329.72	75	0.9	0.006
5	A.1d	202.03	0	0.9235	0.00753
Experiments	-	-	-	0.9	0.01
OF blunt	O-mesh	292.377	0	0.8979	0.0135

Table A.1: Results obtained for an angle of attack of 8 degrees the different meshes tried shown in figures A.1. AR=Aspect Ratio

As it has been previously said, in OpenFOAM it could not be run the mesh of case 1 from table A.1, thus it is done a comparison with results of ANSYS CFX with mesh of case 1 from table A.1 and mesh of case 5. The results for lift and drag coefficients are shown in figures A.2 and A.3, respectively. It can be seen that there is almost no difference in the results obtained with the different meshes used, the only difference seen is for an angle of attack of 12 degrees.

Finally, for the mesh of Case 5 (from table A.1) which corresponds to the mesh in figure A.1d, it is done a comparison between the results obtained with both OpenFOAM and ANSYS CFX. This comparison is done in figures A.4

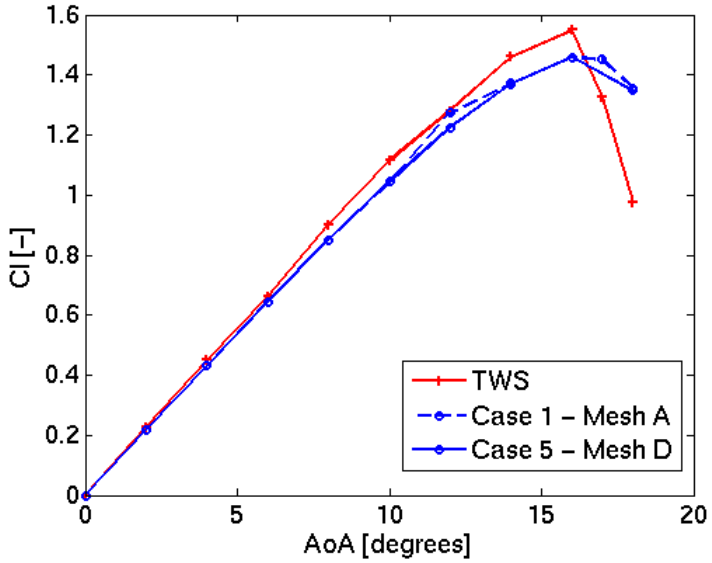

Figure A.2: Lift coefficient curves for the airfoil NACA0012 at Re=3.000.000 with different distribution of cells, cases from table A.1. Curves obtained with ANSYS CFX.

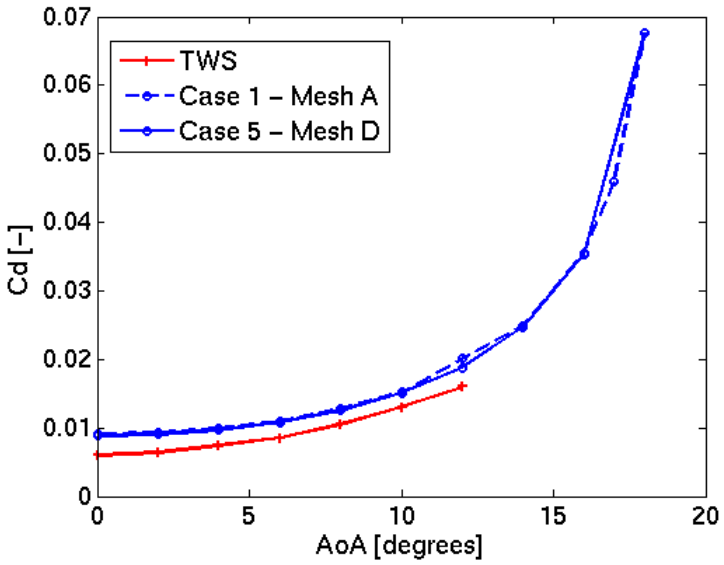

Figure A.3: Drag coefficient curves for the airfoil NACA0012 at Re=3.000.000 with different distribution of cells, cases from table A.1. Curves obtained with ANSYS CFX.

and A.5.

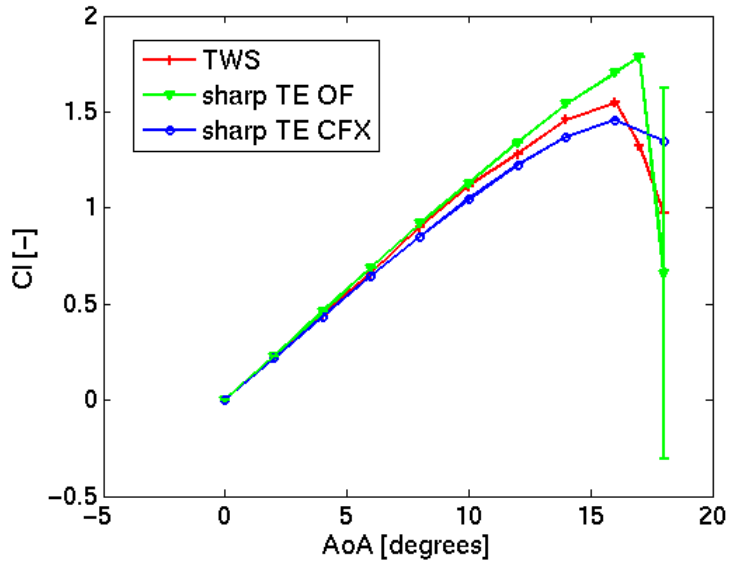

Figure A.4: Lift coefficient curves for the airfoil NACA0012 at Re=3.000.000 for the mesh from figure A.1d, case 5 from table A.1.

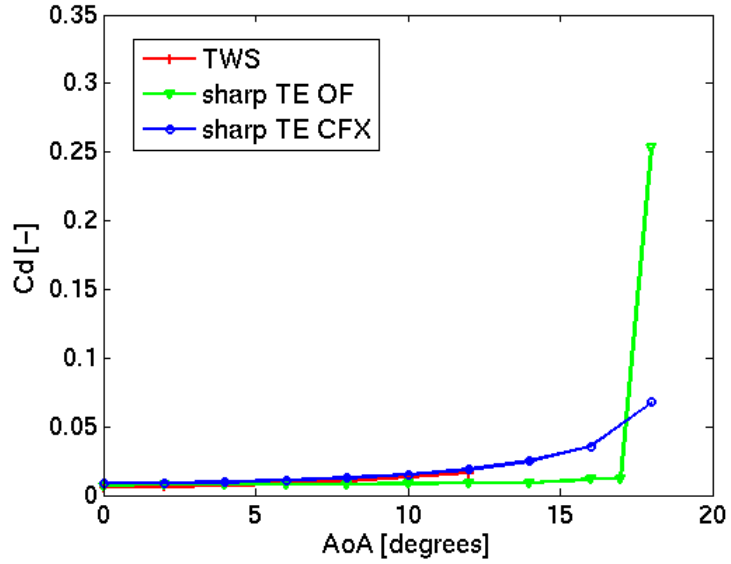

Figure A.5: Drag coefficient curves for the airfoil NACA0012 at Re=3.000.000 for the mesh from figure A.1d, case 5 from table A.1.

Appendix B

Results computed with ANSYS CFX and Ellipsys for the airfoils FX-77-W

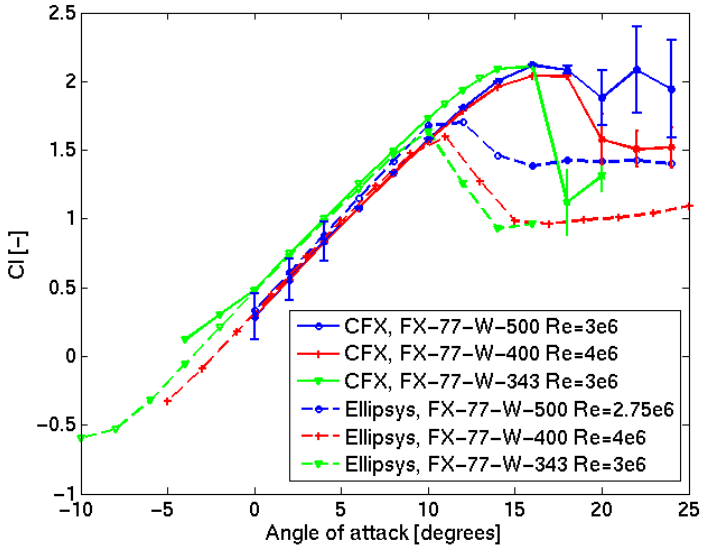

Figure B.1: Comparison of the results obtained with ANSYS CFX and Ellipsys of the lift coefficient for the airfoils FX-77-W at the different Reynolds number specified.

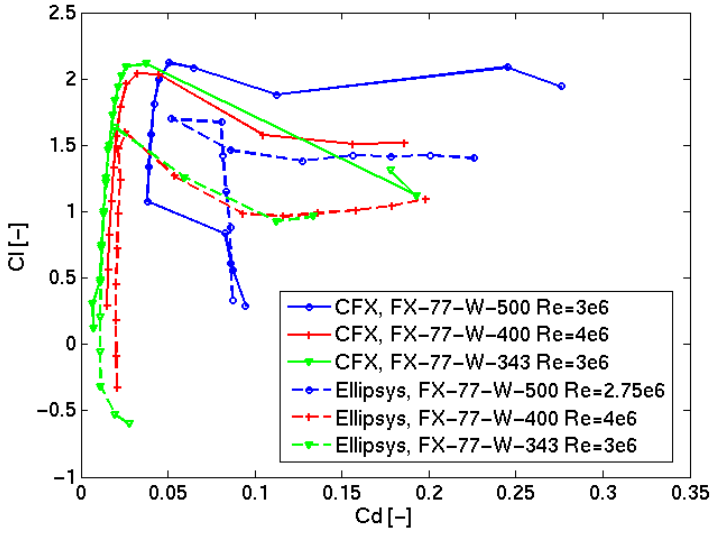

Figure B.2: Comparison of the results obtained with ANSYS CFX and Ellipsys for the drag coefficient of the airfoils FX-77-W at the different Reynolds number specified.

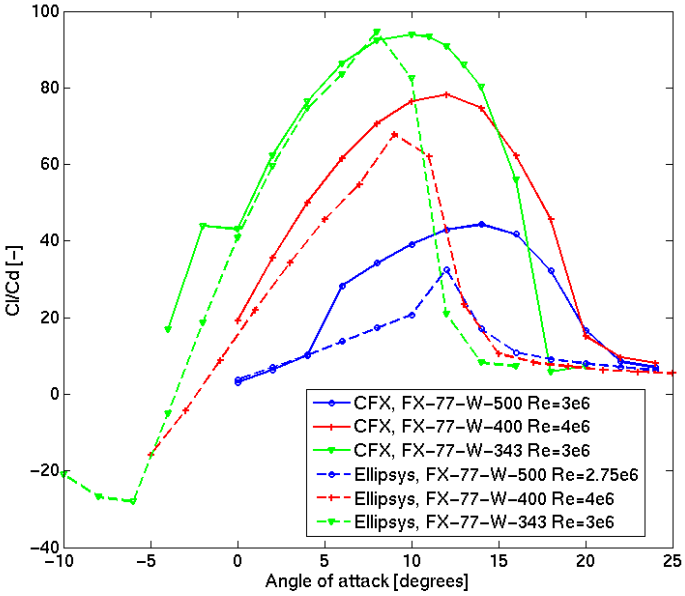

Figure B.3: Comparison of the results obtained with ANSYS CFX and Ellipsys for the lift-to-drag ratio of the airfoils FX-77-W at the different Reynolds number specified.

Appendix C

Results computed with ANSYS CFX and Ellipsys for the airfoils FB-3500-XXXX

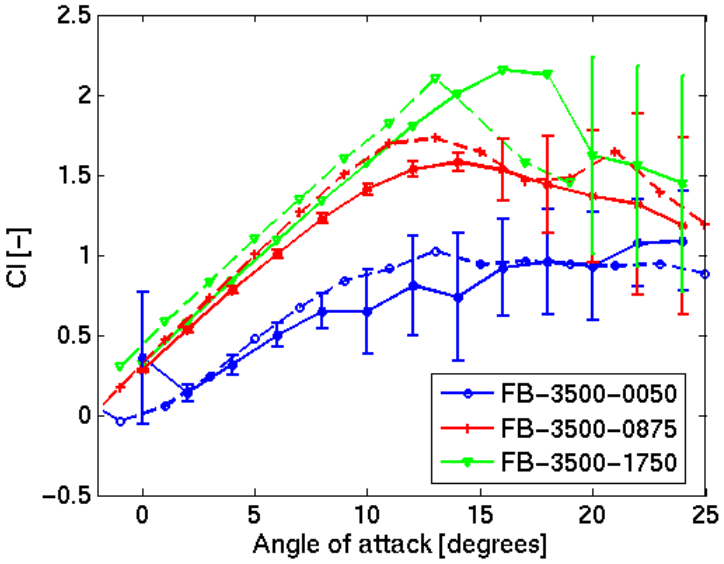

Figure C.1: Comparison of the the lift coefficient for the airfoils FB-3500 at Re=666.000. ANSYS CFX = solid line, Ellipsys = broken line.

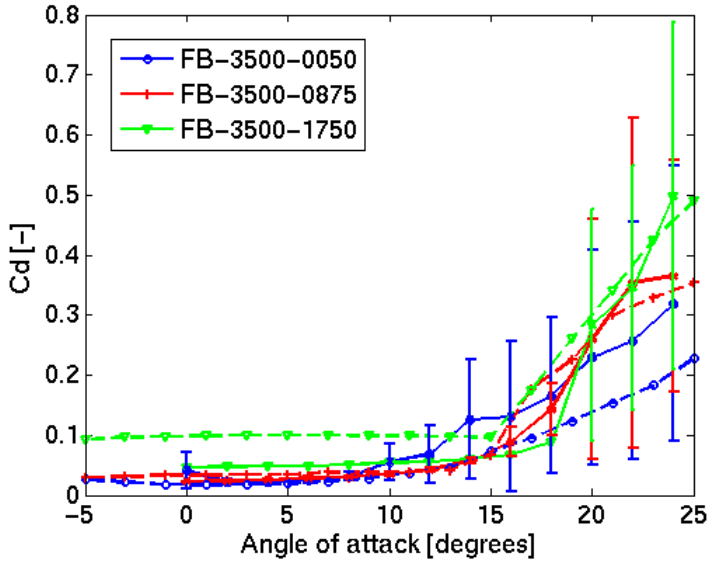

Figure C.2: Comparison of the drag coefficient for the airfoils FB-3500 at Re=666.000. ANSYS CFX = solid line, Ellipsys = broken line.

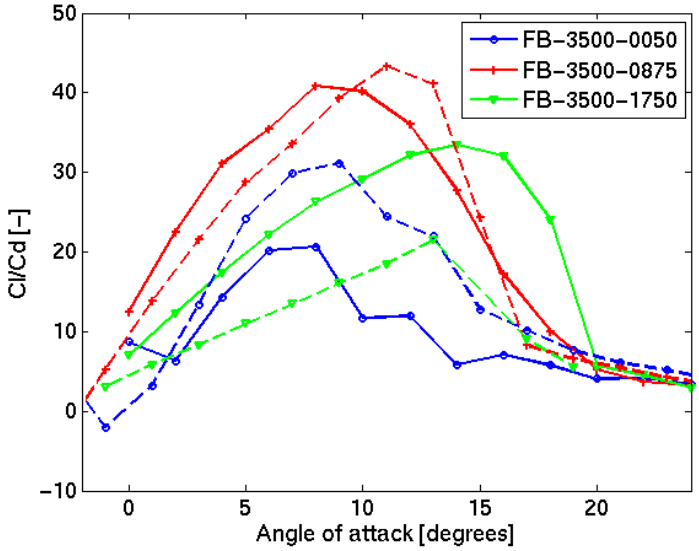

Figure C.3: Comparison of the lift to drag ratio of the airfoils FB-3500 at Re=666.000. ANSYS CFX = solid line, Ellipsys = broken line.

Appendix D

Comparison of the results obtained with OpenFOAM and ANSYS CFX for the airfoils NEW TE X%

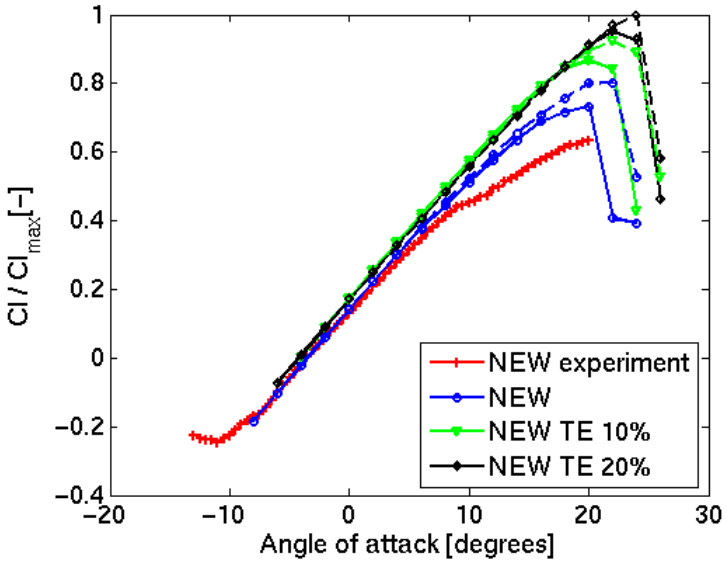

Figure D.1: Lift coefficient normalized for the airfoil *NEW* at Re=4.000.000. OpenFOAM=solid line, ANSYS CFX=broken line.

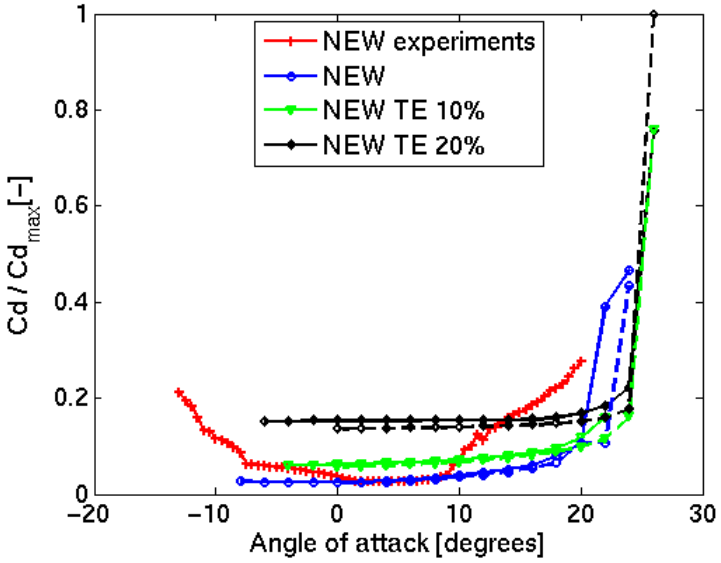

Figure D.2: Drag coefficient normalized for the airfoil *NEW* at Re=4.000.000. OpenFOAM=solid line, ANSYS CFX=broken line.

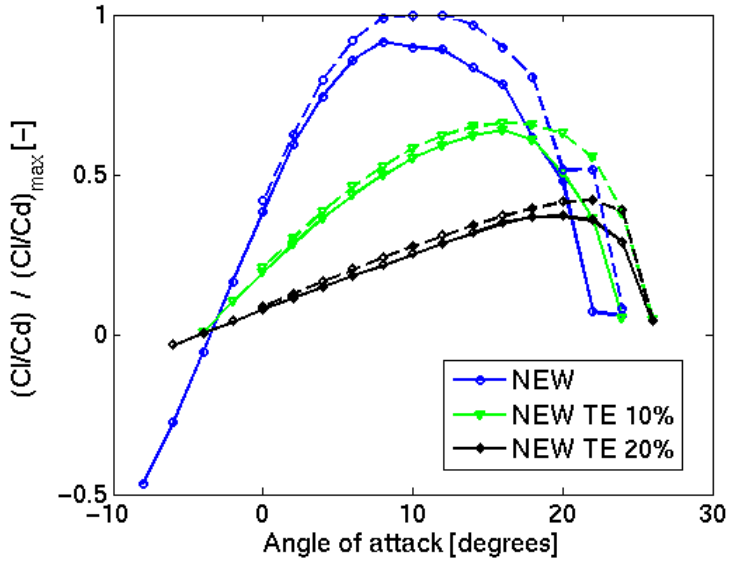

Figure D.3: Lift-to-drag ratio normalized for the airfoil *NEW* at Re=4.000.000. OpenFOAM=solid line, ANSYS CFX=broken line.

Appendix E

Comparison of the results obtained with OpenFOAM and ANSYS CFX for the airfoils *NEWsym* TE X%

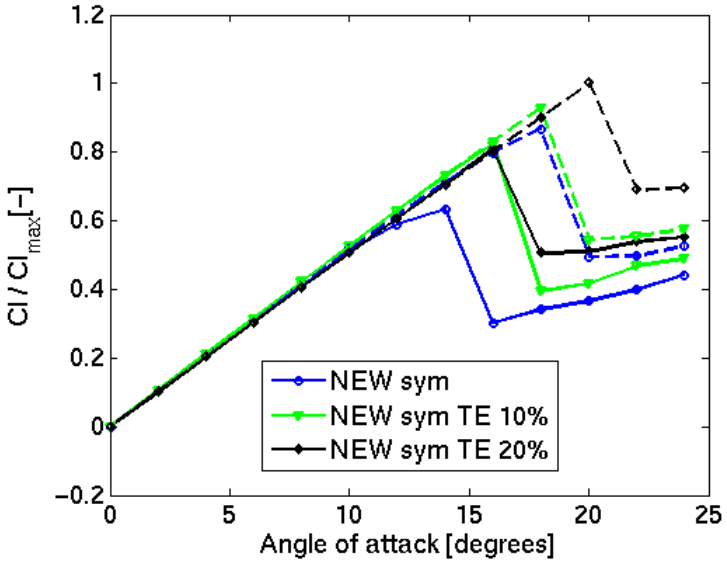

Figure E.1: Lift coefficient normalized for the airfoil *NEWsym* at Re=4.000.000. OpenFOAM=solid line, ANSYS CFX=broken line.

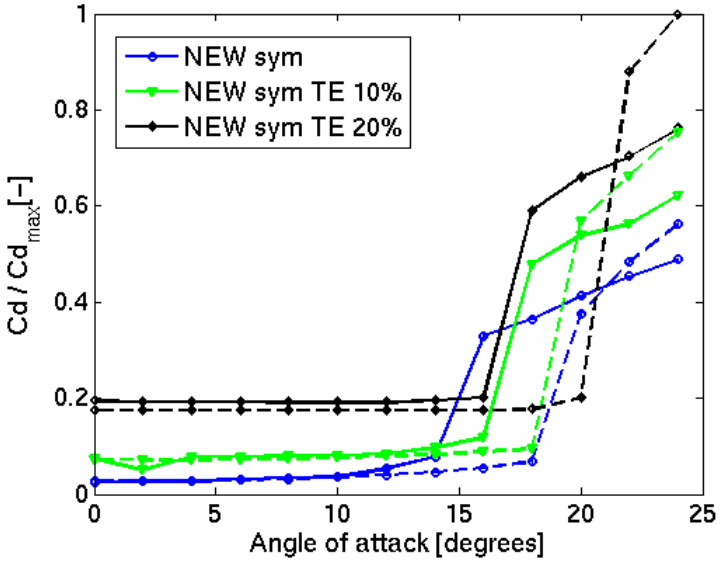

Figure E.2: Drag coefficient normalized for the airfoil *NEWsym* at Re=4.000.000. OpenFOAM=solid line, ANSYS CFX=broken line.

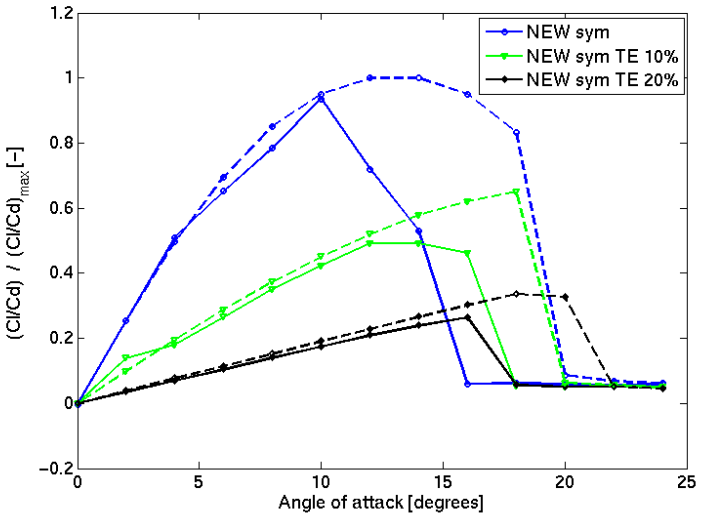

Figure E.3: Lift-to-drag ratio normalized for the airfoil *NEWsym* at Re=4.000.000. OpenFOAM=solid line, ANSYS CFX=broken line.

Appendix F

Comparison of the results obtained with OpenFOAM and ANSYS CFX for the airfoils *NEWthick* TE X%

Comparison of the results obtained with OpenFOAM and ANSYS CFX for the airfoils *NEWtsym* TE X%

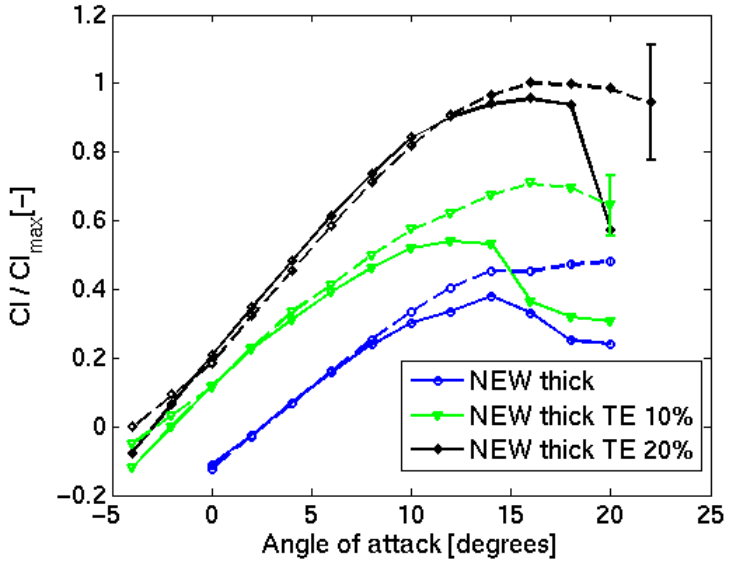

Figure F.1: Lift coefficient normalized for the airfoil *NEWthick* at Re=4.000.000. OpenFOAM=solid line, ANSYS CFX=broken line.

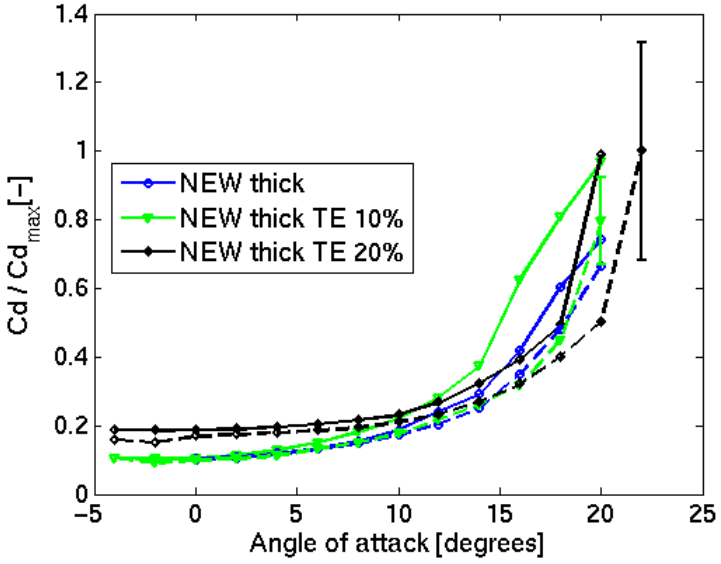

Figure F.2: Drag coefficient normalized for the airfoil *NEWthick* at Re=4.000.000. OpenFOAM=solid line, ANSYS CFX=broken line.

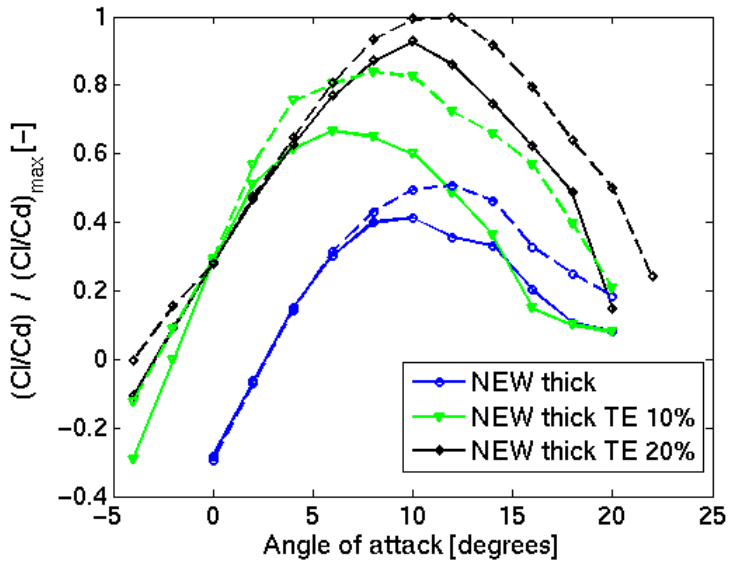

Figure F.3: Lift-to-drag ratio normalized for the airfoil *NEWthick* at Re=4.000.000. OpenFOAM=solid line, ANSYS CFX=broken line.

Appendix G

Mesh dependence study for the airfoil FX-77-W-400

It has been done a mesh dependence study for the airfoil FX-77-W-400 for angles of attack of 0 and 8 degrees. The results are shown in figures G.1 and G.2 for angles of attack of 0 and 8 degrees, respectively. These mesh dependence studies show differences of 1 % and 5 % for the lift and drag coefficients, respectively.

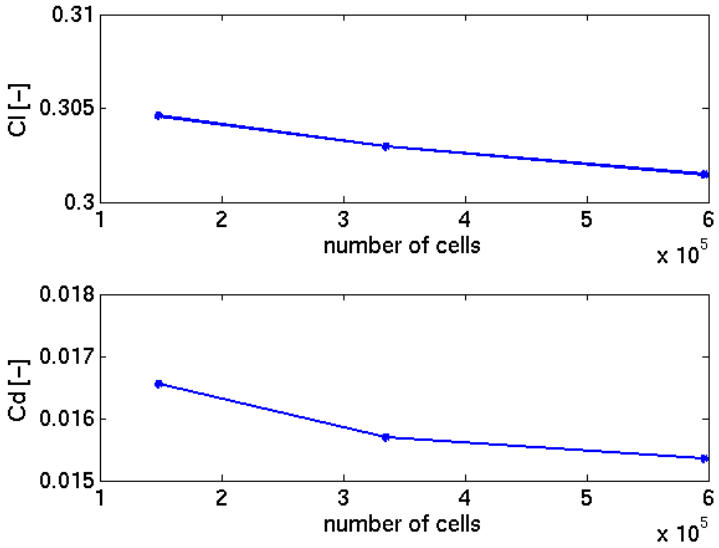

Figure G.1: Mesh dependence study for an angle of attack of 0 degrees for the airfoil FX-77-W-400 at Re=4.000.000.

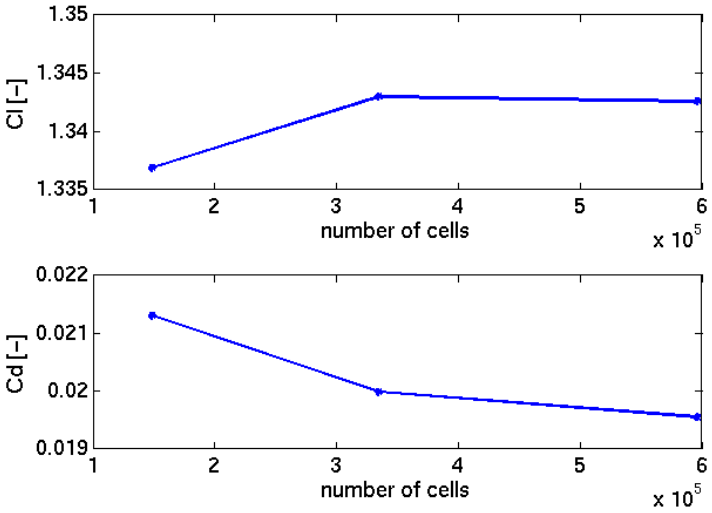

Figure G.2: Mesh dependence study for an angle of attack of 8 degrees for the airfoil FX-77-W-400 at Re=4.000.000.

Appendix H

Mesh dependence study for the airfoil FB-3500-0875

It has been done a mesh dependence study for the airfoil FB-3500-0875 for different angles of attack. The results are shown in figures H.1, H.2 and H.3 for angles of attack of 0, 8 and 16 degrees, respectively. While having a look at these mesh dependence studies one concludes that a finer mesh should be used to compute the flow around this airfoil because of the variation of the force coefficients while increasing the number of cells in the meshes used. For these cases there are difference at the coefficients up to 12 %, opposite to what it happened for the previous mesh dependence studies, where variations between 1-5 % were shown.

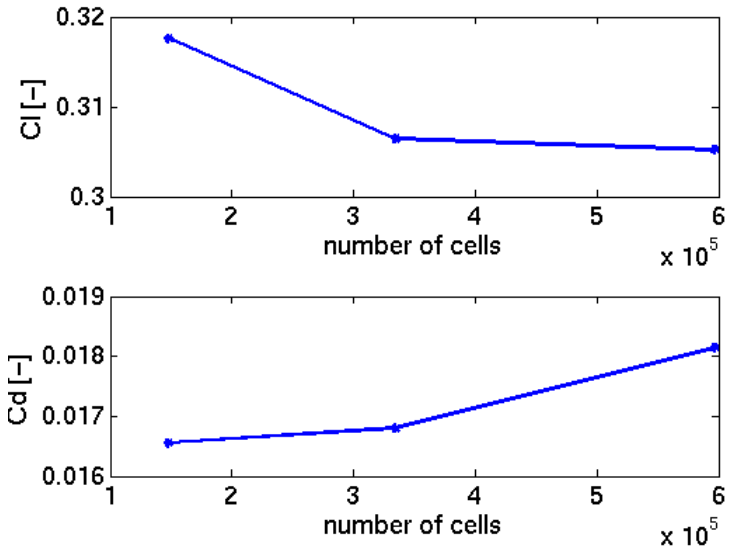

Figure H.1: Mesh dependence study for an angle of attack of 0 degrees for the airfoil FB-3500-0875 at Re=666.000.

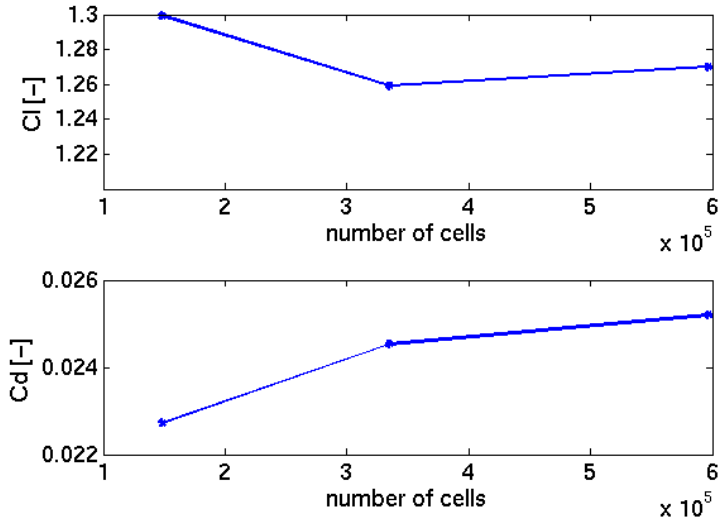

Figure H.2: Mesh dependence study for an angle of attack of 8 degrees for the airfoil FB-3500-0875 at Re=666.000.

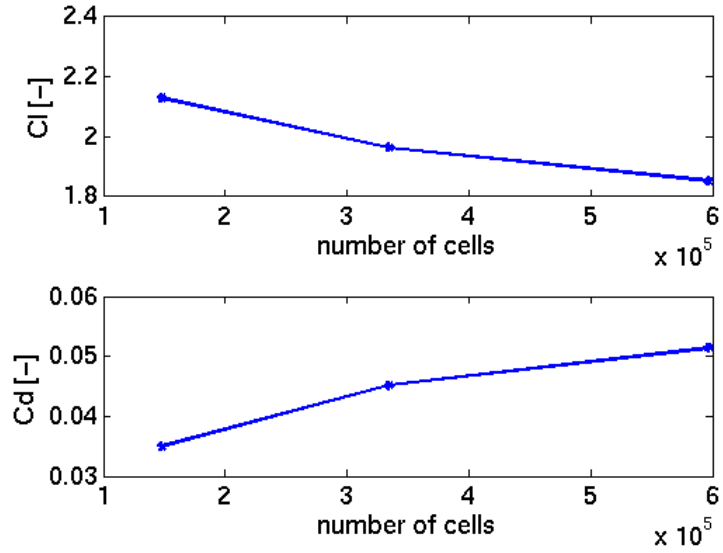

Figure H.3: Mesh dependence study for an angle of attack of 16 degrees for the airfoil FB-3500-0875 at Re=666.000.

Appendix I

Example of the *fvSolution* file of OpenFOAM

```
/*--------------------------------*- C++ -*----------------------------------*\
| =========                 |                                                 |
| \\      /  F ield         | OpenFOAM: The Open Source CFD Toolbox           |
|  \\    /   O peration     | Version:  1.7.1                                 |
|   \\  /    A nd           | Web:      www.OpenFOAM.com                      |
|    \\/     M anipulation  |                                                 |
\*---------------------------------------------------------------------------*/
FoamFile
{
    version     2.0;
    format      ascii;
    class       dictionary;
    location    "system";
    object      fvSolution;
}
// * * * * * * * * * * * * * * * * * * * * * * * * * * * * * * * * * * * * //

solvers
{
    p
    {
        solver          GAMG;
        tolerance       1e-10;
        relTol          0.01;
        smoother        GaussSeidel;
        nPreSweeps      0;
        nPostSweeps     2;
        cacheAgglomeration true;
        nCellsInCoarsestLevel 120;
        agglomerator    faceAreaPair;
        mergeLevels     1;
    }

    U
       {
```

```
36          solver          GAMG;
37          tolerance       1e-10;
38          relTol          0.01;
39          smoother        GaussSeidel;
40          nPreSweeps      0;
41          nPostSweeps     2;
42          cacheAgglomeration true;
43          nCellsInCoarsestLevel 120;
44          agglomerator    faceAreaPair;
45          mergeLevels     1;
46      }
47
48      k
49      {
50          solver          PBiCG;
51          preconditioner  DILU;
52          tolerance       1e-10;
53          relTol          0.01;
54      }
55
56      omega
57      {
58          solver          PBiCG;
59          preconditioner  DILU;
60          tolerance       1e-10;
61          relTol           0.01;
62      }
63
64   gamma
65      {
66         solver          PBiCG;
67          preconditioner  DILU;
68          tolerance       1e-10;
69          relTol          0.01;
70          minIter 1;
71
72      }
73
74      ReThetatTilda
75      {
76        solver          PBiCG;
77          preconditioner  DILU;
78          tolerance       1e-10;
79          relTol          0.01;
80          minIter 1;
81
82      }
83
84
85
86
87  }
88
89  SIMPLE
```

```
90  {
91      nNonOrthogonalCorrectors 0;
92  //    nNonOrthogonalCorrectors 20;        // for potentialFoam -writep
93  }
94
95  relaxationFactors
96  {
97      p               0.2;
98      U               0.8;
99      k               0.6;
100     omega           0.6;
101     gamma           0.7;
102     ReThetatTilda   0.7;
103 }
104
105
106 // ************************************************************************* //
```

DTU Mechanical Engineering
Section of Fluid Mechanics
Technical University of Denmark

Nils Koppels Allé, Bld. 403
DK- 2800 Kgs. Lyngby
Denmark
Phone (+45) 45 25 43 00
Fax (+45) 45 88 43 25

www.mek.dtu.dk